Evolutionary repurposing of a DNA segregation machinery into a cytoskeletal system controlling cyanobacterial cell shape

Benjamin L. Springstein[1,#], Manjunath G. Javoor[1,†], Daniela Megrian[2,†], Roman Hajdu[1], Dustin M. Hanke[3], Florian K. M. Schur[1], Martin Loose[1,#]

[1] Institute of Science and Technology Austria (ISTA), 3400 Klosterneuburg, Austria

[2] Institut Pasteur de Montevideo, Bioinformatics Unit, 11200 Montevideo, Uruguay

[3] Institute of General Microbiology, Kiel University, 24118 Kiel, Germany

[#] Address correspondence to Benjamin L. Springstein (benjamin.springstein@ista.ac.at) and Martin Loose (martin.loose@ista.ac.at).

[†] MJ and DM contributed equally

Running Title: Evolutionary repurposing of the ParMR system for cell shape control

Key words: ParM, ParR, DNA segregation, cell shape, cytoskeleton, bacteria, MinC, *Nostocales* cyanobacteria

Abstract:

Bacteria, despite their diversity, use conserved cytoskeletal systems for their intracellular organization. In unicellular bacteria, the ParMRC DNA partitioning apparatus is well known for forming actin-like filaments that push low copy number plasmids to opposite cell poles. In multicellular cyanobacteria such as *Anabaena* sp. PCC 7120, the presence of a chromosomally encoded ParMR system suggests it may play an analogous role in chromosome segregation. However, we show here that it instead constitutes a novel cytoskeletal system – termed CorMR – whose loss does not impair DNA segregation but leads to severe morphological defects, revealing a role in maintaining cell shape. Using live-cell imaging and *in vitro* reconstitution experiments, we demonstrate that CorM forms dynamically instable filaments. These filaments are recruited to the membrane by CorR, which has acquired a conserved N-terminal amphipathic helix specific to multicellular cyanobacteria. Cryo-EM analysis reveals that CorM forms antiparallel double-stranded filaments, in contrast to the polar, parallel filament pair seen in ParM. Furthermore, CorMR filaments are excluded from the cell poles and division plane by MinC, via a long N-terminal extension also specific to multicellular cyanobacteria. Comparative genomics suggests that cyanobacterial multicellularity co-evolved with the chromosomal relocation of ParMR genes, acquisition of the amphipathic helix in CorR, and functional extension of MinC, supporting an evolutionary link among these features. Our findings uncover a striking repurposing of ancestral biochemical systems, expanding the known roles of ParMR and Min systems beyond plasmid segregation and division site selection to include regulation of cell shape.

45 **Importance:**

46 The ParMRC system is a well-characterized machinery for the segregation of low-copy-
47 number plasmids to the cell poles and, until now, was primarily described to be encoded on
48 plasmids. We found that during the emergence of multicellularity in cyanobacteria, a
49 chromosome-encoded ParMR system has undergone extensive evolutionary and functional
50 repurposing, resulting in a previously undescribed bacterial cytoskeletal system that controls
51 cell shape. We also found that this new cytoskeleton, called CorMR, is under the control of the
52 MinCDE system, which has evolved to not only antagonize Z-ring formation, but also to
53 regulate CorM polymerization. Such interplay between different cytoskeletal systems highlights
54 an intricate regulatory mechanism linking cell division and morphology. As this repurposing of
55 existing cytoskeletal system coincided with the emergence of multicellularity in cyanobacteria,
56 it may have played a key role for the evolution of cyanobacteria with distinct cell shapes.
57 Overall, our discovery highlights the plasticity of bacterial polymeric systems and gives insight
58 into the evolution of cellular and multicellular complexity.

59

60 **Introduction:**

61 Bacteria employ different polymeric protein systems to control cell shape, growth and
62 division[1]. Protein filaments homologous to the eukaryotic cytoskeleton segregate plasmid DNA
63 (ParM)[2], control cell division (FtsZ and FtsA)[3–5], or mediate cell elongation (MreB)[6], as also
64 reviewed in [1]. In *E. coli* and many other rod-shaped species, a spatiotemporal oscillation of the
65 Min system generates an inhibitory gradient that restricts FtsZ polymerization to the midcell[7].

66 While these discoveries provided profound insights into how bacterial cells are
67 organized, prokaryotes exhibit immense evolutionary diversity, and we are only beginning to
68 grasp the full spectrum of their organizational strategies. This is particularly true for
69 Cyanobacteria, one of the most morphologically complex phyla described to date[8]. Especially
70 multicellular cyanobacteria exhibit a remarkable diversity in cell and cell filament (termed
71 trichome) morphologies, some of which are capable of cellular differentiation[9]. Among them,
72 multicellular cyanobacteria of the order *Nostocales*, including the model organism *Anabaena*

73 sp. PCC 7120 (hereafter *Anabaena*), form long trichomes and can differentiate heterocysts -
74 specialized cells capable of nitrogen fixation[10]. Like all cyanobacteria, *Anabaena* has a hybrid
75 Gram phenotype, containing an outer membrane and an unusually thick cell wall with several
76 layers of peptidoglycan (PG)[11]. Multicellularity in cyanobacteria arises through incomplete cell
77 division, resulting in a shared outer membrane, a continuous PG layer and metabolically
78 connected cytoplasms[10]. Septal junctions - functional analogs to eukaryotic gap junctions -
79 promote cell-cell communication through nanopores in the septal PG[10,12,13]. The emergence of
80 such complex, multicellular species likely requires the evolution of distinct protein systems to
81 organize the intracellular space, to maintain cell morphology and to control cell division.

82 The cellular physiology of multicellular cyanobacteria makes them a powerful model for
83 identifying potential novel solutions for these challenges. For example, cyanobacteria lack
84 FtsA[14,15], the predominant FtsZ membrane anchor in Gram negative bacteria such as *E. coli*[16],
85 and instead recruit FtsZ to the membrane by the cyanobacteria-specific protein ZipN[17]. Despite
86 the presence of thylakoid membranes, the Min system oscillates in unicellular cyanobacteria,
87 which possess an additional, cyanobacteria-specific protein – Cdv3 – that recruits MinC to
88 midcell. This suggests that both Cdv3 and MinE contribute to the spatial regulation of MinC's
89 inhibitory effect on Z-ring formation[18]. In contrast, much less is known about the role of MreB
90 in *Anabaena*. Unlike in other rod-shaped bacteria, MreB is not essential for viability but is
91 crucial for preserving the barrel-like shape of *Anabaena* cells[19–21]. It also contributes to septal
92 PG synthesis and is important for maintaining cell–cell communication between vegetative
93 cells and heterocysts[20,22].

94 Another characteristic of cyanobacteria is their remarkable diversity in chromosome
95 copy numbers, ranging from one to over 200 copies per cell[23], suggesting different strategies
96 to distribute the genetic information to their daughters. For instance, the highly polyploid
97 unicellular *Synechocystis sp.* PCC 6803 most likely relies on a random distribution of its up to
98 ~200 chromosomes during cell division[23,24]. In contrast, the maintenance of chromosomes and
99 low copy number plasmids probably depends on active DNA segregation systems[25]. For
100 instance, the unicellular *Synechococcus elongatus* PCC 7942 aligns its 3-6 chromosomes

101 along the long cell axis prior to cell division, through a mechanism that remains largely
102 unknown[26,27], although the involvement of a ParA-like protein has been speculated[28]. In
103 *Anabaena*, which contains ~8 chromosome copies, a dedicated segregation mechanism
104 seems likely, but none has been described to date[21].

105 In the context of a recent comparative analysis[19], we discovered a chromosomal ParMR
106 system in multicellular cyanobacteria such as *Anabaena.* As ParMR systems typically ensure
107 maintenance of low copy plasmids during bacterial cell division[29], we hypothesized that the
108 chromosomal systems in multicellular cyanobacteria may have evolved to control segregation
109 of chromosomes. Typically, the ParMR system consists of the actin-like ATPase ParM, the
110 DNA-binding adaptor protein ParR, and the centromere-like DNA element *parC*[29,30]. The
111 system gets initiated upon binding of ParR (generally encoded in an operon with *parM*) to short,
112 centromere-like *parC* elements on the plasmid, thereby forming ParRC complexes. *E. coli*
113 ParM forms parallel (i.e., polar), helical double-stranded filaments (a -filament being composed
114 of two protofilaments), which undergo cycles of polymerization and catastrophic
115 depolymerization[30–33]. Through this dynamic instability, ParM searches and captures ParRC
116 complexes, which then stabilizes one filament end. Antiparallel alignment of two ParRC-bound,
117 parallel ParM double-filaments gives rise to a cytoskeletal structure analogous to the mitotic
118 spindle in eukaryotic cells, pushing newly replicated plasmids to opposite cell poles by
119 incorporating new ParM subunits at the ParRC-bound filament ends[29,30,32]. Whether the
120 chromosomal ParMR systems of multicellular cyanobacteria segregate chromosomes has not
121 been shown so far.

122 Here, we set out to understand the function of the chromosome-encoded ParMR
123 system in *Anabaena*. To our surprise, we found that this system – and those of other
124 multicellular cyanobacteria - have undergone extensive evolutionary diversification such that
125 they now control cell shape. This functional repurposing of an existing bacterial cytoskeleton –
126 from DNA segregation to cell shape control - reveals an unexpected evolutionary innovation in
127 bacterial intracellular organization coinciding with the emergence of multicellularity.
128

129 **Results:**

130 **A chromosomal ParMR system not involved in DNA segregation**

131 While looking for proteins involved in division, growth and cell-cell communication in
132 multicellular cyanobacteria[19], we discovered a chromosome-encoded ParMR system in
133 *Anabaena* (which we first called chrParMR; Fig. 1A). This finding was surprising, as ParMR
134 systems have until recently[34] only been described on plasmids, with a single complete
135 chromosomal ParMR system reported in *K. pneumoniae*[35] and few chromosomal ParR
136 homologs in select *Enterobacteriaceae* species[36] - though the function of these chromosomal
137 systems remains unknown. *Anabaena* has about 8 chromosome copies and how they are
138 maintained during cell division remains unknown[21,23]. We therefore speculated that the
139 chrParMR system may function as a chromosome segregation machinery.

140 Compared to other plasmid-encoded ParMR such as the *E. coli* ParMR (EcParMR)
141 from the R1 plasmid[37], the chrParMR of *Anabaena* does not have *parC*-like DNA repeats[38–40].
142 In addition, the proteins are longer and share only limited sequence identity of 20-30% with the
143 other ParMR proteins, contrasting the relatively high sequence identity of the plasmid-encoded
144 EcParM with the chromosomal *K. pneumoniae* ParM (KpParM) (~54 %) (Fig. 1B). Structure
145 predictions indicated that chrParM contains an extensive N-terminal intrinsically disordered
146 region (IDR), which is absent in EcParM (Fig S1A) and KpParMR. Both chrParR and EcParR
147 are ribbon-helix-helix (RHH) domain containing proteins (Fig 1C, S1B), which are typically
148 dimers and bind DNA[41]. chrParR is predicted to lack helices H3 and H4, which are
149 characteristic for canonical ParR proteins, while helix H5 appears to be divided into two
150 segments - a long H5a and a short H5b segment - connected by an IDR that is not present in
151 EcParR (Fig 1C, S1B). Notably, in *E. coli*, helix H5 mediates ParMR interactions[42].

152 We first conducted a phylogenetic analysis to identify other chromosomal ParMR
153 systems within cyanobacteria and other bacterial species. As the sequence conservation
154 among ParR homologs (Fig. 1B) is low we performed this analysis looking for ParM homologs
155 by sequence similarity and identifying ParR homologs based on their genomic context and 3D
156 structure prediction. We limited our search to fully sequenced species with closed

157 chromosomes and plasmids to unambiguously distinguish plasmid-encoded from
158 chromosomal ParMR systems. The phylogeny reconstructed from the identified ParM protein
159 sequences (Fig. 1D) shows that all cyanobacterial sequences are monophyletic, suggesting a
160 common origin. However, we observed three distinct clades of ParMR systems in
161 Cyanobacteria (Fig. 1D; Supplementary File 1), including two evolutionarily distant clades
162 whose proteins are mostly plasmid-encoded (yellow and salmon). Of these only the ParMR
163 proteins from the yellow clade structurally resembled previously described plasmid segregation
164 systems, based on their 3D structure prediction and automatic annotation[36,43]. One well-
165 separated clade containing only chromosomal ParMR systems (green) is restricted to the
166 orders *Nostocales* (including *Anabaena*) and *Oscillatoriales*. Within our representative
167 sampling of 148 fully assembled cyanobacterial genomes, we found a chromosomal ParMR
168 system in every *Nostocales* and *Oscillatoriales* genus analyzed, suggesting that its
169 evolutionary emergence likely traces back to an ancestor of these two multicellular
170 cyanobacterial orders. Notably, extended N-terminal IDRs were restricted to the green clade
171 of chromosomal ParMs and are largely absent in the plasmid-encoded clades (Fig. S1C). ParM
172 sequences identified in other bacterial phyla do not show monophyly within phyla, suggesting
173 horizontal gene transfer between species. Surprisingly, we found chromosomal ParMR
174 systems in a broad spectrum of bacterial species, challenging the notion of ParMR as a sole
175 plasmid segregation system. Chromosomal ParM sequences appear scattered throughout the
176 phylogenetic tree and are widely distributed. Indeed, when we searched for proteins identical
177 to *E. coli* ParM from the R1 plasmid (WP_000959884.1) in all *E. coli* assemblies available in
178 the NCBI RefSeq Genome database, we found 365 occurrences in plasmids and 12 in
179 chromosomes, indicating that such exchanges occur even among different strains of the same
180 species. When present in the chromosome, we identified a transposase gene
181 (WP_001067858.1) in the same genomic context as *parM*, supporting the incorporation of the
182 gene from a mobile element.

183 Together, these findings suggest that during bacterial evolution, the ParMR system has
184 likely been exchanged between bacterial chromosomes and plasmids multiple times during

185 evolution undergoing both vertical and horizontal transfers between species. In contrast, our
186 results indicate that the evolutionary history of the ParMR systems in Cyanobacteria is more
187 constrained, with two ancestral duplications and an inferred event of chromosomal integration
188 that has been vertically inherited from an ancestor of *Nostocales* and *Oscillatoriales*.

189 To test the hypothesis that chrParMR is involved in chromosome segregation in
190 *Anabaena*, we generated a Δ*parMR* mutant and assessed general DNA distribution and
191 segregation using DAPI staining. Contrary to our initial hypothesis, we observed no obvious
192 defects in cellular DNA distribution or any anuclear cells (Fig. 1E, I) as are commonly observed
193 in strains deficient in other types of chromosome segregation systems[44–46]. Instead, the mutant
194 showed a striking change in cell morphology, losing the characteristic barrel-like shape of the
195 wild type (WT) and forming enlarged and rounded cells instead (Fig. 1E). Δ*parMR* cells
196 displayed a near 1:1 aspect ratio, with width (3.88 ± 0.56 μm) approximately equal to length
197 (4.53 ± 0.47 μm), contrasting WT cells (length: 4.8 ± 0.96 μm, width: 2.89 ± 0.35 μm) (Fig. 1F-
198 H). This morphological change was accompanied by a slight reduction in fitness (Fig. S1D),
199 likely due to defects in septum maturation or completion as identified by scanning electron
200 microscopy (SEM) (Fig. S1E). Overall, the Δ*parMR* phenotype resembles a previously
201 described *Anabaena* Δ*mreB* strain[22], suggesting a similar function in cell shape control.
202 Complementation of the mutant only partially rescued the aberrant cell shape phenotype (Fig.
203 S1F), likely due to high levels of protein expression from the *parMR* promoter. We could not
204 recapitulate the native *parMR* expression levels through heterologous expression since the
205 native *parMR* promoter is also employed by *E. coli* and strains carrying plasmids with P_{parMR}-
206 *parM-parR* could not be generated, likely due to the toxic effects of ParR overexpression (Fig.
207 S1G). Based on these observations, we conclude that the *Anabaena* chrParMR system
208 represents a unique variant of the ParMR family that plays a role in cell shape control, rather
209 than in DNA segregation.

210 ***Anabaena's* chrParM forms dynamically instable cortical filaments *in vivo***

211 To localize chrParM within *Anabaena*, we used a CRISPR-Cpf1 system and generated a strain
212 in which the 5' end of chr*parM* is translationally fused to mNeonGreen (mNG), resulting in sole
213 expression of the tagged protein[47]. We note that the mNG-chrParM fusion protein is not fully
214 functional, as evidenced by a mild alteration in cell morphology (Fig. 2A, S2A). C-terminal
215 fusions could not be generated due to the presence of the chr*parR* ribosomal binding site within
216 the 3' end of chr*parM*. Unlike EcParM, which forms cytoplasmic filament bundles[2],
217 fluorescence imaging of live cells showed that chrParM assembled into filament arrays along
218 the inner cell membrane, with no association to the intracellular thylakoid membranes or the
219 cellular DNA (Fig. 2A-C). These filaments aligned perpendicular to the cell's long axis, with a
220 mean angle of 88.3 ± 12.15° (Fig. 2D). Time lapse microscopy of dividing cells revealed a cell
221 cycle-dependent distribution of chrParM filaments. During cell elongation chrParM is more and
222 more excluded from the cell poles and the future division sites. Right after division chrParM is
223 completely absent from the new cell poles (Fig. 2E; Supplementary Movie 1), suggesting active
224 mechanisms limiting its cellular distribution. Using total internal reflection fluorescence (TIRF)
225 microscopy, we then imaged the polymerization dynamics of chrParM in living cell. Consistent
226 with previously described plasmid-encoded ParMs[48,49], chrParM exhibits dynamic instability *in*
227 *vivo* (Fig. 2F,G; Supplementary Movie 2), with a filament growth rate of 18.96 ± 3.609 nm/s for
228 mNG-chrParM (Fig. 2H), approximately half that of EcParM[48]. Filaments also underwent rapid
229 shrinkage at a rate of at least 52.06 ± 23.54 nm/s, about one-fifth of the shrinkage rate
230 observed in *E. coli*[48]. Expressing an mNG fusion of a chrParM variant lacking the N-terminal
231 IDR (i.e., the first 40 amino acids; $^{\Delta 1\text{-}40}$chrParM) resulted in more severe morphological defects
232 than the strain expressing mNG-tagged full-length chrParM (Fig. S2A), indicating that the N-
233 terminal IDR is essential for maintaining proper cell shape in *Anabaena*. While mNG-$^{\Delta 1\text{-}}$
234 ^{40}chrParM still predominantly localizes perpendicular to the long cell axis, we observed a
235 generally less ordered mesh-like filament arrangement with occasional localizations to the
236 division site (Fig. S2B). Interestingly, although dynamic instability was retained (Fig. S2C), the
237 N-terminal deletion significantly increased the filament growth rate to 36.14 ± 8.035 nm/s (Fig.

238 S2D). Thus, chrParM maintained the polymerizing properties of EcParM, including the dynamic
239 instability, but exhibits a vastly different cellular localization pattern with dynamic properties
240 dependent on the N-terminal IDR absent in plasmid-encoded ParMs.

241 To assess the role of chrParR for chrParM localization, we ectopically expressed mNG-
242 chrParM from a replicative plasmid in Δ*parMR*. Here, in the absence of chrParR, we observed
243 mNG-chrParM filaments appearing in the cytoplasm of the cells without a clear localization
244 pattern (Fig. 2I), suggesting that chrParR is essential for the organization of chrParM into a
245 cortical array. Genomic replacement of chrParR with an mNG-tagged variant (chrParR-mNG)
246 as the sole gene copy confirmed its localization to the cell envelope (Fig. S2E). The
247 accumulation of chrParR-mNG signal at the cell poles is likely an artifact resulting from the
248 close proximity of two neighboring cell membranes at these sites, where signal from adjacent
249 cells merges due to the resolution limits of fluorescence microscopy. However, the swollen and
250 rounded phenotype of this strain indicates that the fusion protein is not fully functional,
251 suggesting that an unmodified C-terminus is essential for chrParM binding (Fig. S1E, F) similar
252 to what was previously reported for EcParR[36,42].

253 In summary, *Anabaena*'s chrParM and chrParR proteins form an evolutionarily distinct
254 ParMR system, whose deletion results in a pronounced cell shape defect. Using fluorescent
255 versions of the protein, we found that this actin-related protein assembles into a cortical array
256 of membrane-associated filaments. Together, these findings strongly suggest that chrParMR
257 is not involved in DNA segregation. According to their intracellular localization and cellular
258 function, we therefore propose to rename chrParM and chrParR as CorM and CorR,
259 respectively, to reflect their <u>cor</u>tical cytoskeletal organization.

260

261 ***In vitro* characterization of the CorMR system**

262 To biochemically characterize CorM, we purified the protein via heterologous
263 expression in *E. coli*. CorM retained ATPase activity but in contrast to EcParM, showed
264 negligible GTPase activity (Fig. S3A), and was unable to polymerize in the presence of GTP
265 and only weakly polymerized in the presence of AMP-PNP, a non-hydrolyzable ATP analog

266 (Fig. S3B-D). ATP hydrolysis by CorM increased with protein concentration (Fig. S3E), while
267 high-speed pelleting assays did not indicate a clear critical concentration for polymerization
268 under the tested conditions (Fig. S3F). Interestingly, deletion of the N-terminal IDR ($^{\Delta 1–40}$CorM)
269 led to elevated ATPase activity (Fig. S3G), indicating that the IDR modulates polymerization
270 kinetics.

271 We next confirmed interaction between CorM and CorR (Fig. S3H) in high-speed co-
272 pelleting assays (Fig. S3I, J), as well as through bacterial two-hybrid (B2H) screens (Fig. S3K).
273 Using CorR mutants, we confirmed that this interaction is mediated by CorR's helix H5b (Fig.
274 S3K), consistent with the *E. coli* ParMR system,

275 In plasmid-based ParMR systems, DNA segregation depends on ParR binding to *parC*
276 repeats (see for example [33,36,50]). To determine whether CorR also binds to DNA, we performed
277 electrophoresis mobility shift assays (EMSA) using the promoter region of *corMR* and *E. coli*
278 *parMR* as bait. CorR failed to bind DNA even at high concentrations (Fig. 3A), whereas EcParR
279 produced a clear mobility shift (Fig. 3A).

280 Sequence analysis using AmphipaseeK[51] revealed an N-terminal amphipathic helix
281 (AH) in CorR's first 10 amino acids, located just upstream of the $(RHH)_2$ domain (Fig. 3B). We
282 confirmed membrane binding of CorR in vesicle co-sedimentation assays, where the protein
283 was only found in the pellet in the presence of multilaminar vesicles (MLVs) (Fig. 3C, S4A).
284 Furthermore, CorM co-sedimented with MLVs mostly only in the presence of CorR, confirming
285 that CorR recruits CorM to lipid membranes. Although deletion of CorM's N-terminal IDR did
286 not impair its recruitment to the pellet by CorR, $^{\Delta 1\text{-}40}$CorM exhibited increased pelleting
287 compared to the full-length CorM, suggesting that the N-terminal IDR contributes to filament
288 length control or bundling (Fig. S4B, C). In contrast, deletion of CorR's N-terminal AH ($^{\Delta 1\text{-}}$
289 ^{10}CorR) abolished CorR's ability to bind MLVs and to recruit CorM (Fig. 3C, S4A). Meanwhile,
290 a CorR variant lacking the C-terminal α-helix (amino acid residues 150-162; CorR$^{\Delta 150\text{-}162}$)
291 retained lipid-binding capacity but failed to recruit CorM (Fig. 3C, S4A), consistent with our
292 B2H results (Fig. S1E). Together with our observation of cytoplasmic CorM filament bundles
293 in cells missing CorR, this suggests that CorR acts as a membrane tether for CorM filaments.

294 Next, we were wondering if other bacterial ParRs have acquired an N-terminal AH
295 suggesting membrane- instead of DNA-binding. However, by analyzing the protein sequence
296 of all cyanobacterial ParRs, we found that only CorR homologs from *Nostocales* and
297 *Oscillatoriales* cyanobacteria (Fig 3D) contain an AH, with strong sequence conservation in
298 *Nostocales* but not in *Oscillatoriales* species (Fig. S4D, S5). This suggests that the acquisition
299 of *corR* in the chromosome and the emergence of this membrane binding motif have a common
300 origin.
301 Together, these findings provide the first evidence for a ParR homolog that has lost its
302 DNA-binding capacity and instead evolved the ability to bind membranes, mediated by a newly
303 acquired amphipathic helix at the N-terminus of the $(RHH)_2$ domain.
304
305 **CorM assembles into antiparallel, double-stranded helical filaments**
306 Given the unexpected behavior of the CorMR system, we aimed to gain structural insights into
307 the molecular architecture of CorM filaments and their interaction with CorR. To this end, we
308 performed single particle analysis cryo-electron microscopy (cryo-EM) of filaments consisting
309 of solely CorM, $^{\Delta 1\text{-}40}$CorM or CorM assembled in the presence of CorR (CorMR) (Fig. 4A, S6.1-
310 6.4). We included $^{\Delta 1\text{-}40}$CorM to investigate if the unusually long N-terminal part of CorM might
311 play a structural role in filament assembly. For all three samples, we obtained electron
312 microscopy density maps at resolutions that allowed unambiguous assignment of individual
313 CorM subunits (Fig. 4B, S6.1-6.4), revealing in each case that CorM filaments consist of two
314 antiparallel, unstaggered protofilaments forming a left-handed helix. Our structures also show
315 that both deletion of the N-terminal amino acids as well as the presence of CorR in the *in vitro*
316 assembly do not visibly alter filament architecture (Fig. S6.1-6.4). However, we observed that
317 CorM alone forms shorter filaments in our *in vitro* preparation (Fig. S6.3) and that these
318 filaments had a slightly differing rise and twist (46.5 Å/-18.5°) as compared to the other two
319 structures (CorMR: 46.427 Å/-15.75°; $^{\Delta 1\text{-}40}$CorM 47.294 Å/-15.344°) (Fig. S6.1-6.2). Since the
320 CorMR sample reached the highest resolution (3.9 Å as compared to 4.4 Å for $^{\Delta 1\text{-}40}$CorM and
321 7.1 Å for CorM alone), we used this electron microscopy density map to build a molecular

322 model of the CorM filament (Fig. 4C, D). Upon closer inspection of the maps fitted with the
323 molecular model, we found that the 40 N-terminal amino acids do not adopt a structured
324 conformation in either of the CorM or CorMR samples. Similarly, within the CorMR filament
325 structure all visible density was occupied by CorM alone, which suggests that CorR only binds
326 to the filament ends, as has been shown for other ParR systems[30]. Given the non-staggered
327 nature of the filament assembly, the lateral association of the two CorM protofilaments
328 (designated n and n* in Figure 4D) is only established by interactions of always only two
329 neighboring subunits. Analysis of our model using PDBePISA[52] shows only weak hydrogen
330 bond interactions across a small lateral interface (interface area 452.2 $Å^2$) (Figure 4E). Hence,
331 it seems CorM forms weaker lateral interactions compared to EcParM, where multiple lateral
332 interactions between the protofilaments are determined by salt bridges[32]. This potentially has
333 implications in filament stability or dynamic behavior of CorM. Further cryo-EM processing to
334 obtain a higher resolution structure and a structure of filament ends will be required to further
335 characterize the lateral interactions as well as how CorR interacts with CorM.

336 In contrast, the longitudinal interactions between CorM subunits along the filament are
337 extensive (interface area 1466.7 $Å^2$) and involve multiple salt bridges and hydrogen bonds
338 (Fig. 4F), similar to EcParM filaments[32]. Interestingly, EcParM filaments have been described
339 to form parallel, polar and staggered helices, which is drastically different from the antiparallel,
340 non-polar and non-staggered assembly of CorM (Figure 4G). Instead, the filament architecture
341 of CorM more closely resembles the antiparallel, non-polar filament doublets formed by MreB
342 (Figure 4G), although MreB does not adopt a helical conformation and does not show dynamic
343 instability.

344 In summary, our cryo-EM analysis shows a novel filament architecture with in the ParM
345 family formed by our CorM filaments, underscoring the uniqueness of the CorMR system
346 relative to plasmid-encoded, DNA-segregating ParMR systems.

347 **Reconstitution of CorM dynamics *in vitro* on supported lipid bilayers**

348 We next asked whether CorM dynamics could be reconstituted on membranes *in vitro*. To this
349 end, we used supported lipid bilayers (SLBs), as previously described for the cytoskeletal
350 system formed by FtsZ and FtsA[4] (Fig. 5A). Indeed, we successfully recapitulated the *in vivo*
351 behavior of CorM and CorR *in vitro* (Fig. 5B), demonstrating that these two proteins are
352 sufficient to drive filament formation and dynamics.

353 When Alexa488-labeled CorM was added to SLBs in the presence of CorR, it initially
354 assembled into individual filaments that tended to swivel on the membrane surface. Over time,
355 these filaments formed stable and increasingly dense networks, eventually giving rise to a
356 highly complex filamentous mesh (Fig. 5B). We saw the same filament assembly phenotype
357 over a range of CorM concentrations (from 1-2.5 μM). Fluorescence recovery after
358 photobleaching (FRAP) experiments confirmed the dynamic nature of CorM filaments *in vitro*
359 (Fig. S7A; Supplementary Movies 4), and filament turnover rates increased with rising
360 concentrations of CorR (half recovery times ($T_{1/2}$) for different CorR concentrations: 0.125 μM:
361 10.64 ± 0.87 s; 0.25 μM: 6.97 ± 0.24 s; 0.75 μM: 4.94 ± 0.14 s) (Fig. S7B).

362 The $^{\Delta 1–40}$CorM mutant retained dynamic behavior, although FRAP recovery was
363 significantly slower than for the WT protein ($T_{1/2}$ WT: 10.64 ± 0.87 s; $T_{1/2}$ $^{\Delta 1–40}$CorM: 24.65 ±
364 1.22 s) (Fig. S7A, C, D; Supplementary Movie 5). Notably, filament architecture differed
365 substantially: while initial filament formation resembled that of WT CorM, $^{\Delta 1–40}$CorM ultimately
366 formed a much more ordered and aligned network (Fig. S7E), again suggesting that the IDR
367 modulates filament architecture over time.

368 Consistent with observations in live cells, CorM filaments displayed dynamic instability
369 *in vitro*, undergoing repeated cycles of growth and sudden shrinkage events (Fig. 5C-E;
370 Supplementary Movie 6). Growth was observed at both filament ends (Fig. 5F–I;
371 Supplementary Movie 7), with a mean growth velocity of 76.63 ± 19.23 nm/s (Fig 5I),
372 comparable to EcParM[49]. Dual-color imaging, where individual monomers were labeled with a
373 different fluorophore than the rest of the filament, revealed that while filaments grew at both
374 ends, individual monomers within the filament remained static (Fig. 5F-H). Intriguingly, when

375 we quantified bidirectional growth, we saw that one filament end grew slightly faster than the
376 other (faster end: 35.85 ± 5.53 nm/s; slower end: 23.53 ± 5.36 nm/s). On average resulting in
377 a net unipolar growth rate of 29.69 ± 8.28 nm/s (Fig. 5I). As the two ends are structurally
378 identical, we assume that the observed kinetic difference is likely due to only one filament end
379 being engaged by CorR at a given time. End-binding of CorR would also be consistent with
380 previous reports on the ParMR system[42] and would also align with the observed swiveling
381 motion of CorM filaments on membrane surfaces. Due to its small size and the essential roles
382 of its N- and C-termini, we were unable to generate a fluorescently labeled version of CorR to
383 verify this assumption. Shrinkage occurred at a much higher rate, with mean disassembly
384 velocities of -1313.42 ± 671.54 nm/s (Fig. 5I), approximately eight times faster than previously
385 reported for EcParM[49].
386
387 **Control of CorMR filaments by the Min system**
388 Plasmid-encoded ParMR systems typically function independently of host regulation and no
389 other regulators or interactors have been described to date. In contrast, the distinct filament
390 pattern of CorM *in vivo* (Fig. 2A) and the pronounced phenotype observed upon CorMR
391 deletion (Fig 1D) suggest active spatial regulation of CorM polymerization and possible
392 interactions with proteins involved in cell wall remodelling.
393 To identify putative binding partners for CorM, we performed an *in silico* screen using
394 AlphaFold-Multimer[53,54] of CorM against the entire *Anabaena* proteome (Fig. 6A;
395 Supplementary File 2). This approach uses structural predictions of pairwise protein-protein
396 interactions and ranks them according to their interface-predicted template modeling score
397 (ipTM score). Consistent with our experimental data, the top-ranking predictions included
398 CorM-CorR (rank 8) and CorM-CorM (rank 12) interactions, both with ipTM scores above 0.65.
399 Notably, MinC - a well-characterized inhibitor of FtsZ polymerization and an element of the Min
400 system[55] - ranked second in the list, with an ipTM score of 0.77 (Fig. 6A, Fig. S8A). This
401 unexpected prediction raised the possibility that, in multicellular cyanobacteria, MinC may
402 regulate not only the Z-ring formation but also the CorMR system.

403 To experimentally validate these interactions, we first used B2H assays, which
404 confirmed that CorM interacts with MinC and revealed that CorR also interacts with MinC (Fig.
405 S8B). However, neither CorM nor CorR interacted with MinD or MinE (Fig. S8D). Additionally,
406 CorR was found to interact with Cdv3 (Fig. S8C), a cyanobacteria-specific component of the
407 Min system[14,18]. MinC interacted with Cdv3 and – as expected from prior findings in *E. coli,*
408 with MinD and MinE (Fig. S8E).

409 Interestingly, we found that MinC proteins from multicellular cyanobacteria - particularly
410 of *Nostocales* - are substantially longer on average than their counterparts in unicellular
411 cyanobacteria or other bacteria (Fig. 6B, S9; Supplementary File 3). Multiple sequence
412 alignments showed that this length increase is always due to MinC's N-terminal extension,
413 which is unique to *Nostocales* cyanobacteria (Fig. S9).

414 Structural predictions suggest that this region is intrinsically disordered and includes a
415 short α-helix (Fig. 6C, S8A). We superimposed the predicted structures of CorM-CorR and
416 CorM-MinC (compare Fig. S3H and S8A) and found that of MinC's N-terminal α-helix binds to
417 the same pocket on CorM as the C-terminal α-helix of CorR (Fig 6C). This suggests that CorR
418 and MinC compete for CorM binding. Notably, this binding pocket of CorM is well conserved
419 among chromosomal CorM homologs while highly variable in plasmid-encoded ParMs (Fig.
420 S10A), highlighting its likely relevance in regulating CorM's function.

421 *In vivo*, we found that MinC oscillates from pole to pole (Fig. 6D, E; Supplementary
422 Movie 8), as previously described for unicellular bacteria such as *E. coli*[56,57]and the rod-shaped
423 cyanobacterium *S. elongatus*[18]. This provides the first evidence that robust Min system
424 oscillation can also occur in multicellular bacteria. As described in *S. elongatus*, MinC forms
425 local maxima at the cell poles and at the sites of active constriction (Fig. S10B). This
426 localization pattern is mutually exclusive with CorM, which is excluded from these sites,
427 suggesting spatial antagonism. Unfortunately, due to the strong chlorophyll A autofluorescence
428 of cyanobacterial thylakoid membranes, dual-color imaging using green and red fluorophores
429 is currently not feasible, limiting our ability to directly co-visualize MinC and CorM.

430 To test for the functional relevance of the CorM and MinC interaction, we performed *in*
431 *vitro* pelleting assays with CorM under polymerizing conditions while titrating MinC. We found
432 that MinC potently depolymerized CorM in a concentration dependent manner (Fig. 6F, S10C).
433 This effect was abolished when we mutated conserved residues in the N-terminal α-helix of
434 MinC (S50A+L55D, Fig. S10D) or deleted the entire helix (residues 46-67) (Fig. 6G, S10E).
435 No effect was observed upon addition of a synthetic peptide mimicking MinC's N-terminal α-
436 helix, suggesting that additional elements of MinC are needed to promote CorM disassembly
437 (Fig. 6G). Depolymerization of CorM filaments was also observed *in vitro* on SLBs upon
438 addition of WT MinC but not with the mutant variants or buffer control (Fig. 6H, I;
439 Supplementary Movies 9-12). Moreover, MinC addition reduced CorM ATPase activity (Fig.
440 S10F), suggesting a sequestering mechanism of filament depolymerization as described for
441 inhibitory proteins of actin[58–60], tubulin[61] or FtsZ[62] polymerization and providing a mechanistic
442 link between MinC and filament disassembly. Finally, using the B2H system, we confirmed that
443 the N-terminal helix is essential for MinC's ability to interact with CorM (Fig. S10G).
444 Taken together, these findings reveal a novel regulatory role for the Min system in
445 multicellular cyanobacteria. Beyond its established role in regulating Z-ring positioning, MinC
446 modulates the CorMR system by directly competing with CorR for CorM binding, thereby
447 spatially restricting CorM polymerization and contributing to cell shape control.
448
449 **Discussion:**
450 This study uncovers the functional repurposing of a protein system - from plasmid segregation
451 to cell shape control. In multicellular cyanobacteria, the canonical plasmid segregating ParMR
452 system has undergone substantial evolutionary adaptation to form the cortical CorMR
453 cytoskeleton on the cell membrane (Fig. 7A). This adaptation seems to be specific to
454 *Nostocales* and *Oscillatoriales* cyanobacteria, most of which retain plasmid-encoded ParMR
455 systems in addition to the chromosomal CorMR system.
456 The evolutionary history of ParMR appears to be complex, shaped by multiple
457 horizontal transfers, gene duplications, and transfer between plasmids and chromosomes.

458 These results challenge the notion that ParMR systems solely act as plasmid segregation
459 systems, and detailed, lineage-specific analyses will be necessary to determine whether
460 ParMR systems have acquired distinct functions independently in other groups. In
461 Cyanobacteria, however, the evolutionary trajectory seems more straightforward, involving two
462 ancestral duplications and some lineage-specific chromosomal acquisition, with a single
463 chromosomal incorporation that has been transmitted vertically. Besides CorMR, two broadly
464 distributed plasmid-associated ParMR clades are observed: one is known to mediate plasmid
465 copy number regulation and partitioning, while the function of the other remains unknown.
466 Observations from both bacterial and cyanobacterial phylogenetic relationships raise the
467 question of whether the ParMR system is more functionally plastic than previously recognized
468 and might have been repurposed multiple times during evolution.

469 The transition from plasmid segregation to cell shape control is accompanied by several
470 structural and functional innovations. Most prominently, the associated adaptor protein, CorR,
471 has acquired an N-terminal amphipathic helix that enables membrane association while
472 classical ParR proteins bind DNA. Our cryo-EM structure also reveals that CorM filaments form
473 antiparallel filament bundles, in contrast to ParM which forms polar double-stranded
474 filaments[30]. We also find that the canonical cell division regulator MinC has acquired a novel
475 regulatory role. In *Nostocales*, MinC has an extended N-terminal intrinsically disordered region
476 containing short α-helical motif, which binds a conserved pocket in CorM. Here, MinC
477 competes with CorR binding on the one hand and also with CorM polymerization, potentially
478 through a sequestration mechanism similar to what was reported for actin[58–60], tubulin[61] or
479 FtsZ[62]. In contrast to MinC's effect on FtsZ, which does not affect FtsZ's GTPase activity, we
480 observed a reduction in CorM's ATPase activity in the presence of MinC, suggesting that
481 additional mechanisms beyond mere sequestration may be involved. As a result, MinC is able
482 to efficiently depolymerize and remove CorM filaments from supported membranes *in vitro* as
483 well as from the cell poles *in vivo*. This dual functionality of a Min gradient - regulating both
484 FtsZ and CorM - is, to our knowledge, unprecedented and suggests an expanded role for the
485 Min system in the cytoskeletal organization of multicellular cyanobacteria (Fig. 7A, B).

486 The cell shape phenotype of Δ*corMR* and Δ*mreB*[22] observed in *Anabaena* suggests a
487 role for CorMR as a spatial coordinator of PG biogenesis, while the precise molecular
488 interactions between CorMR and the PG synthesis machinery are currently under investigation
489 and will be addressed in subsequent studies. This function is also reminiscent of plant root
490 cortical microtubules (prcMTs), which guide cellulose synthase complexes to shape plant
491 cells[63–65]. Both systems operate through transversely oriented polymers and likely act in
492 concert with cell wall synthases to control cell shape. Although CorM is an actin homolog and
493 prcMTs are built from tubulin, the mechanistic parallels suggest an important role of dynamic
494 instability to orient a cortical cytoskeleton perpendicular to the cell axis, a potential case of
495 convergent evolution of their functions.

496 Interestingly, while Δ*corMR* and Δ*mreB*, Δ*mreC* or Δ*mreD* mutants exhibit similar
497 morphological phenotypes - a swollen or rounded and enlarged cell[20,22] - neither system is
498 essential for viability in *Anabaena*, even under nitrogen starvation conditions that typically
499 fragment cell filaments. This observation contrasts with the essential role of MreBCD in rod-
500 shaped unicellular cyanobacteria and in most other bacteria[26,66–68], highlighting the robustness
501 and redundancy of morphogenetic systems in multicellular cyanobacteria.

502 CorM and MreB form antiparallel, double-stranded filaments, where individual
503 protofilaments have opposite orientation[69]. In contrast to MreB filaments, whose motion relies
504 on PG synthesis[6,70], we find that CorMR filaments exhibit dynamic instability both *in vivo* and
505 *in vitro*, similar to its ancestor ParM. Unlike canonical polymeric systems composed of actin,
506 tubulin, ParM, or FtsZ, which are intrinsically polar and stabilized through nucleotide caps at
507 their structurally distinct plus ends[32,49,71,72], CorM filaments are antiparallel, and thus both
508 filament ends are structurally and kinetically identical. Accordingly, the classic nucleotide cap
509 model for dynamic instabilities of microtubules[73] cannot be applied here and additional
510 mechanistic studies are necessary to reveal how this is achieved in a non-polar, antiparallel
511 filament.

512 Despite the symmetry of CorM filaments, we observed slightly different growth
513 velocities at the two ends *in vitro* (Fig. 5I) and apparent uni-directional growth *in vivo* (Fig. 2F,

514 G). We believe that these asymmetric growth kinetics arises from the interaction with CorR.
515 Based on the previous observations of a clash between the C-terminal peptide of ParR with a
516 ParM monomer within the ParM filament[42] and the stabilization of the ATP cap at the filament
517 end during growth[49], we believe that CorR competes with the addition of another CorM
518 monomer during polymerization. Such a competition between CorR and CorM at one of the
519 two ends could not only explain asymmetric growth kinetics, but also the characteristic
520 swiveling of membrane-bound CorM filaments and accelerated CorM turnover at higher CorR
521 concentrations (Fig. S7B).
522 The CorMR system exemplifies evolutionary innovation, having been repurposed from a
523 plasmid segregation module into a membrane cytoskeleton that controls cell shape (Fig. 7C).
524 In addition, our findings establish the chromosomal CorMR as a novel membrane-associated
525 actin system in bacteria that assembles into non-polar, dynamically instable filaments. Our
526 findings highlight the plasticity of bacterial cytoskeletal systems and demonstrate how pre-
527 existing modules can be co-opted and functionally diversified to serve novel cellular roles,
528 offering insights into the evolution of cellular and multicellular complexity.
529
530 **Supplemental material:**
531 Supplementary Movie 1: Live cell time lapse microscopy of mNG-CorM
532 *Anabaena* cells expressing mNG-CorM were grown on 1.5% agar pads and illuminated with
533 an in-house plant growth light. Images were acquired at 15-minute intervals. Scale bar: 5 µm.
534 Supplementary Movie 2: Dynamic instability of mNG-CorM *in vivo*
535 Polymerization and sudden shrinkage of mNG-CorM filaments in *Anabaena* cells recorded by
536 TIRF microscopy. Images were acquired at 10-second intervals. Scale bar: 1 µm.
537 Supplementary Movie 3: Dynamic instability of mNG-$^{\Delta 1\text{-}40}$CorM *in vivo*
538 Polymerization and sudden shrinkage of mNG-$^{\Delta 1\text{-}40}$CorM filaments in *Anabaena* cells recorded
539 by TIRF microscopy. Images were acquired at 5-second intervals. Scale bar: 1 µm.
540 Supplementary Movie 4: FRAP of CorM *in vitro*

541 FRAP experiment of Alexa488-CorM filaments *in vitro* on SLBs. Images were acquired at 1-
542 second intervals. Scale bar: 10 µm.
543 Supplementary Movie 5: FRAP of $^{\Delta 1-40}$CorM *in vitro*
544 FRAP experiment of Alexa488-$^{\Delta 1-40}$CorM filaments *in vitro* on SLBs. Images were acquired at
545 1-second intervals. Scale bar: 10 µm.
546 Supplementary Movie 6: CorM polymerization dynamics *in vitro*
547 TIRF microscopy of Alexa488-CorM filaments on supported lipid bilayers. Individual filaments
548 can only be tracked during the early stages of polymerization. Images were acquired at 0.15-
549 second intervals. Scale bar: 2 µm.
550 Supplementary Movie 7: CorM dual color filament tracking *in vitro*
551 TIRF microscopy of Alexa488-CorM filaments with single Cy5-CorM monomers on supported
552 lipid bilayers. Images were acquired at 1-second intervals. Scale bar: 1 µm.
553 Supplementary Movie 8: Live cell time lapse microscopy of mNG-MinC
554 *Anabaena* cells expressing mNG-MinC were grown on 1.5% agar pads and images were
555 acquired at 1-minute intervals.
556 Supplementary Movie 9: CorM + MinC *in vitro*
557 TIRF microscopy of pre-assembled Alexa488-CorM filaments. MinC was added at equimolar
558 concentration after 30 seconds. Images were acquired at 1-second intervals. Scale bar: 5 µm.
559 Supplementary Movie 10: CorM + MinC$^{S50A+L55D}$ *in vitro*
560 TIRF microscopy of pre-assembled Alexa488-CorM filaments. MinC$^{S50A+L55D}$ was added at
561 equimolar concentration after 30 seconds. Images were acquired at 1-second intervals. Scale
562 bar: 5 µm.
563 Supplementary Movie 11: CorM + $^{\Delta 46-67}$MinC *in vitro*
564 TIRF microscopy of pre-assembled Alexa488-CorM filaments. $^{\Delta 46-67}$MinC was added at
565 equimolar concentration after 30 seconds. Images were acquired at 1-second intervals. Scale
566 bar: 5 µm.
567 Supplementary Movie 12: CorM + buffer ctrl. *in vitro*

568 TIRF microscopy of pre-assembled Alexa488-CorM filaments. Buffer was added at a volume
569 equivalent to that of MinC after 30 seconds. Images were acquired at 1-second intervals. Scale
570 bar: 5 µm.
571
572 Supplementary File 1: Taxonomic sampling and ParM and ParR NCBI protein identifiers for
573 the Cyanobacteria and Bacteria databases.
574 Supplementary File 2: CorM AlphaFold pulldown against *Anabaena* proteome
575 AlphaFold results testing CorM against the whole *Anabaena* proteome. To ease readability,
576 only one out of five predicted dimer models provided by AlphaFold is given.
577 Supplementary File 3: Taxonomic sampling and MinC NCBI protein identifiers for the
578 Cyanobacteria and Bacteria databases.
579
580 Supplementary Tables: Strains, plasmids and primers used in this study.
581
582 **Figure legends:**
583 **Figure 1: A ParMR system functioning in cell shape control**
584 (**A**) Schematic representation of the chromosomal *parMR* operon from *Anabaena*. The
585 promoter region is predicted to be about 400 bp long. Numbers below indicate genomic locus
586 position. (**B**) Sequence identity and similarity (in brackets) in percent of chrParMR from
587 *Anabaena* with chromosome-encoded KpParMR from *K. pneumoniae* and plasmid-encoded
588 ParMR from *E. coli* R1 plasmid. (**C**) Schematic representation of the chromosome and plasmid-
589 encoded ParM and ParR proteins from *Anabaena* and *E. coli*, respectively. chrParM contains
590 a N-terminal 40 amino acid (aa) long intrinsically disordered region (IDR) in addition to globular
591 domain observed in both, chrParM and EcParM. chrParR is longer than EcParR and lacks
592 helix H3 and H4. Instead, helix H5 appears to be split into one large helix (H5a) and one small
593 helix (H5b). Numbers indicate aa positions. (**D**) Maximum-likelihood phylogeny of bacterial
594 ParM. All cyanobacterial sequences (outlined with a dashed line) form a monophyletic clade.
595 Chromosome-encoded sequences are marked with a green background for Cyanobacteria,

596 and with a black dot for other bacterial phyla. The scale bar represents the average number of
597 substitutions per site. For the detailed tree, see Source Data. ParM proteins from the yellow
598 clade structurally resemble previously characterized plasmid segregation systems, whereas
599 the functions of ParM proteins from the green and pink clades remain unknown. (**E**)
600 Micrographs of *Anabaena* WT and Δ*parMR* cells showing an overlay of Direct Illumination
601 Acquisition (DIA) with chlorophyll a (chlA) autofluorescence images and DAPI staining from
602 the same cells. (**F-H**) Scatter plots showing the mean cell property values ± standard deviation
603 (SD) for (**F**) cell width (WT: 4.8 ± 0.96 µm; Δ*parMR*: 4.53 ± 0.47 µm), (**G**) cell length (WT: 2.89
604 ± 0.35 µm; Δ*parMR*: 3.88 ± 0.56 µm) and (**H**) cell aspect ratio (WT: 0.62 ± 0.13; Δ*parMR*: 0.86
605 ± 0.09) of *Anabaena* WT and Δ*parMR* cells. WT: n=222 cells; Δ*parMR*: n=259 cells. (**I**) Mean
606 DAPI fluorescence intensity from individual cells plotted against the normalized cell length (0
607 = one cell pole, 1 = opposite cell pole). Values for WT are shown in cyan and values for Δ*parMR*
608 are shown in grey. Shaded areas correspond to the SD around the mean. The intensity profiles
609 show a peak near the center of the cell, indicating midcell enrichment of DAPI signal, with
610 reduced signal toward the poles. WT: n=46 cells; Δ*parMR*: n=49 cells.
611
612 **Figure 2: CorM forms cortical filaments transverse to the long cell axis**
613 (**A**) Maximum intensity projection micrographs of *Anabaena* cells expressing mNG-ParM from
614 its native locus as the sole copy within the cell. Left: mNG-ParM fluorescence signal, middle:
615 overlap of mNG-ParM and chlorophyll A (chlA) autofluorescence (magenta), right: side view of
616 the left image. (**B**) Cross section view of the same cells as in (**A**) showing the middle plane of
617 the cells, highlighting that mNG-ParM and chlA signals do not overlap. Beige bar indicates
618 region used to measure the intensity plot profile from mNG-ParM and chlA signal as shown in
619 (C). (**D**) Angles of mNG-ParM filaments (n=386 filaments) in respect to the long cell axis.
620 Cartoon indicates process of angle measurement. (**E**) Dynamic localization of mNG-ParM
621 during the cell division cycle (see Supplementary Movie 1). The kymograph (center) shows the
622 mean fluorescence intensity of mNG-ParM over time from 56 dividing cells. Top and bottom
623 cell sketches indicate the chrParM patterns before and after cell division, respectively. Purple

624 horizontal bars indicate specific time points (~2.5 h, ~7.5 h, ~12.5 h), corresponding to intensity
625 profiles shown on the right. These profiles display the average distribution of mNG-ParM
626 intensities at three key division stages: during growth, before constriction, and after division.
627 Each line profile is the average signal from 3 micrographs taken within a 45-minute time
628 window (images were taken every 15 min). Intensity profiles correspond the normalized mean
629 fluorescence intensity signal from mNG-ParM, while shaded purple regions indicate the cell
630 boundaries. The SD of the cell boundaries is shaded in light purple (n=56). (**F**) Time series
631 from Supplementary Movie 2 displaying TIRF micrographs of individual mNG-ParM filaments
632 over a period of 180 seconds. White triangle marks the initial position of a mNG-ParM filament,
633 and the red triangle indicates its furthest observed position during the time series. (**G**)
634 Kymograph of individual mNG-ParM filaments from TIRF microscopy. White arrows indicate
635 growing filaments whereas magenta arrows indicate filament disassembly/shrinkage. (**H**)
636 Scatter plot showing the growth velocities (mean 18.96 ± 3.61 nm/s) of mNG-ParM filaments
637 as recorded by TIRF microscopy. Error bars represent the mean ± SD of 80 independent
638 filaments measured. (**I**) Micrograph showing merged DIA and mNG-ParM fluorescence images
639 of Δ*parMR* carrying a low copy number plasmid heterologously expressing mNG-ParM from a
640 synthetic *ntcA* promoter integrated into the neutral *thrS2* site on the *Anabaena* chromosome[74]
641 resulting in medium expression levels. Unlike in the WT, mNG-ParM loses its transverse
642 localization in the absence of ParR.
643
644 **Figure 3: CorR binds to lipid membranes and recruits CorM**
645 (**A**) EMSA assay with increasing concentrations of CorR or *E. coli* ParR using the promoter
646 region of *corMR* (400 bp) or *parC* (380 bp), respectively, as DNA bait. Concentrations in μM
647 are given above the individual lanes. Blot shows a representative example of six individual
648 experiments. (**B**) Left shows an AlphaFold3 prediction of a CorR dimer with C-terminal CorM
649 interaction site and N-terminal amphipathic helix (AH) indicated. The AH within the first 10 aa
650 was identified using Amphipaseek[51]. Notably, AlphaFold3 does not predict the N-terminal AH
651 as a helical structure but rather as an unstructured region. This may be because AHs often

652 exist as nascent helices that only adopt their proper fold upon contact with the membrane.
653 Right shows the helical wheel projection of the first 11 aa of CorR and *E. coli* ParR. Arrows
654 indicate the hydrophobic moment of the predicted helix indicating the amphipathicity of the
655 respective proteins. The high hydrophobic moment of CorR indicates the potential to bind to
656 lipid membranes at the interface between the lipid bilayer and the cytosolic phase. (**C**)
657 Representative Coomassie-stained SDS-PAGE gel of a pelleting assay with indicated protein
658 combinations with or without MLVs. 30 % of the total pellet [P] and 12.5 % of the total
659 supernatant [S] samples were separated on the gel. The respective quantifications are shown
660 in Fig. S3B. CorR is enriched in the pellet fraction in the presence of MLVs. CorM alone is not
661 efficiently pelleted at 21,000 x *g* but gets enriched in the pellet when co-incubated with CorR,
662 indicating that CorR recruits CorM to the MLV-containing pellet. CorR lacking the N-terminal
663 AH ($^{\Delta 1-10}$CorR) fails to bind MLVs and is thus not enriched in the MLV-containing pellet fraction.
664 In contrast, CorR$^{\Delta 150-162}$ retains the N-terminal AH and can be recruited to the pellet via MLV
665 interactions but cannot recruit CorM to the pellet due to the absence of the C-terminal peptide
666 required for CorM binding. Dotted lines separate individual gels stiched together for better
667 visualization. (**D**) Maximum-likelihood phylogeny based on the concatenation of CorM/ParM
668 and CorR/ParR sequences from Cyanobacteria. The presence of a predicted AH in CorR/ParR
669 cyanobacterial homologs is indicated with a red dot. *Anabaena* CorR is indicated with a red
670 circle. The scale bar represents the average number of substitutions per site. For the detailed
671 tree, see Source Data.
672
673 **Figure 4: Cryo-EM structure of *in vitro* reconstituted CorM filaments**
674 (**A**) Cryo-EM micrograph showing CorMR filaments formed in vitro at a protein concentration
675 of 5 µM for each CorM and CorR. (**B**) Cryo-EM density map of *in vitro* reconstituted wild type
676 CorM filament in the presence of CorR (CorMR) at 3.9 Å. The details of the cryo-EM processing
677 pipeline for all the three obtained structures are provided in Fig. S6.1-S6.3. (**C-D**) Refined
678 model of the CorM filament built by fitting the Alphafold-predicted CorM monomer into
679 CorM+CorR cryo-EM density map. ADP molecules are shown. (**E**) The two antiparallel

680 protofilaments are annotated as n and n*. Rectangles outline the enlarged lateral and
681 longitudinal interaction interfaces in **F**. Both of the interface interactions were determined using
682 PDBePISA (Proteins, Interfaces, Structure and Assemblies)[52]. (**G**) Comparison of surface
683 representations of CorM (this study), with previously published *E. coli* ParM (PDB entry 5AEY)
684 and *C. crescentus* MreB (PDB entry 4CZJ) models, respectively. Individual protofilaments are
685 colored in dark or light green to illustrate their relative arrangement. Similarities and differences
686 in polarity, subunit arrangement and helical parameters are given below the models.
687
688 **Figure 5: *In vitro* reconstitution of CorMR polymerization on supported membranes**
689 (**A**) Illustration of the experimental assay to reconstitute CorM polymerization with CorR on
690 supported lipid bilayers (SLBs). CorR binds to the SLB through its AH and recruits CorM
691 filaments to the membrane. CorM filaments grow from both sites through bidirectional addition
692 of monomers to an existing filament. (**B**) TIRF micrographs of purified and Alexa488-labeled
693 CorM (0.25 μM) together with unlabeled CorM (0.75 μM) recruited to the SLB through
694 interaction with CorR (0.25 μM). Initially, CorM forms individual filaments (left image) that then
695 eventually form a denser network of filaments (middle image), which ultimately merge into a
696 dense, seemingly highly interconnected meshwork of thin filaments (right image). (**C**) Time
697 series from Supplementary Movie 6 displaying TIRF micrographs of individual Alexa488-
698 labeled CorM filaments showing dynamic instability. Blue triangles mark the initial position of
699 an individual CorM filament that continues to grow throughout the whole time series. Orange
700 triangles mark the initial position of an individual CorM filament that grows initially and then
701 rapidly collapses before regrowing. The purple triangles indicate the furthest observed position
702 of another filament which ultimately undergoes rapid and complete depolymerization during
703 the time series. (**D**) Kymographs of the respective filaments marked with blue, orange and
704 purple triangles in (C) showing growth, catastrophe and rescue events. The filament indicated
705 with blue triangles only grows during the 120 sec time series shown in (C) and eventually also
706 undergoes depolymerization. The filament indicated with purple triangles grows bidirectionally
707 and then completely collapses. (**E**) CorM filament undergoing an initial polymerization phase

708 followed by rapid depolymerization. Growth is represented by the increase in distance between
709 the two poles of the filament over time. The filament polymerizes steadily at a rate of 96.95
710 nm/s (green line) followed by a rapid depolymerization phase with a rate of -958.07 nm/s
711 (orange line). (**F**) Time series from Supplementary Movie 7 displaying TIRF micrographs of an
712 individual Alexa488-labeled CorM filament supplemented with Cy5-CorM over a period of 32
713 seconds. Alexa488-CorM: 0.5 µM; Cy5-CorM: 4.48 pM; CorR: 0.25 µM. The Cy5-CorM
714 monomer within the Alexa488-CorM filament remains static while Alexa488-CorM monomers
715 are added to both filament poles. (**G**) Kymograph of CorM filament depicted in (F), confirming
716 the immobile nature of the Cy5-CorM monomer and the bipolar extension of the CorM filament.
717 (**H**) Start (triangle) and end (cross) positions of the two ends of the filament ends (light and
718 dark green) shown in (F) as well as the position of the Cy5-CorM monomer (orange) during
719 the time lapse. (**I**) Growth and shrinkage properties of CorM filaments from *in vitro* time-lapse
720 TIRF microscopy. Scatter plots show the mean ± SD filament velocities of Alexa488-CorM
721 during bipolar growth (76.63 ± 19.23 nm/s; n=13), unipolar growth (29.69 ± 8.28 nm/s; n=10),
722 and shrinkage (-1313.42 ± 671.54 nm/s; n=5), as determined by single-filament tracking from
723 TIRF microscopy. Bipolar growth and shrinkage were measured from single and dual color
724 time-lapse imaging series using Alexa488-CorM or Alexa488-CorM with low levels of Cy5-
725 CorM, while unipolar growth was extracted from dual color time-lapse imaging series only.
726

727 **Figure 6: Control of CorMR filaments by the Min system**

728 (**A**) *in silico* pulldown to identify interactions of CorM (bait) against the whole *Anabaena*
729 proteome (5326 open reading frames included in the analysis). Accuracy of the predicted
730 interaction is given as interface predicted template modelling (ipTM) score as described by
731 AlphaFold2[75]. ipTM scores for CorM, CorR and MinC are highlighted in the plot. (**B**) Scatter
732 plots of MinC sequence lengths (in aa) from all bacteria, cyanobacteria and *Nostocales*
733 cyanobacteria. (**C**) (top) AlphaFold3 prediction of an *Anabaena* MinC dimer. (bottom) A zoom-
734 in into a well-conserved pocket of CorM predicted to bind to the C-terminal α-helix of CorR
735 (blue) and the N-terminal α-helix of MinC (orange), suggesting a competition of CorR and MinC

736 for binding to CorM. Conservation is based on a multiple sequence alignment from all identified
737 cyanobacterial chromosomal CorMs (green clade). Coloring by sequence conservation is
738 based on the entropy-based measure AL2CO from ChimeraX[76] using the default coloring
739 scheme (cyan: poor conservation; white: intermediate conservation; red: highly conserved;
740 grey: no conservation). (**D**) *in vivo* time lapse microscopy of *Anabaena* cells expressing mNG-
741 MinC from a synthetic *ntcA* promoter integrated into the neutral *thrS2* site on the *Anabaena*
742 chromosome. Orange arrows indicate the positions of mNG-MinC fluorescence maxima in the
743 uppermost cell over time, highlighting its pole to pole oscillatory behavior throughout the time-
744 lapse analysis. Grey bar spanning the cell filament indicates region used to generate the
745 kymograph show in (E). (**F**) Representative Coomassie-stained SDS-PAGE gel from a high-
746 speed ultracentrifugation-based pelleting assay of 5 μM CorM with or without indicated MinC
747 concentrations in the presence of 2.5 mM ATP (i.e., under polymerizing conditions). 40 % of
748 the total pellet [P] and 11.1 % of the total supernatant [S] samples were separated on the gel.
749 CorM runs at around 45 kDa while MinC runs at ~55 kDa. The respective quantifications are
750 shown in Fig. S8G. (**G**) Representative Coomassie-stained SDS-PAGE gel from a high-speed
751 ultracentrifugation-based pelleting assay of 5 μM CorM with or without 5 μM MinC WT,
752 $MinC^{S50A+L55D}$, $^{\Delta 46-67}$MinC or a synthesized peptide mimicking MinC's N-terminal α-helix in the
753 presence of 2.5 mM ATP (i.e., under polymerizing conditions). 40 % of the total pellet [P] and
754 11.1 % of the total supernatant [S] samples were separated on the gel. The respective
755 quantifications are shown in Fig. S10A. (**H**) Snapshots from TIRF microscopy time lapse series
756 extracted from Supplementary Movies 8-11 of pre-formed CorMR filaments (0.75 μM
757 Alexa488-CorM, 0.25 μM CorM and 0.25 μM CorR) on SLBs supplemented with 1 μM MinC
758 WT, $MinC^{S50A+L55D}$, $^{\Delta 46-67}$MinC or buffer. Only MinC WT can depolymerize CorMR filaments on
759 the SLBs. We note that CorMR filaments re-assemble several minutes after addition of MinC
760 WT, indicating that CorM depolymerization by MinC is a transient effect. (**I**) Normalized
761 fluorescence intensity over time from the time lapse series shown in (H), with the initial value
762 set arbitrarily to 1. A decrease in fluorescence signal is observed only upon addition of MinC
763 WT, while both MinC mutants and the buffer control samples cause an increase in fluorescence

764 signal, likely due to mixing after addition, which replenishes the local concentration of CorM
765 monomers near the membrane.
766
767 **Figure 7: A quadruple evolutionary event regulated cell shape in *Anabaena***
768 (**A**) Cyanobacterial phylogenetic species tree with annotations indicating the presence of a
769 chromosomal CorMR system, an amphipathic helix (AH) in CorR homologs, an N-terminal
770 intrinsically disordered region (IDR) in CorM homologs, and a long MinC protein (>300 aa).
771 Monophyletic families were collapsed into single branches. Presence of the respective feature
772 within a family is assumed if at least 50 % of the species within the clade display the feature.
773 The complete tree is available in the Supplementary Figure 5 and Source Data, and detailed
774 information is provided in Supplementary File 1 and 3. (**B**) Proposed model for the regulation
775 of the chromosomal CorMR system in *Anabaena*. CorM assembles into cortical-like filaments
776 oriented transverse to the cell's long axis. These filaments are dynamically unstable and are
777 recruited to the cytoplasmic membrane by CorR, which has acquired membrane-binding
778 affinity through its N-terminal AH. CorM polymers are excluded from the cell poles and division
779 sites due to the regulatory actions of MinC, which localizes to these regions and actively
780 depolymerizes CorM filaments. (**C**) A model for the evolutionary diversification and cytoskeletal
781 innovation of an existing plasmid segregation system (ParMR), which was functionally
782 repurposed and evolved into CorMR, thereby contributing to the emergence of complex
783 multicellular (cyano)bacterial species.
784
785 **Supplementary figure legends:**
786 **Figure S1: Properties of the chromosomal ParMR**
787 (**A**) AlphaFold3-predicted structure of chromosomal ParM (chrParM) from *Anabaena* (pTM
788 score: 0.83) and the resolved X-ray structure of plasmid-encoded ParM from *E. coli* (PDB ID:
789 4A62). (**B**) AlphaFold3-predicted structure of a chromosomal ParR (chrParR) dimer from
790 *Anabaena* (pTM score: 0.34; ipTM score: 0.34) and the resolved X-ray structure of the plasmid-
791 encoded ParR dimer from *E. coli* (PDB ID: 2JD3). For A and B, predicted aligned error (PAE)

792 maps and plDDT score-colored structure predictions for AlphaFold3 predictions are also
793 shown. (**C**) Mean amino acid residues ± SD within the N-terminal IDR from ParM homologs
794 from the green (42.05 ± 11.03), yellow (9.66 ± 11.32) and pink (0.71 ± 2.149) clades of
795 cyanobacterial ParM's showing that only the green clade has any substantial N-terminal IDR.
796 (**D**) Representative growth curve analysis of *Anabaena* WT and Δ*parMR* revealing that the
797 mutant lacking ParMR has a slight growth defect. OD_{750} values were recorded every day or
798 every other day for a total of 11 days. Afterwards, cultures became too sticky to properly
799 measure the OD_{750} value. Error bars represent the mean ± SD of three technical replicates.
800 The experiment was performed twice with similar results. (**E**) Scanning electron microscopy
801 images of (left) *Anabaena* WT and Δ*parMR* revealing cell division defects in 30 % of actively
802 dividing Δ*parMR* cells (6 of 20 cells). These cells displayed irregular or incomplete septa, being
803 partially constricted but not fully separated, a phenotype not observed in the WT (16 cells). Left
804 Δ*parMR* image shows defects in proper constrictions, which are not observed in another
805 subset of Δ*parMR* cells as indicated on the right Δ*parMR* image. (**F**) Complementation
806 attempts of the Δ*parMR* phenotype. DIA micrograph of Δ*parMR* carrying a replicative plasmid
807 expressing *parM-parR* from a medium level, unregulated synthetic promoter (P_{ntcA}) derived
808 from the promoter of the global regulator of nitrogen homeostasis NtcA from *Anabaena*[77]. For
809 comparison Δ*parMR* is shown. The swollen phenotype of Δ*parMR* is moderated in the
810 complementation strain but expression of *parM-parR* from P_{ntcA} is not sufficient to provide the
811 same cellular levels of ParMR as the native promoter can. However, attempts to clone such
812 construct failed because *E. coli* can employ the P_{parMR} promoter, and we found that excess
813 levels of ParMR are toxic for *E. coli*. (**G**) Micrographs of *E. coli* C41 (DE3) co-expressing mNG-
814 ParM from P_{T7} and ParR-mScarlet-I from P_{BAD} grown over night in TB medium supplemented
815 with 0.02 % L-Ara and 0.25 mM IPTG at 37 °C. Cells containing ParR-mScarlet-I signal are
816 strikingly malformed, forming huge balloon-like structures. These cells lack any discernible
817 mNG-ParM signal, indicating that they cannot tolerate both proteins together for extended
818 periods. Micrograph with enhanced contrast reveals red fluorescent cell debris, likely
819 originating from burst cells expressing ParR-mScarlet-I. mNG-ParM localizes as filamentous

820 bundles in cells with WT-like morphology that lacked ParR-mScarlet-I signal, suggesting that
821 specifically ParR is responsible for the aberrant cell phenotype.
822
823 **Fig. S2: ParM's N-terminal IDR is not involved in cellular ParM localization or dynamics**
824 (**A**) Scatter plots showing the mean cell property values ± SD for cell width (WT: 4.8 ± 0.96
825 µm; Δ*parMR*: 4.53 ± 0.47 µm; mNG-ParM: 3.73 ± 0.65 µm; mNG-$^{\Delta 1\text{-}40}$ParM: 3.42 ± 0.49 µm),
826 cell length (WT: 2.89 ± 0.35 µm; Δ*parMR*: 3.88 ± 0.56 µm; mNG-ParM: 4.91 ± 0.56 µm; mNG-
827 $^{\Delta 1\text{-}40}$ParM: 4.06 ± 0.29 µm) and cell aspect ratio (WT: 0.62 ± 0.13; Δ*parMR*: 0.86 ± 0.09; mNG-
828 ParM: 0.76 ± 0.09; mNG-$^{\Delta 1\text{-}40}$ParM: 0.84 ± 0.09) of *Anabaena* WT, Δ*parMR*, mNG-ParM or
829 mNG-$^{\Delta 1\text{-}40}$ParM expressing cells. WT: n=222 cells; Δ*parMR*: n=259 cells; mNG-ParM: n=67
830 cells; mNG-$^{\Delta 1\text{-}40}$ParM: n=144 cells. Values for WT and Δ*parMR* are the same as in Fig. 1F-H.
831 (**B**) mNG-$^{\Delta 1\text{-}40}$ParM and merged mNG-$^{\Delta 1\text{-}40}$ParM and chlA autofluorescence micrographs of
832 *Anabaena* cells expressing mNG-$^{\Delta 1\text{-}40}$ParM as the sole copy obtained with a Nikon SoRa
833 spinning disk confocal microscope. (**C**) Time series from Supplementary Movie 3 displaying
834 TIRF micrographs of individual mNG-$^{\Delta 1\text{-}40}$ParM filaments over a period of 230 seconds. White
835 triangles mark the initial position of a single mNG-$^{\Delta 1\text{-}40}$ParM filament and red triangles mark the
836 furthest observed position of this filament during the time series. Blue triangles mark the initial
837 position of another single mNG-$^{\Delta 1\text{-}40}$ParM filament, yellow triangles mark the furthest observed
838 position of this filament during the time series and purple triangles indicate the position this
839 filament retracted to upon a dynamically instable shrinkage event. (**D**) Scatter plot showing the
840 mean ± SD of the growth velocities of mNG-ParM (18.96 ± 3.61 nm/s; n=80) and mNG-$^{\Delta 1\text{-}}$
841 ^{40}ParM (35.75 ± 8.19 nm/s; n=58) filaments, revealing the N-terminal IDR is responsible to limit
842 the growth kinetics *in vivo*. (**E**) ParR-mNG, DIA and merged ParR-mNG and chlA
843 autofluorescence micrographs of *Anabaena* expressing ParR-mNG as the sole copy. This
844 strain's cellular morphology is markedly altered, resembling the Δ*parMR* strain. This suggests
845 that the ParR-mNG fusion is not fully functional, likely because ParR's C-terminal peptide is
846 essential for interaction with ParM and is sterically hindered by the C-terminal mNG fusion.
847 Note that membrane localization of proteins in *Anabaena* looks mostly diffuse at the periphery

848 as is the case for ParR-mNG. For comparison, *Anabaena* cells expressing soluble mNG are
849 shown on the right side. Micrographs were obtained by a standard Nikon TI2 epi-fluorescence
850 microscope.
851
852 **Fig. S3: Biochemical properties of CorM reveal functional divergence from EcParM and**
853 **regulation by the N-terminal IDR**
854 (**A**) NTPase activity assay using the Malachite Green Phosphate Assay Kit (Sigma Aldrich)
855 shows that CorM readily hydrolyzes ATP but, unlike the EcParM, is not able to meaningfully
856 hydrolyze GTP. NTPase activity is quantified by the degree of phosphate release during the
857 conversion of NTP to NDP during NTPase activity. Error bars represent the mean ± SD of two
858 independent replicates (n=2). (**B**) Representative Coomassie-stained SDS-PAGE gel from a
859 high-speed ultracentrifugation-based pelleting assay comparing CorM with EcParM (both 5
860 μM) in the presence of buffer (ctrl.), ATP, ADP, GTP and a non-hydrolyzable ATP analog
861 (AMP-PNP). Nucleotides were provided at 2.5 mM each. 40 % of the total pellet [P] and 11.1
862 % of the total supernatant [S] samples were separated on the gel (**C, D**) Quantification of the
863 pelleting efficiency as displayed in (B), confirming that CorM only polymerizes in the presence
864 of ATP but not with GTP or AMP-PNP. Error bars represent the mean ± SD of three
865 independent replicates (n=3). (**E**) ATPase activity assay showing that CorM ATPase activity is
866 a concentration dependent process that seemingly begins to plateau at higher concentrations.
867 Error bars represent the mean ± SD of three independent replicates (n=3). (**F**) The degree of
868 CorM polymerization is not a concentration-dependent process and is not altered upon high-
869 levels of ParM (n=1). (**G**) ATPase activity assay comparing CorM with a mutant lacking the first
870 40 aa ($^{\Delta 1\text{-}40}$CorM) reveals that the N-terminal IDR limits CorM's ATPase activity. Error bars
871 represent the mean ± SD of two independent replicates with 3 technical replicates each. (**H**)
872 AlphaFold3-predicted interaction between CorM and a CorR dimer, together with the
873 corresponding PAE map, showing interaction of CorR's C-terminal α-helix H5b with CorM, as
874 well as a plDDT score-colored CorM-CorR complex (pTM score: 0.59; ipTM score: 0.51). (**I**)
875 Representative Coomassie-stained SDS-PAGE gel from a high-speed ultracentrifugation-

876 based pelleting assay comparing ParM and ParR, alone or in combination (5 µM each),
877 incubated with 2.5 mM ATP or without nucleotide (ctrl.) (n=2). 34 % of the total pellet [P] and
878 9.7 % of the total supernatant [S] samples were separated on the gel (**J**) Quantification of the
879 pelleting efficiency from (C), showing pellet and supernatant values for ParM (left graph) and
880 ParR (right graph) individually. CorR is recruited to the pellet through polymerized CorM (ATP-
881 containing sample). Data represent the mean ± SD from two independent experiments (n=2)
882 (**K**) B2H assays testing for the interaction of chrParM with chrParR from Anabaena fused to
883 either the T25 or T18 subunit, including a ParR variant lacking the predicted C-terminal α-helix,
884 which is known to facilitate the interaction of plasmid-encoded ParR with ParM in *E. coli*.
885 chrParR lacking amino acids 150-162 is no longer able to interact with ParM. Negative control:
886 ParM-T18 with empty pKNT25 plasmid. Positive control: Zip/Zip control. Error bars represent
887 the mean ± SD of three independent replicates (n=3).
888
889 **Fig. S4: CorR binds to lipid membranes**
890 (**A**) Quantification analysis of the CorM with CorR pelleting assay from Fig. 3C showing the
891 values for CorM and CorR separately. P indicates values for pellet samples and S indicates
892 values for supernatant samples. Error bars represent the mean ± SD from at least three
893 independent replicates. (**B**) Representative Coomassie-stained SDS-PAGE gel from a
894 pelleting assay with indicated protein combinations with or without MLVs (proteins are provided
895 as 5 µM each). 30 % of the total pellet [P] and 12.5 % of the total supernatant [S] samples
896 were separated on the gel. (**C**) Quantifications from pelleting assay shown in (B), showing
897 values for CorM and CorR separately. Error bars represent the mean ± SD from three
898 independent replicates (n=3). (**D**) Amino acid sequence logo (using WebLogo[78]) from the
899 multiple sequence alignment shown in Fig. S5, showing only the first 20 aa of CorR's N-
900 terminus. To enhance readability, CorR sequences from *Oscillatoriales* and *Nostocales* are
901 shown independently, which also highlights that the N-terminal CorR region is strongly
902 conserved among *Nostocales* species and less so among *Oscillatoriales* species.
903

904 **Figure S5: Conservation of CorR's amphipathic helix**

905 Cyanobacterial phylogenetic species tree with multiple sequence alignment of CorR homologs
906 containing a N-terminal AH. Since AHs were only found among chromosomal CorMR
907 homologs in *Nostocales* and *Oscillatoriales*, only sequences from these species are shown.
908 The N-terminal region comprising the AH (roughly 10 aa) is highly conserved among
909 *Nostocales* species and less among *Oscillatoriales* species.

910

911 **Fig. S6: Cryo-EM image processing strategy applied to obtain structure of CorM filament**
912 **(CorMR filaments (6.1), $^{\Delta 1\text{-}40}$CorM (6.2), and CorM (6.3)) and the final cryo-EM maps (6.4)**

913 Schematics of the image processing strategy used for determining all the three obtained CorM
914 filament structures using cryoSPARC v4.4. Representative micrographs, 2D class averages,
915 3D class averages, and final electron microscopy density maps are shown. For helical
916 refinement jobs, the initial estimates of helical rise and helical twist were obtained using online
917 helical indexing tool (HI3D- Helical Indexing using cylindrical projection of a 3D map[79]). These
918 values are marked with * under each helical refinement job. Two side views of local resolution
919 filtered EM maps and Fourier Shell Correlation (FSC) curves are displayed. The surface
920 representation of the final cryo-EM maps of CorM, $^{\Delta 1\text{-}40}$CorM, and CorMR and their estimated
921 resolutions (using FSC 0.143 criteria) are shown in 6.4.

922

923 **Fig. S7: The N-terminal IDR prevents filament bundling and increases protein dynamics**

924 (**A**) Representative FRAP snapshots from TIRF microscopy time series (Supplementary
925 Movies 4-5) of pre-formed CorMR or $^{\Delta 1\text{-}40}$CorMR filaments (0.75 μM unlabeled CorM WT or $^{\Delta 1\text{-}}$
926 ^{40}CorM, 0.25 μM Alexa488-CorM or Alexa488-$^{\Delta 1\text{-}40}$CorM and 0.125 μM unlabeled CorR) on
927 SLBs subjected to photobleaching. (**B**) Dependency of the half-recovery time on CorR
928 concentration. Plot showing the half-recovery time ($T_{1/2}$) in seconds as a function of CorR
929 concentration (0.125 μM, 0.25 μM, and 0.75 μM). Increasing concentrations of CorR lead to a
930 dose-dependent decrease in $T_{1/2}$, suggesting higher CorM dynamics with higher CorR levels.
931 Error bars represent the mean ± SD from individual measurements: 0.125 μM: 10.64 ± 0.87

932 nm/s (n=9); 0.25 μM: 6.97 ± 0.24 nm/s (n=6); 0.75 μM: 4.94 ± 0.14 nm/s (n=5). Half-recovery
933 times comparing CorM WT and $^{\Delta 1\text{-}40}$CorM in the presence of 0.125 μM CorR, showing that the
934 N-terminal IDR in CorM modulates dynamics and reaction kinetics. Error bars represent the
935 mean ± SD from individual measurements: CorM values are the same as in (B); $^{\Delta 1\text{-}40}$CorM:
936 24.65 ± 1.22 nm/s (n=7). (**D**) Representative recovery curves from FRAP experiments
937 comparing CorM WT and $^{\Delta 1\text{-}40}$CorM in the presence of 0.125 μM CorR. (**E**) Representative
938 snapshots of $^{\Delta 1\text{-}40}$CorM (protein concentrations same as in A) filaments in the course of an
939 imaging session. Like CorM WT, $^{\Delta 1\text{-}40}$CorM initially forms individual filaments. These filaments
940 then form thick bundles but eventually assemble into a well-defined network of filaments, which
941 appears much more ordered compared to CorM WT (see Fig. 5B for comparison).
942
943 **Fig. S8: Properties of the *Anabaena* Min system and it's modulating function on CorM**
944 (A) (top) AlphaFold3-predicted interaction between CorM and MinC, together with the
945 corresponding PAE map, showing interaction of MinC's N-terminal α-helix with CorM, as well
946 as a plDDT score-colored CorM-MinC complex (pTM score: 0.51; ipTM score: 0.76). (bottom)
947 AlphaFold3-predicted MinC dimer (pTM score: 0.46; ipTM score: 0.47), including the
948 corresponding PAE map and a plDDT score-colored dimer. (**B-D**) B2H assays testing for the
949 interaction of CorMR with (**B**) MinC, (**C**) Cdv3 or (**D**) MinD and MinE fused to either the T25 or
950 T18 subunit. Both, CorM and CorR interact with MinC but only CorR interacts with Cdv3.
951 Neither CorM nor CorR interacts with MinD or MinE. Negative control: (B, D) CorM-T25 with
952 empty pUT18C plasmid or (C) CorM-T18 with empty pKNT25 plasmid. Positive control: Zip/Zip
953 control Error bars represent the mean ± SD of three independent replicates (n=3). (**E**) B2H
954 assays testing for the interaction of MinC with MinD, MinE and Cdv3 fused to either the T25 or
955 T18 subunit. Results show that MinC interacts with all three proteins. Negative control: MinC-
956 T25 with empty pUT18C plasmid. Positive control: Zip/Zip control. Error bars represent the
957 mean ± SD of three independent replicates (n=3).
958

959 **Fig. S9: In *Nostocales* cyanobacteria MinC exhibits an extended N-terminal domain**
960 MinC phylogenetic tree, including cyanobacteria and other bacterial species. Blue-shaded
961 cubes next to the tree indicates MinC sequence lengths. Note that specifically *Nostocales*
962 cyanobacteria contain long MinC sequences (>300 aa), which is represented by an N-terminal
963 IDR with an α-helix in between. On the right, a multiple sequence alignment of all listed MinCs
964 is shown with two different conservation patterns. Orange shades indicate conservation
965 exclusively among the N-terminal IDR of *Nostocales* MinCs whereas grey shades indicate
966 conservation exclusively among the globular domain of MinC. Black dots indicate Ultrafast
967 Bootstrap supports (UFB) >= 85. The scale bar represents the average number of substitutions
968 per site.
969
970 **Fig. S10: MinC's N-terminal α-helix mediates CorM depolymerization**
971 (**A**) AlphaFold3-predicted structures of (top) plasmid-encoded ParM (#BAB78165.1; All7081)
972 from the large low copy number Alpha plasmid from *Anabaena* or (bottom) plasmid-encoded
973 EcParM (WP_000959884.1) from the R1 plasmid. Conservation is based on multiple sequence
974 alignments from all identified cyanobacterial plasmid-encoded ParMs or all identified other
975 bacterial plasmid-encoded ParMs. Coloring by sequence conservation is based on the
976 entropy-based measure AL2CO from ChimeraX[76] using the default coloring scheme (cyan:
977 poor conservation; white: intermediate conservation; red: highly conserved). (**B**) mNG-MinC
978 fluorescence, chlA autofluorescence and merged micrographs of *Anabaena* expressing mNG-
979 MinC from P_{ntcA} integrated into the neutral chromosomal *thrS2* sites. Fluorescence intensity
980 profiles show high levels of MinC at the cell poles and midcell in diving cells and only at the
981 cell poles in vegetative cells. (**C**) Quantifications from pelleting assay shown in Fig. 6F showing
982 values for CorM and MinC separately. Different MinC protein concentrations are indicated
983 below. Error bars represent the mean ± SD of two independent replicates (n=2). (**D**) Sequence
984 logo showing the conservation of aa residues within the N-terminal α-helix of *Nostocales*
985 cyanobacteria. A multiple sequence alignment of all tested MinC sequences from
986 cyanobacteria and other bacteria is shown in Fig. S9. (**E**) Quantifications from pelleting assay

shown in Fig. 6G showing values for CorM. Both MinC helix mutants, $MinC^{S50A+L55D}$ and $^{\Delta 46-67}$MinC lost the ability to depolymerize CorM filaments. A synthesized peptide mimicking MinC's N-terminal α-helix had no influence on CorM polymerization, indicating that other aspects of the interaction of CorM with MinC are essential for active depolymerization. Error bars represent the mean ± SD of three independent replicates (n=3). (**F**) CorM ATPase activity assay with or without indicated MinC concentrations resolved over time, showing that MinC acts on CorM by decreasing its enzymatic activity. Data represents the mean values for each data point from three independent replicates (n=3). (**G**) B2H assays testing for the interaction of CorM with MinC helix mutants ($MinC^{S50A+L55D}$ and $^{\Delta 46-67}$MinC) fused to either the T25 or T18 subunit. Results show that CorM interaction with MinC is lost in both MinC helix mutants. Negative control: CorM-T25 with empty pUT18C plasmid. Positive control: Zip/Zip control. Error bars represent the mean ± SD of three independent replicates (n=3).

Acknowledgements:

We thank all members of the Martin Loose lab at ISTA for helpful discussions and Marko Kojic for critical reading of the manuscript. This research was supported by the Scientific Service Units (SSU) of ISTA through resources provided by the Imaging & Optics Facility (IOF), the Scientific Computing (SciComp) and the Electron Microscopy Facility (EMF), as well as the Lab Support Facility (LSF). This project has received funding from the European Union's Horizon 2020 research and innovation program under the Marie Skłodowska-Curie Grant Agreement No.101034413 awarded to BLS as well as an ERC grant (ActinID, 101076260) from the European Union awarded to FKMS. Views and opinions expressed are however those of the author(s) only and do not necessarily reflect those of the European Union or the European Research Council. Neither the European Union nor the granting authority can be held responsible for them.

We are grateful for Antonia Herrero (Sevilla University) for sharing her extensive BACTH plasmid library and other plasmids as well as cyanobacterial strains. Likewise, we would like

to thank Tal Dagan and Fabian Nies (both Kiel University) for sharing cyanobacterial strains and plasmids and for valuable discussions.

We would further like to express our gratitude to Nicolas Sapay and Alexis Michon for providing the Amphipaseek code, which enabled us to perform our large-scale amphipathic helix screen of cyanobacterial CorR proteins. Finally, we also want to thank Jesse Hansen for advice in cryo-EM data processing.

Author contributions:

Conceptualization: BLS and ML; Experimental investigation: BLS, MGJ, DM, RH, and DMH; Data analysis: BLS, MGJ, DM, RH, DMH, FKMS and ML; Visualization: BLS, MGJ, DM, RH, FKMS and ML; Writing (original draft): BLS and ML with contributions from all co-authors.

Competing interests:

The authors declare no competing interests.

Data availability:

The electron microscopy density maps of the different CorM filament structures have been deposited in the Electron Microscopy Data Bank under accession codes: **EMD-54060** (CorM in the presence of CorR), **EMD-54061** (CorM) and **EMD-54062** ($^{\Delta 1\text{-}40}$CorM). The model of the CorM filament refined into EMD-54060 has been deposited in the Protein Data Bank under accession code: **PDB 9RMI** (Extended PDB ID pdb_00009RMI).

Source Data for phylogenetic analysis will be available in a Mendeley repository under accession code 10.17632/d6hmm7bjnt.1 upon publication, but is temporarily accessible from: https://data.mendeley.com/preview/d6hmm7bjnt?a=9155e04d-88b1-4719-8ec6-0a300aa479f6

Supplementary Movies will be available from an ISTA repository but are temporarily available from the authors upon request. All other data are either directly enclosed to this manuscript or available from the authors upon reasonable request.

1042 **Material and methods:**

1043 ***Bacterial strains and growth conditions***

1044 *Escherichia coli* strain DH5α was used for routine cloning procedures and chemically
1045 competent *E. coli* were transformed with plasmid DNA by the standard heat shock procedure.
1046 BL21 (DE3) (NEB, USA) or C41 (DE3) (Merck, USA) were used for heterologous recombinant
1047 protein expression. Strain BTH101 was used for bacterial adenylate cyclase two-hybrid system
1048 (BACTH) analysis. All *E. coli* strains listed in Supplementary Table 1 were grown in standard
1049 LB or TB medium containing the appropriate antibiotics at standard concentrations. *Anabaena*
1050 was a gift from Tal Dagan (Kiel University, Germany) and cells were routinely grown
1051 photoautotrophically in BG11 medium at constant illumination with an intensity of 1200 Lux
1052 (using a Osram T8 L 15W/840 LUMILUX Cool White G13 light bulb) or at RT with ambient light
1053 exposure for extended culturing. When appropriate, liquid growth medium or agar plates
1054 (containing 1.5 % agarose) were supplemented with 50 µg/ml neomycin or 5% sucrose.

1055

1056 ***Plasmid construction***

1057 All plasmids generated in this study (see Supplementary Table 1) were constructed using an
1058 in-house Gibson assembly mix or the Q5® Site-Directed Mutagenesis Kit (NEB, USA). Primers
1059 employed for plasmid construction are listed in Supplementary Table 2. In each case, plasmid
1060 sequence integrity was verified by Sanger sequencing by Microsynth Austria GmbH (Austria).
1061 In addition, we are grateful for Antonia Herrero, Fabian Nies and Tal Dagan for a wealth of
1062 plasmids, particularly for the BACTH plasmid library from Antonia Herrero.

1063 pBAD33.1-Km: The nptII cassette was amplified from pRL25C using primers
1064 (oBS218+oBS219) and integrated into PCR-amplified pBAD33.1 (using primers
1065 oBS216+oBS217). pBS1: *corM* was amplified from *Anabaena* genomic DNA using primers
1066 oBS8+oBS9 and then integrated into HindIII+BamHI-digested pKNT25 by Gibson assembly.
1067 pBS2: *corM* was amplified from *Anabaena* genomic DNA using primers oBS10+oBS11 and
1068 then integrated into BamHI+EcoRI-digested pKT25 by Gibson assembly. pBS3: *corM* was
1069 amplified from *Anabaena* genomic DNA using primers oBS8+oBS9 and then integrated into

1070 HindIII+BamHI-digested pUT18 by Gibson assembly. pBS4: *corM* was amplified from
1071 *Anabaena* genomic DNA using primers oBS12+oBS13 and then integrated into BamHI+EcoRI-
1072 digested pUT18C by Gibson assembly. pBS9: corR was amplified from *Anabaena* genomic
1073 DNA using primers oBS18+oBS19 and then integrated into HindIII+BamHI-digested pKNT25
1074 by Gibson assembly. pBS10: *corR* was amplified from *Anabaena* genomic DNA using primers
1075 oBS20+oBS21 and then integrated into BamHI+EcoRI-digested pKT25 by Gibson assembly.
1076 pBS11: *corR* was amplified from *Anabaena* genomic DNA using primers oBS18+oBS19 and
1077 then integrated into HindIII+BamHI-digested pUT18 by Gibson assembly. pBS12: *corR* was
1078 amplified from *Anabaena* genomic DNA using primers oBS22+oBS23 and then integrated into
1079 BamHI+EcoRI-digested pUT18C by Gibson assembly. pBS41: *corR* was amplified from
1080 *Anabaena* genomic DNA using primers oBS69+oBS70 and integrated into PCR-amplified
1081 pTB146 (using primers oBS59+oBS60) by Gibson assembly. pBS47: *parR* from the *E. coli*
1082 NR1 plasmid was amplified from a gBlock (Twist Biosciences, USA) using primers
1083 oBS81+oBS82 and ligated into PCR-amplified pTB146 (using primers oBS59+oBS60) by
1084 Gibson assembly. pBS71: *corM* was amplified from *Anabaena* genomic DNA using primers
1085 oBS62+oBS126 and ligated into PCR-amplified pTB146 (using primers oBS59+oBS60) by
1086 Gibson assembly. pBS75: *parM* from the *E. coli* NR1 plasmid was amplified from a gBlock
1087 (Twist Biosciences, USA) using primers oBS80+oBS130 and ligated into PCR-amplified
1088 pTB146 (using primers oBS59+oBS60) by Gibson assembly. Plasmid pBS80 was constructed
1089 using Gibson assembly to ligate three PCR-amplified fragments. The vector was amplified from
1090 plasmid pTB146 using primers oBS59+oBS150, mNeonGreen (mNG) was amplified from a
1091 gBlock (Twist Biosciences, USA) using primers oBS151+oBS119 and *corM* was amplified from
1092 *Anabaena* genomic DNA using primers oBS120+oBS62. pBS103 was generated by annealing
1093 of primers oBS199+oBS200 and ligating the annealed primers into AarI-digested pCpf1b using
1094 T4 ligase (NEB, USA). pBS105 was generated by annealing of primers oBS203+oBS204 and
1095 ligating the annealed primers into AarI-digested pCpf1b using T4 ligase (NEB, USA). pBS108
1096 was constructed by Gibson assembly, ligating two PCR-amplified fragments - amplified from
1097 *Anabaena* genomic DNA using primers oBS205+oBS206 and oBS207+oBS208 - into BamHI-

1098 digested pBS105. Plasmid pBS135 was constructed using Gibson assembly to ligate three
1099 PCR-amplified fragments. The vector was amplified from plasmid pTB146 using primers
1100 oBS59+oBS150, *parM* from the *E. coli* NR1 plasmid was amplified from a gBlock (Twist
1101 Biosciences, USA) using primers oBS284+oBS285 and mNG was amplified from a gBlock
1102 (Twist Biosciences, USA) using primers oBS154+oBS155. pBS136 was generated by
1103 annealing of primers oBS286+oBS287 and ligating the annealed primers into AarI-digested
1104 pCpf1b using T4 ligase (NEB, USA). pBS138 was constructed by Gibson assembly, ligating
1105 two PCR-amplified fragments - amplified from *Anabaena* genomic DNA using primers
1106 oBS290+oBS291 and oBS292+oBS293 - into BamHI-digested pBS136. pBS154 was
1107 generated by annealing of primers oBS401+oBS402 and ligating the annealed primers into
1108 AarI-digested pCpf1b using T4 ligase (NEB, USA). pBS159 was generated by Gibson
1109 assembly-based ligation of two PCR products into PCR-amplified (using primers
1110 oBS143+oBS144); one amplifying *corR* from *Anabaena* genomic DNA using primers
1111 oBS145+oBS147 and the 2nd amplifying *mScarlet-I* from a gBlock (Twist Biosciences) using
1112 primers oBS148+oBS149. pBS166 was generated by Gibson assembly-based ligation of three
1113 PCR products into BamHI-digested pBS138; one amplifying a synthetically optimized *ntcA*
1114 promoter (P_{ntcA})[80] using primers oBS294+oBS297 and pCSL135[81] as a template, the 2nd one
1115 amplifying *corR* using primers oBS338+oBS345 and *Anabaena* genomic DNA as a template
1116 and the 3rd amplifying SCFP3 using primers oBS346+oBS347 and a gBlock (Twist
1117 Biosciences, USA) as a template. pBS184 was generated by Gibson assembly-based ligation
1118 of three PCR products into BamHI-digested pBS138, one amplifying P_{ND} using primers
1119 oBS294+oBS297 and pCSL135 as a template, the 2nd one amplifying *corR* using primers
1120 oBS338+oBS376 and *Anabaena* genomic DNA as a template and the 3rd amplifying mNG
1121 using primers oBS377+oBS296 and a gBlock (Twist Biosciences, USA) as a template. pBS190
1122 was generated by annealing of primers oBS385+oBS386 and ligating the annealed primers
1123 into AarI-digested pCpf1b using T4 ligase (NEB, USA). pBS191 was generated by Gibson
1124 assembly-based ligation of three PCR products into BamHI-digested pBS190. The first product
1125 amplified 1000 bp upstream of *corM* using primers oBS205+oBS117 and *Anabaena* genomic

1126 DNA as a template. The 2nd product was amplified sequentially by first amplifying mNG using
1127 primers oBS118+oBS119 and a gBock as a template and then using this product as a new
1128 template for the following PCR using primers oBS118+oBS378. The 3rd PCR amplified parts
1129 of the *corM* open reading frame (ORF) using primers oBS388+oBS389 and *Anabaena*
1130 genomic DNA as a template. pBS196 was generated by Gibson assembly-based ligation of
1131 three PCR products into BamHI-digested pBS154, one amplifying a ~1000 bp fragment that
1132 encompassed *corR* and parts of *corM* using primers oBS403+oBS404 and *Anabaena* genomic
1133 DNA as a template, the 2nd one amplifying mNG using primers oBS405+oBS406 and pBS184
1134 as a template and the 3rd amplifying 1000 bp downstream of *corR* using primers
1135 oBS407+oBS208 and *Anabaena* genomic DNA as a template. pBS201: *minD* was amplified
1136 from *Anabaena* genomic DNA using primers oBS415+oBS416 and then ligated into
1137 HindIII+BamHI-digested pKNT25. pBS202: *minD* was amplified from *Anabaena* genomic DNA
1138 using primers oBS417+oBS418 and then ligated into BamHI+EcoRI-digested pKT25. pBS203:
1139 *minD* was amplified from *Anabaena* genomic DNA using primers oBS415+oBS416 and then
1140 ligated into HindIII+BamHI-digested pUT18. pBS204: *minD* was amplified from *Anabaena*
1141 genomic DNA using primers oBS419+oBS420 and then ligated into BamHI+EcoRI-digested
1142 pUT18C. pBS205: *minE* was amplified from *Anabaena* genomic DNA using primers
1143 oBS421+oBS422 and then ligated into HindIII+BamHI-digested pKNT25. pBS206: *minE* was
1144 amplified from *Anabaena* genomic DNA using primers oBS423+oBS424 and then ligated into
1145 BamHI+EcoRI-digested pKT25. pBS208: *minD* was amplified from *Anabaena* genomic DNA
1146 using primers oBS425+oBS426 and then ligated into BamHI+EcoRI-digested pUT18C.
1147 pBS213: *cdv3* was amplified from *Anabaena* genomic DNA using primers oBS433+oBS434
1148 and then ligated into HindIII+BamHI-digested pKNT25. pBS214: *cdv3* was amplified from
1149 *Anabaena* genomic DNA using primers oBS435+oBS436 and then ligated into BamHI+EcoRI-
1150 digested pKT25. pBS231 was generated by site-directed mutagenesis using primers
1151 oBS60+oBS464 and pBS41 as a template. pBS233 generated by site-directed mutagenesis
1152 using primers oBS60+oBS475 and pBS71 as a template. pBS316: *minC* was amplified from
1153 *Anabaena* genomic DNA using primers oBS648+oBS649 and ligated into PCR-amplified

1154 pTB146 (using primers oBS59+oBS60) by Gibson assembly. pBS326 was generated by
1155 Gibson assembly-based ligation of three PCR products into BamHI-digested pBS138, one
1156 amplifying P_{ND} using primers oBS294+oBS229 and pCSL135 as a template, the 2nd one
1157 amplifying mNG using primers oBS118+oBS119 and a gBlock as a template and the 3rd
1158 amplifying *minC* using primers oBS508+oBS669 and *Anabaena* genomic DNA as a template.
1159 pBS338: $^{\Delta 150\text{-}162}$*corR* was amplified from *Anabaena* genomic DNA using primers
1160 oBS20+oBS700 and then ligated into BamHI+EcoRI-digested pKT25. pBS339: $^{\Delta 150\text{-}162}$*corR*
1161 was amplified from *Anabaena* genomic DNA using primers oBS22+oBS701 and then ligated
1162 into BamHI+EcoRI-digested pUT18C. pBS346 was generated by site-directed mutagenesis
1163 using primers oBS59+oBS711 and pBS41 as a template. pBS353 was generated by site-
1164 directed mutagenesis using primers oBS720+oBS721 and pBS316 as a template. pBS354
1165 was generated by site-directed mutagenesis using primers oBS722+oBS723 and pBS316 as
1166 a template. pBS386 was generated by site-directed mutagenesis using primers
1167 oBS720+oBS721 and pCSAV269 (a gift from Antonia Herrero, Sevilla University) as a
1168 template. pBS387 was generated by site-directed mutagenesis using primers
1169 oBS722+oBS723 and pCSAV269 as a template. pBS396 was generated by Gibson assembly-
1170 based ligation of two PCR products into BamHI-digested pBS103. The first product amplified
1171 1000 bp upstream of *corM* and *mNG* using primers oBS205+oBS119 and pBS191 as a
1172 template. The 2nd product amplified 882 bp downstream of codon 40 of *corM* using primers
1173 oBS651+oBS389 and pBS191.
1174
1175 ***Strain construction***
1176 Transformation into *Anabaena* WT or mutant strains was achieved using a triparental mating,
1177 essentially as described before in [47], but with the following modification: instead of *E. coli*
1178 HB101, we used *E. coli* DH5α. Over-night grown *E. coli* and *Anabaena* were mixed and plated
1179 onto nitrocellulose filters (0.45 µm pore size) placed on BG11 plates supplemented with 5%
1180 LB pre-mixed powder. Cells were incubated for 6 - 8 hours at 30 °C under low light and then
1181 transferred to BG11 plates containing 50 µg/ml neomycin (BG11+Nm) and exposed to full light.

1182 Colonies routinely appeared after 10 - 12 days. These were picked and re-streaked on
1183 BG11+Nm plates to isolate single colonies and eliminate residual *E. coli* for several rounds.
1184 For heterologous expression of fluorescently labeled proteins, newly emerging colonies were
1185 screened by fluorescence microscopy and propagated on BG11+Nm plates instead.
1186 Strain BS326 was generated by Cpf1-based heterologous insertion of the P_{ntcA}-*mNG-minC*
1187 construct into the *thrS2* open reading frame (encoding threonine-tRNA ligase; NCBI Ref. Seq.:
1188 WP_010998854.1), a chromosomal neutral site[20,74]. Double homologous recombination using
1189 ~1000 bp flanking regions cloned into plasmid pBS326 replaced the *thrS2* segment encoding
1190 residues Q188–F228 with P_{ntcA}-*mNG-minC*. Complete segregation was verified by colony PCR
1191 using construct-specific primers.
1192 For colony PCR, colonies were either picked with a pipette tip, briefly spotted onto a fresh
1193 BG11+Nm plate, and then resuspended directly in the PCR reaction mixture, or resuspended
1194 in 10 µl sterile PBS, of which 1 µl was used for each 10 µl PCR reaction.
1195 For the Δ*corMR* (strain BS108), plasmid pBS108 was conjugated into *Anabaena* WT. Arising
1196 colonies were re-streaked twice onto fresh BG11+Nm plates. Deletion of *corM-corR* was
1197 confirmed by colony PCR using site- and gene-specific primers, followed by Sanger
1198 sequencing of the encompassing regions.
1199 Strain BS191, expressing mNG-CorM as the sole copy of CorM, was generated by conjugating
1200 plasmid pBS191 into *Anabaena* WT. Resulting colonies were picked, re-streaked on
1201 BG11+Nm plates, screened for mNG-CorM fluorescence by microscopy, and verified by
1202 Sanger sequencing of a PCR-amplified fragment encompassing the P_{corMR}-*mNG-corM-corR*
1203 region from a single colony. Strain BS396 was obtained in the same manner as BS191, using
1204 plasmid pBS396 instead of pBS191. Sanger sequencing confirmed the presence of P_{corMR}-
1205 *mNG-*$^{\Delta 1–40}$*corM-corR.*
1206 In all cases, curing of pCpf1b was performed by sucrose counter-selection. For this, strains
1207 were grown in BG11 medium, sonicated in a VWR Ultrasonic Cleaner USC-TH for 10 min at
1208 maximum intensity, and then plated in 1:10 serial dilutions on BG11 plates supplemented with
1209 5% sucrose. Arising colonies were screened by streaking on BG11 and BG11+Nm plates;

1210 those that failed to grow on BG11+Nm (indicating loss of pCpf1) were selected for further
1211 experiments.
1212
1213 ***BACTH analysis***
1214 For protein-protein interaction analysis, the BACTH system (Euromedex, France) was
1215 employed. Genes were cloned into the expression vectors pKNT25, pKT25, pUT18, and
1216 pUT18C using GIBSON assembly, resulting in N- or C-terminal translational fusions to the T25
1217 or T18 subunit of the *E. coli* adenylate cyclase. *E. coli* BTH101 cells were co-transformed with
1218 about 5 ng of the respective plasmid combinations and then plated on LB agar containing 200
1219 µg/ml X-gal, 0.5 mM IPTG, 100 µg/ml ampicillin (Amp), and 50 µg/ml Kanamycin (Km). As a
1220 positive control, plasmids pKT25-zip and pUT18C-zip and as a negative control empty plasmid
1221 pUT18 and a pKNT25 plasmid containing a test gene were also co-transformed into BTH101
1222 cells. The plates were incubated at RT for 2-3 days. To then measure beta-galactosidase as a
1223 surrogate measure to quantify protein-protein interaction strengths, a modified protocol from
1224 Karimova et al.[82] was employed. For each combination, three independent colonies were
1225 picked and grown in 300 µl LB supplemented with 0.5 mM IPTG, Amp, and Km in a 2 ml 96-
1226 well deep well plate for 2-3 days at RT and 1000 rpm in an orbital microplate shaker.
1227 Afterwards, 50 µl of cells were diluted with 50 µl 2x M63 medium and OD_{595} values were
1228 recorded in a 96-well plate. Cells were then lysed by adding 10 µl of PopCulture® Reagent
1229 (Merck, USA) supplemented with 10µl/ml Lysonase™ Bioprocessing Reagent (Merck, USA).
1230 Lysis was conducted for at least 30 min at RT and rigorous shaking with 650 rpm in the 96-
1231 well plate on an orbital microplate shaker (We find that even hour-long lysis did not decrease
1232 experimental readout). Subsequently, 20 µl of lysate was added to 105 µl of PM2 assay
1233 medium supplemented with 100 mM β-mercaptoethanol in a new 96-well plate and incubated
1234 at RT with mild shaking for 20 min before the reaction was stopped by adding 50 µl of 1 M
1235 Na_2CO_3. Finally, OD_{405} values were recorded, and beta-galactosidase activity was calculated
1236 as described in the BACTH System Kit (Euromedex).
1237

1238 ***Microscopy***

1239 Experiments were performed using a Nikon Eclipse Ti2 microscope equipped with iLas2
1240 (GATACA) 360° / Ring / Azimuthal TIRF module, a TI2-N-ND-P Perfect Focus System and
1241 either a CFI Apochromat TIRF 60x oil immersion objective (NA 1.49, WD 0.13 mm) or a CFI
1242 Plan Apo Lambda D 100x oil immersion objective (NA 1.45, WD 0.13 mm).

1243 Fluorophores and fluorescent proteins were excited using the Omicron LightHUB Ultra laser
1244 system for TIRF imaging and Fluorescence Recovery After Photobleaching (FRAP), equipped
1245 with 405nm, 488nm, 561nm and 640nm lasers. Emitted fluorescence signals were filtered
1246 using a Nikon 525/50 ET bandpass and a 635 nm long pass filter for dual-color imaging. For
1247 the dual-color experiments, a Cairn TwinCam camera splitter equipped with a TwinCam Cube
1248 dichroic mirror for green/red,far-red was used in addition.

1249 For epifluorescence microscopy, LED-FITC-A Filter Cube EX 474/27, EM 525/45 and LED-
1250 Cy5-A Filter Cube EX 628/40, BA 692/40 filter cubes were used, and bright field images were
1251 obtained with a CoolLED pE300 White MB light source. The microscope was operated using
1252 the NIS elements AR (v.5.42.04) software and images were recorded using one or two Andor
1253 iXon Life 888 Back Illuminated EMCCD cameras.

1254 High-resolution spinning disk confocal microscopy was conducted using a Nikon Ti2 CSU W1-
1255 01 SoRa+NIR microscope, equipped with a Nipkow disk-based Super-resolution via optical
1256 Re-assignment (SoRa) module and a Nikon CFI Plan Apochromat 100× silicone immersion
1257 objective (NA 1.35, WD 0.3 mm). Excitation was provided by an Omicron LightHUB UltraN
1258 laser system with 405 nm, 488 nm, and 561 nm lasers, guided through a confocal quad-band
1259 dichroic mirror (405/488/561/640 nm). Emission signals were collected through a quad-band
1260 emission filter (440/521/607/700 nm) and imaged using a Teledyne Photometrics BSI scientific
1261 CMOS camera.

1262

1263 ***DAPI staining***

1264 For DAPI staining, cells grown on BG11 agar plates were re-suspended in PBS supplemented
1265 with 10 µg/ml DAPI (final), incubated for 1-2 min and then spotted and immobilized on BG11
1266 2% agar pads prior to imaging.

1267

1268 ***Time lapse microscopy of mNG-CorM in Anabaena cells***

1269 For time-resolved tracking of mNG-CorM filaments in *Anabaena* cells of strain BS191, cells
1270 were grown on BG11 plates, re-suspended in sterile BG11 and spotted on BG11 pads
1271 containing 1.5 % low melting agarose (TopVision Low Melting Point Agarose, Thermo Fisher
1272 Scientific) supplemented with 10 mM $NaHCO_3$ in a Grene Frame (65 µl; Thermo Fisher
1273 Scientific) to avoid evaporation. Cells were visualized in a Nikon Eclipse Ti2 microscope
1274 equipped with iLas2 system and mNG-CorM filaments were recorded in epifluorescence mode
1275 (50 ms exposure, 10 % blue LED light intensity). Cells were grown at RT and illuminated using
1276 a custom-made plant light equipped with three LEDs emitting blue (450 nm), red (655 nm), and
1277 far-red (725 nm) light. The light intensities at the sample position were 285.20 mW/m² (blue),
1278 41.25 mW/m² (red), and 38.65 mW/m² (far-red). Images were acquired every 15 minutes with
1279 the perfect focus system enabled to maintain the correct focal plane.

1280

1281 ***Protein purification***

1282 **Purification of CorM**

1283 CorM with three N-terminal Gly (GGG-CorM) to make it amenable for sortagging was purified
1284 as a N-terminal His_6-SUMO fusion protein expressed from pBS71 in *E. coli* C41 (DE3) cells.
1285 For this, cells were grown at 37 °C, 220 rpm in Terrific Broth (TB) supplemented with Amp and
1286 expression was induced at an OD_{600} 0.5-0.7 with 0.5 mM isopropyl-β-thiogalactopyranoside
1287 (IPTG) for 4 h at 37 °C. Cells were harvested by centrifugation (8,000 x *g,* 20 min at 4 °C) and
1288 cell pellets were scooped out and stored in 50 ml reaction tubes at -70 °C. Cell pellets were
1289 resuspended in HEPES lysis buffer (HLB; 50 mM HEPES, 150 mM KCl, 5 mM $MgCl_2$, 1 mM
1290 DTT, 25 mM imidazole and 10 % glycerol) supplemented with 1x EDTA-free protease inhibitor

1291 cocktail (Roche, Switzerland). Cells were lysed by sonication using Q700 Sonicator equipped
1292 with a 1/2 in horn tip (amplitude 40, 1 sec on + 1 sec off with 10 min on time) and subsequently
1293 incubated with 10 µl DNase I (2500 U/ml; Thermo Fisher Scientific, USA) per every 1 L of initial
1294 bacterial culture volume for 15 min. The lysate was then centrifuged for 30 min at 60,000 x *g*
1295 at 4 °C and the supernatant transferred to HisPur™ Ni-NTA Resin (1 ml per 1 L of initial
1296 bacterial culture volume; Thermo Fisher Scientific, USA) pre-equilibrated with HLB in
1297 incubated with mild agitation for 1-2 h at 4 °C. The mixture was loaded onto a gravity flow
1298 column, the flow through was discarded and the resin was washed with 3x 20 ml HLB. Proteins
1299 were eluted with HEB (HLB with 250 mM imidazole) in 1 ml steps. Eluates were briefly tested
1300 for protein content using a quick and dirty Bradford (Bio-Rad Protein Assay Dye Reagent;
1301 BioRad, USA) assay by adding 2 µl of each elution fraction to 200 µl Bradford assay solution.
1302 Protein fractions that resulted in a discernible blue color shift were pooled and dialyzed over
1303 night at 4 °C against HLB in Pur-A-Lyzer™ Maxi 6000 dialysis tubes (Sigma Aldrich, USA)
1304 supplemented with His-tagged SUMO protease (Ulp1) (ratio of 1:100). The next day, reverse
1305 affinity was performed to remove His-SUMO and His-Ulp1. For this, the solution was subjected
1306 to Ni-NTA (half the volume as used for the initial purification) pre-equilibrated in HLB, incubated
1307 for 1 h at 4 °C and mild rotation. The resin was applied to a gravity flow column and the flow
1308 through was collected followed by 3x washing with 1x column volume (CV) of HLB. The flow
1309 through and the wash fractions were pooled, concentrated using a Vivaspin 20 10KMWCO
1310 centrifugal concentrator (Sartorius, Germany) and subjected to size-exclusion chromatography
1311 (SEC) on an Äkta pure system using a HiLoad 16/600 Superdex 75 PG column (Cytiva, USA)
1312 equilibrated with HEPES storage buffer (HSB, HLB without imidazole). Protein-containing
1313 fractions were pooled, concentrated using another Vivaspin 20 10KMWCO centrifugal
1314 concentrator and then finally flash-frozen in liquid nitrogen and then stored at -70 °C.
1315

1316 **Purification of $^{\Delta 1\text{-}40}$CorM**

1317 $^{\Delta 1\text{-}40}$CorM with three N-terminal Gly (GGG-$^{\Delta 1\text{-}40}$CorM) to make it amenable for sortagging was
1318 purified as a N-terminal His_6-SUMO fusion protein expressed from pBS233 in *E. coli* C41 (DE3)

1319 cells for 3 h at 37 °C with 0.5 mM IPTG. Cell pellets were re-suspended in HLB and lysed as
1320 described for CorM. Cell-free lysates were then subjected to Ni-NTA purification using the Äkta
1321 pure system equipped with a HisTrap^{TM} HP 5 ml column and proteins were eluted in HEB.
1322 Pooled fractions were then subjected to Ulp1 cleavage and dialyzed overnight at 4 °C against
1323 HLB. After subsequent reverse affinity, the flow through and two wash fractions were pooled,
1324 concentrated using a Vivaspin 20 10KMWCO centrifugal concentrator and subjected to
1325 another round of reverse affinity due to remaining contamination with His6-SUMO. The flow
1326 through and two wash fractions were then pooled, and protein purity was confirmed by SDS
1327 polyacrylamide gel electrophoresis (SDS-PAGE) followed by flash-freezing in liquid nitrogen
1328 and storage at -70 °C.
1329
1330 **Purification of EcParM from *E. coli* R1 plasmid**
1331 ParM from *E. coli* NR1 plasmid was expressed from pBS75 with three N-terminal Gly (GGG-
1332 ParM) in C41 (DE3) for 3 h at 37 °C with 0.5 mM IPTG. Lysis and subsequent Ni-NTA-based
1333 purification were done as described for CorM. After the reverse affinity, ParM was concentrated
1334 using a Vivaspin 20 10KMWCO centrifugal concentrator and subjected to buffer exchange to
1335 HSB using a PD-10 desalting column. ParM was again concentrated using a Vivaspin 20
1336 10KMWCO centrifugal concentrator and flash-frozen in liquid nitrogen and then stored at -70
1337 °C.
1338
1339 **Purification of CorR**
1340 CorR was expressed as a N-terminal His_6-SUMO fusion protein from pBS41 in BL21 (DE3) for
1341 3 h at 37 °C with 0.5 mM IPTG or in C41 (DE3) for 18 h at 18 °C with 0.5 mM IPTG. Lysis and
1342 subsequent Ni-NTA-based purification were done as described for GGG-CorM. After the
1343 reverse affinity, flow through and wash fractions were pooled, concentrated using a Vivaspin
1344 20 10KMWCO centrifugal concentrator and subjected to anion exchange chromatography
1345 (AIEX) on Äkta pure system using HiTrap 1ml Q HP anion exchange chromatography column
1346 (Cytiva, USA) equilibrated with no salt buffer (50 mM HEPES pH 7.4, 5 mM $MgCl_2$, 10 %

1347 glycerol). For this, CorR was diluted 1/5 in no salt buffer and subjected to a linear gradient of
1348 no salt and high salt buffer (50 mM HEPES pH 7.4, 1 M KCl, 5 mM $MgCl_2$, 10 % glycerol).
1349 CorR elutes as numerous, not well-defined peaks, likely representing different oligomeric
1350 states of CorR. CorR-containing fractions were pooled, concentrated using a Vivaspin 20
1351 5KMWCO centrifugal concentrator, flash-frozen in liquid nitrogen and stored at -70 °C.
1352

1353 **Purification of $^{\Delta 1\text{-}10}$CorR**

1354 $^{\Delta 1\text{-}10}$CorR was expressed as a N-terminal His_6-SUMO fusion protein from pBS231 in BL21
1355 (DE3) for 3 h at 37 °C with 0.5 mM IPTG. Lysis and subsequent purification steps were done
1356 as described for CorR.
1357

1358 **Purification of $^{\Delta 150\text{-}162}$CorR**

1359 $^{\Delta 150\text{-}162}$CorR was expressed as a N-terminal His_6-SUMO fusion protein from pBS346 in BL21
1360 (DE3) for 16 h at 18 °C with 0.5 mM IPTG. Lysis and subsequent purification steps were done
1361 as described for CorR.
1362

1363 **Purification of ParR**

1364 ParR from *E. coli* NR1 plasmid was expressed as a N-terminal His_6-SUMO fusion protein from
1365 pBS47 in BL21 (DE3) for 3 h at 37 °C with 0.5 mM IPTG. After overnight cleavage with Ulp1,
1366 ParR was subjected to SEC using HiLoad 16/600 Superdex 75 PG equilibrated with HSB.
1367 Protein containing fractions were pooled, supplemented with 10 mM imidazole and subjected
1368 to reverse affinity. The flow through and wash fractions were pooled, concentrated using a
1369 Vivaspin 20 5KMWCO centrifugal concentrator, flash frozen in liquid nitrogen and stored at -
1370 70 °C.
1371

1372 **Purification of MinC**

1373 MinC with three N-terminal Gly (GGG-MinC) to make it amenable for sortagging was purified
1374 as an N-terminal His_6-SUMO fusion protein expressed from pBS316 in *E. coli* BL21 (DE3) or

1375 C41 (DE3) cells for 3 h at 37 °C with 0.5 mM IPTG. Lysis and subsequent Ni-NTA-based
1376 purification were done as described for CorM. After the reverse affinity, MinC was concentrated
1377 using a Vivaspin 20 10KMWCO centrifugal concentrator and was then subjected to SEC using
1378 HiLoad 16/600 Superdex 75 PG column equilibrated with HSB. One major peak was detected
1379 and pooled and proteins subjected to AIEX as described for CorR with a gradient from no salt
1380 to high salt buffer. A single peak was identified, pooled, flash-frozen in liquid nitrogen and
1381 stored at -70 °C.
1382
1383 **Purification of MinC$^{S50A+L55D}$**
1384 MinC$^{S50A+L55D}$ with three N-terminal Gly (GGG-MinC$^{S50A+L55D}$) to make it amenable for
1385 sortagging was purified as a N-terminal His$_6$-SUMO fusion protein expressed from pBS353 in
1386 *E. coli* BL21 (DE3) cells for 4 h at 37 °C with 0.5 mM IPTG. Lysis and subsequent Ni-NTA-
1387 based purification were done as described for CorM. After the reverse affinity, MinC$^{S50A+L55D}$
1388 was concentrated using a Vivaspin 20 10KMWCO centrifugal concentrator and was then
1389 subjected to AIEX as described for CorR. Due to remaining contamination with His6-SUMO,
1390 another reverse affinity step was included, the flow through and wash steps were collected,
1391 pooled and then dialyzed overnight at 4 °C against HSB in Pur-A-Lyzer™ Maxi 6000 dialysis
1392 tubes. Afterwards, MinC$^{S50A+L55D}$ was concentrated using a Vivaspin 20 10KMWCO centrifugal
1393 concentrator, flash-frozen in liquid nitrogen and stored at -70 °C.
1394
1395 **Purification of $^{\Delta 46-67}$MinC**
1396 $^{\Delta 46-67}$MinC with three N-terminal Gly (GGG-$^{\Delta 46-67}$MinC) to make it amenable for sortagging was
1397 purified as a N-terminal His$_6$-SUMO fusion protein expressed from pBS354 in *E. coli* BL21
1398 (DE3) cells for 4 h at 37 °C with 0.5 mM IPTG. $^{\Delta 46-67}$MinC was purified as described for
1399 MinC$^{S50A+L55D}$.
1400

1401 ***Peptide labelling***

1402 For labelling of peptide for subsequent sortagging reactions, we obtained dried CLPETGG
1403 peptides from Biomatik (USA). 1.5 mg of the peptide was dissolved in 50 mM HEPES pH 7.4
1404 to a final concentration of 100 mM. Alexa Fluor™ 488 (Alexa488; Thermo Fisher Scientific) C5
1405 Maleimide and Sulfo-Cyanine5 maleimide (Lumiprobe, Germany) were dissolved in DMSO to
1406 obtain a 150 mM solution. For extended storage, dissolved dyes were stored at -70 °C. A
1407 roughly 2x molar excess of TCEP was added to the reconstituted peptide (i.e., 10 µl of peptide
1408 and 5 µl of 0.4 M TCEP) to obtain a 66 mM peptide solution. Afterwards, a roughly 3x molar
1409 excess of dye was added to the peptide+TCEP mix (i.e., 20 µl of dye was added leading to a
1410 peptide concentration of roughly 28 mM and a dye concentration of roughly 86 mM). The
1411 reaction was then incubated over night at RT protected from light. The next day, 2 µl of 2-
1412 mercaptoethanol was added to quench unreacted maleimide dye. The 25 mM peptide solution
1413 was then flash-frozen in liquid nitrogen and stored at -70 °C.

1414

1415 ***Protein labelling - Sortagging***

1416 For Sortase-based N-terminal fluorescence labelling, we routinely prepare 1 or 2 ml reactions
1417 of 50 µM GGG-CorM, 0.5 mM labelled peptides (Alexa488-LPETGG or Cy5-LPETGG) and 10
1418 µM Sortase 7M in HSB, which are then incubated overnight at 4 °C in the dark with gentle
1419 rotation. The next day, 3 µl of 2-mercaptoethanol was added to the reaction to quench all
1420 unreacted dye and incubated for 15 min at 4 °C. The reactions were supplemented with 25
1421 mM imidazole (final) and 300 µl pre-equilibrated Ni-NTA slurry was added. After incubation for
1422 60 min at 4 °C with mild rotation, the solution was applied to a gravity flow column and the flow
1423 through was collected. The Ni-NTA was washed 2x with 1x column volume HDB and pooled
1424 with the flow through. To remove unbound labelled peptide and to exchange the buffer to HSB,
1425 Cy5-CorM was then subjected to a PD-10 desalting column (Cytiva, USA) and eluted protein
1426 was concentrated using a Vivaspin 2 10KMWCO centrifugal concentrator (Sartorius,
1427 Germany). For Alexa488-CorM, unbound labelled peptide and imidazole traces were removed
1428 by size-exclusion chromatography on a Superdex 75 Increase 10/300 GL (Cytiva, USA) using

1429 HSB. Protein-containing peaks were then again concentrated using a Vivaspin 2 10KMWCO
1430 centrifugal concentrator and in both cases protein concentration was measured using
1431 NanoDrop One and labelling efficiency was calculated based on the ratio of the concentration
1432 of fluorescence dye (equals labelled protein) to the protein concentration. In both cases,
1433 labelling efficiency was about 30 %. Finally, labelled proteins were flash-frozen in liquid
1434 nitrogen and stored at -70 °C.
1435
1436 ***Piranha treatment of coverslips for TIRF microscopy***
1437 TIRF-suitable glass coverslips (18X18 mm NR 1.5 high precision cover glasses; Marienfield,
1438 Germany) in a custom-made Teflon holder were subjected to piranha solution (mixture of 50
1439 ml 30 % H_2O_2 and 150 ml H_2SO_4) for 2 h at RT until the solution cooled down to RT. Cover
1440 slips were then washed 10x with 500 ml MiliQ H_2O, sonicated in a sonicator bath (VWR
1441 Ultrasonic Cleaner USC - TH) for 20 min and washed again 4x with 500 ml MiliQ H_2O and
1442 finally stored at RT in 500 ml MiliQ H_2O for no longer than 2 weeks. For TIRF microscopy,
1443 coverslips were dried by compressed air and reaction chambers made of 0.5 ml reaction tubes
1444 (cut in half to create a chamber without the conical end) were glued onto the coverslips with a
1445 UV-reactive glue (Norland Optical Adhesive 63) for 2 min under UV light exposure.
1446
1447 ***Preparation of multilaminar vesicles and small unilaminar vesicles***
1448 For pelleting assays and TIRF microscopy experiments we used DOPC (1,2-dioleoyl-sn-
1449 glycero-3-phosphocholine) and DOPG (1,2-dioleoyl-sn-glycero-3-phospho-(1′-rac-glycerol)) *E.*
1450 *coli* polar lipids (Avanti, USA) dissolved in chloroform (stock concentration 2.5 mg) at a ratio of
1451 67:33 mol %. Lipids were mixed in a glass vial and then dried in a stream of nitrogen gas.
1452 Residual chloroform was removed from the lipids by vacuum desiccation for at least 3 h or
1453 overnight. Afterwards, lipids were resuspended by vortexing in HEPES reaction buffer (HRB;
1454 50 mM HEPES [pH 7.4], 150 mM KCl, 5 mM $MgCl_2$) to obtain a 5 mM large multilaminar
1455 vesicles (MLVs) solution. To prepare small MLVs, this solution was then incubated at 37 °C
1456 for 30 min and then subjected to 7x freeze-thaw cycles using a dry ice-isopropanol bath and

1457 hot tap water. Small MLVs were then subjected to centrifugation at 21,000 x *g*, 4 °C, 30 min
1458 and the supernatant was transferred to a new reaction tube, which was then overlayed with
1459 argon gas and stored at 4 °C until further use. For preparation of small unilaminar vesicles
1460 (SUVs), small MLVs were subjected to tip-sonication (Q700 Sonicator equipped with a 1.6 mm
1461 tip) on ice with the following settings: amplitude 1; 1 s on time, 4 s off time; total 5 min on time.
1462 Afterwards, SUVs were centrifuged for 20 min at 21,000 x *g*, 4°C and the supernatant was
1463 transferred to a new tube and overlayed with argon gas.
1464
1465 ***Supported lipid bilayer preparation***
1466 For the preparation of supported lipid bilayers (SLBs), 100 µl reactions were prepared in
1467 reaction chambers containing 89 µl HRB, 0.5 mM SUVs and vesicle rupture was induced by
1468 adding 5 mM $CaCl_2$ to the SUVs. For fusion of the ruptured vesicles with the piranha-treated
1469 glass coverslips, chambers were incubated for 20 min at 37 °C followed by extensive washing
1470 with 6x 200 µl HRB to remove unfused vesicles. Chambers were again washed 3x with 200 µl
1471 HRB right before each individual experiment. SLBs were prepared fresh for each experiment
1472 day.
1473
1474 ***Total Internal Reflections Fluorescence microscopy***
1475 For Total Internal Reflections Fluorescence (TIRF) microscopy, 0.75 µM unlabeled CorM or $^{\Delta 1-}$
1476 ^{40}CorM, 0.25 µM Alexa488-CorM or Alexa488-$^{\Delta 1-40}$CorM, 0.25 µM CorR and an oxygen
1477 scavenger mix composed of 1 µM glucose oxidase from *Aspergillus niger* (Merck, USA), 332
1478 nM catalase from bovine liver (Merck, USA), 11 mM D-glucose, 1 mM DTT and 1 mM Trolox
1479 was used. The equal amount of buffer in the reaction chambers containing the SLBs was
1480 removed and only then all components were added to the chambers. CorM polymerization on
1481 SLBs was induced by the addition of 2.5 mM ATP and CorM polymers were observed by TIRF
1482 imaging. To test for the effect of different CorR concentrations, the same kind of reactions were
1483 prepared but with varying indicated CorR concentrations.

1484 For dual color imaging to study the localization of individual CorM monomers within a CorM
1485 protein filament, a mixture of either 1 µM Alexa488-CorM + 265 pM Cy5-CorM + 0.25 µM CorR
1486 or 0.25 µM Alexa488-CorM + 265 pM Cy5-CorM + 0.75 µM CorM + 0.25 µM CorR was added
1487 to the reaction chambers together with the oxygen scavenger mix. Time-lapse movies were
1488 recorded between 2-5 min after addition of 2.5 mM ATP to the reaction.
1489 To test for the effect of MinC, $MinC^{S50A+L55D}$ and $^{\Delta 46-67}$MinC addition on CorM filaments *in vitro*,
1490 CorM filaments were polymerized on SLBs in the presence of CorR and 2.5 mM ATP for about
1491 5 min upon which equal molar amounts of MinC or MinC mutants (i.e., 1 µM) was added to the
1492 chambers during time lapse imaging. Movies were recorded for 3 min each.
1493
1494 ***Fluorescence recovery after photobleaching experiments***
1495 For FRAP analysis, 3 - 6 pre-bleach frames were acquired, followed by photobleaching of a
1496 defined rectangular region of interest (ROI) using 80 % 488 nm laser power and a pixel dwell
1497 time of 100 µs/pixel. Fluorescence recovery within the ROI was subsequently recorded at a
1498 rate of 1 frame per second.
1499
1500 ***Pelleting assay***
1501 Two types of pelleting assays were performed in this study. One did not involve MLVs and
1502 relied on ultracentrifugation-based pelleting of protein polymers while the other employed the
1503 intrinsic binding capacity of proteins to MLVs. Pelleting assays with MLVs were either
1504 performed in a suspension with or without 0.93 mM small MLVs and proteins at indicated
1505 concentration were incubated for 30 min at 30 °C in HRB supplemented with 2.5 mM ATP.
1506 Unless otherwise stated, proteins were supplied at 5 µM. Afterwards, samples were
1507 centrifuged for 20 min at 30 °C, 21,000 x *g*. For experiments without MLVs, proteins were
1508 incubated in HRB with or without 2.5 mM of indicated nucleotide, incubated for 30 min at 30
1509 °C and centrifuged for 45 min, 436,000 x *g* at 30 °C. In both cases, the supernatant (S) of each
1510 reaction was collected and supplemented with an appropriate amount of 6x Laemmli SDS
1511 sample buffer (Thermo Fisher Scientific, USA). The pellet (P) was resuspended in 50 µl 1x

1512 Laemmli SDS sample buffer. Between 15-25 µl of pellet and supernatant samples were applied
1513 to SDS-PAGE using SurePAGE™ Bis-Tris 4-20 % gels (GenScript, USA). Upon protein
1514 separation, gels were stained with Quick Coomassie® Stain (Serva, Germany) and protein
1515 bands were recorded in a ChemiDoc MP or ChemiDoc Go system (BioRad, USA).
1516
1517 ***ATPase assay***
1518 For ATPase assays, we employed the Malachite Green Phosphate Assay Kit (Sigma Aldrich,
1519 USA) according to the manufacturer's instructions. Proteins at indicated concentrations were
1520 incubated in ATPase reaction buffer (25 mM HEPES [pH 7.4], 150 mM KCl, 1 mM $MgCl_2$) and
1521 if appropriate, supplemented with 1 mM ATP or GTP. Samples were incubated at 30 °C
1522 measurements were performed either as endpoint measurements after 2 h or in a time course
1523 manner (15, 30, 60, 120 min after ATP addition) of 1/8 dilutions and OD_{620} values were
1524 recorded in a Spectramax M2e (Molecular Devices, USA) plate reader. As controls, samples
1525 containing no nucleotide or nucleotide only (without protein) were included.
1526
1527 ***Electrophoretic mobility shift (EMSA) assay***
1528 For EMSA assays, test DNA sequences were amplified by PCR using Q5 polymerase (NEB,
1529 USA) with primer pairs (oBS249+oBS253 for P_{corMR} and oBS627+oBS729 for P_{parMR}) that each
1530 contained one unlabeled (oBS253 and oBS729) and one 5' Alexa488-labelled primer (oBS249
1531 and oBS627). PCR products were purified by PCR clean-up using Monarch® PCR & DNA
1532 Cleanup Kit (NEB, USA) and stored at -20 °C until further use. 150 ng DNA per sample was
1533 then incubated for 30 min at RT with indicated concentrations of CorR or ParR in EMSA
1534 reaction buffer (ERB; 25 mM HEPES [pH 7.4], 150 mM KCl, 1 mM $MgCl_2$, 1 mM DTT, 0.1
1535 mg/ml BSA, 0.1 mg/ml UltraPure™ Salmon Sperm DNA Solution (Thermo Fisher Scientific,
1536 USA), 5% glycerol). Samples were then loaded onto 5% Mini-PROTEAN® TBE Gel (BioRad,
1537 USA) without any loading dye and run in 1x TBE buffer (130 mM Tris, 45 mM boric acid, 2.5
1538 mM EDTA) at 100 V for 1 h. Finally, Alexa488 signal was recorded in a ChemiDoc MP system
1539 (BioRad, USA).

1540 ***in vivo CorM filament angle measurement***

1541 To measure the angle of CorM filaments in *Anabaena* cells, we used two approaches. For the
1542 first, we initially straightened *Anabaena* cells expressing mNG-CorM from obtained images
1543 using an in house ImageJ script ("straighten_2D"), and filament angles were then measured
1544 using CytoSpectre[83]. Alternatively, angles were measured manually in ImageJ using the angle
1545 tool by following an imaginary line from one cell pole to the other and then following each
1546 individual mNG-CorM filament from the point of contact with this imaginary pole-to-pole line.
1547 Both methods resulted in comparable results.

1548

1549 ***Sample preparation for cryo-EM***

1550 For CorM and CorMR samples, 5 µM of CorM alone or 5 µM of both CorM and CorR proteins
1551 were incubated in a buffer containing 25 mM HEPES (pH 7.4), 150 mM KCl, 1 mM $MgCl_2$, and
1552 2 mM ATP for 2 hours at 30 °C. The samples were diluted 1/10 in the same buffer and 3 µL of
1553 sample were applied onto glow-discharged 200-mesh holey carbon girds (Quantifoil Micro
1554 Tools, Au R2/2).

1555 In the case of $^{\Delta 1\text{-}40}$CorM, 5 µM of the protein was pre-mixed in the same buffer but without ATP.
1556 ATP was only subsequently added to this mixture and 3.5 µl of the sample were applied onto
1557 glow-discharged 200-mesh holey carbon girds (Quantifoil Micro Tools, Cu R1.2/1.3) after an
1558 incubation of 1 min at RT. These two modifications were necessary as $^{\Delta 1\text{-}40}$CorM otherwise
1559 readily formed extensive, interconnected protein networks within a few minutes after ATP
1560 addition that were unsuitable for cryo-EM analysis. All the samples were vitrified in liquid
1561 ethane (-185 °C) after 3-3.5s back-side blotting using a Leica GP2 plunger (Leica
1562 Microsystems) maintained at 80% humidity and 25 °C (chamber conditions). The grids were
1563 stored in liquid nitrogen conditions until imaging.

1564

1565 ***Cryo-electron microscopy***

1566 Single-particle datasets were acquired under cryogenic conditions on a Glacios TEM
1567 microscope (Thermo Fisher Scientific) operating at 200 kV equipped with Falcon 4i direct

1568 electron detector. The automated data collection was set up using EPU version 3.7.0 (Thermo
1569 Fisher Scientific). The nominal magnification was set to 150,000x, resulting in a pixel size of
1570 0.931 Å for the CorMR dataset and 0.9551 Å for the CorM and $^{\Delta 1\text{-}40}$CorM datasets. The defocus
1571 range was set to -1.0 to -3 µm. For all three samples, single-particle datasets were acquired in
1572 4,096x4,096px movies in EER mode, with a cumulative dose ranging from 40-80 $e^-/Å^2$.
1573
1574 ***Single-particle image processing***
1575 All the processing steps were performed in CryoSPARC v4.4. For all the datasets,
1576 4,096x4,096px movies in EER mode were motion corrected using patch motion correction, and
1577 patch CTF estimation was used to estimate CTF using default patch size in cryoSPARC.
1578 Manual curation was done to remove empty micrographs and micrographs containing
1579 crystalline ice. The subsequent steps used to process each dataset are summarized below
1580 and the details are provided in the schematics presented in Fig. S6.1-6.3.
1581 For the CorMR dataset, initial particle picking was performed using filament tracer with a
1582 diameter of 90 Å on 2,305 manually curated micrographs. Particles were initially extracted with
1583 a box size of 256 px, followed by 2D classification was performed. Three classes were used
1584 as template to perform filament tracing with a diameter of 100 Å. Particles were extracted with
1585 a bigger box size (512px) and subjected to 2D classification. Using selected 2D classes (22
1586 classed out of 100), ab-initio reconstruction and homogeneous refinement were performed
1587 without symmetry (C1 symmetry). The initial map obtained from homogeneous refinement was
1588 used to determine the helical twist and helical rise estimates using the online helical indexing
1589 tool (HI3D- Helical Indexing using cylindrical projection of a 3D map)[79]. Helical refinement was
1590 performed using an estimated helical twist of -18° and a helical rise 46.5 Å. Local refinement
1591 and local CTF refinements were performed after helical refinement and the map clearly
1592 displayed C2 symmetry. Two rounds of homogeneous refinement were performed after
1593 removing duplicate particles to obtain a final map at 3.92 Å with 124,109 particles, measured
1594 at the 0.143 FSC criterion.

1595 For the $^{\Delta 1\text{-}40}$CorM dataset, particle picking was performed using filament tracer with a diameter
1596 of 100 Å on 1,200 manually curated micrographs. Particles were extracted with a box size of
1597 512px and subject to 2D classification. Using selected 2D classes (10 classed out of 75), ab-
1598 initio reconstruction and homogeneous refinement were performed with C1 symmetry. The
1599 initial map obtained from homogeneous refinement was used to determine the helical twist and
1600 helical rise estimates using online helical indexing tool (HI3D- Helical Indexing using cylindrical
1601 projection of a 3D map)[79]. Helical refinement was performed using the estimated helical twist
1602 of -15.73° and helical rise 47.3 Å. The map from helical refinement had 287,700 particles, 3D
1603 classification was performed to get 3 different classes. One class with good looking map
1604 containing 44.2 % of the particles (127,289 particles) was selected and used for final helical
1605 refinement to obtain a 4.42 Å map, measured at the 0.143 FSC criterion.
1606 For the CorM dataset, initial particle picking was performed using filament tracer with a
1607 diameter of 100 Å with 5 Å separation distance on 2,305 manually curated micrographs.
1608 Particles were extracted with box size of 512 px and 2D classification was performed. 22
1609 Classes out of 100 classes were used as template to perform filament tracing with a diameter
1610 of 100 Å and 1 Å separation distance. Particles were extracted with a box size of 360px and
1611 subjected to rigorous 2D classification (4 rounds). Using selected 2D classes, ab-initio
1612 reconstruction and homogeneous refinement were performed with C1 symmetry. At this stage,
1613 the particles were re-extracted with a bigger box size (512px). One more round of 2D
1614 classification was performed to remove bad particles. Using selected 2D classes, ab-initio
1615 reconstruction and homogeneous refinement were performed with C1 symmetry. The initial
1616 map obtained from homogeneous refinement was used to determine the helical twist and
1617 helical rise estimates using online helical indexing tool (HI3D- Helical Indexing using cylindrical
1618 projection of a 3D map)[79]. Helical refinement was performed using estimated helical twist of -
1619 18.5 ° and helical rise 46.5 Å. The map from helical refinement had 197,123 particles, 3D
1620 classification was performed to get 3 different classes. Two classes with good looking map
1621 containing 78.3 % of the particles (154,726 particles) were combined and used for final helical
1622 refinement job to obtain a 7.14 Å map, measured at the 0.143 FSC criterion.

1623 ***Model building and refinement***

1624 All model and EM-density visualizations were done in UCSF ChimeraX version 1.9 (2024-12-
1625 11)[76]. Model building and refinement was performed using the ISOLDE plugin (v.19)[84] in
1626 ChimeraX.

1627 To build a model of the CorM filament, we first predicted CorM using the AlphaFold3 (AF3)[75]
1628 webserver, either in its APO-form or bound with ADP or ATP. These predicted models were
1629 then rigid body-fitted into the EM density of the filament structure obtained from the CorMR
1630 sample. This revealed that the APO-model showed the best fit. However, as there was clearly
1631 a density for the nucleotide visible, we manually placed an ADP molecule into the EM-density.
1632 As we only observed densities for residues Serine 43 to Asparagine 378 we removed the
1633 remaining residues.

1634 To generate a filament-like model, we then rigid body-fitted 6 copies of the generated CorM(43-
1635 378)-ADP monomer into the EM-density of the filament. 5 non-crystallographic symmetry
1636 copies of the monomers were restrained to a centrally positioned (working) monomer (i.e. a
1637 monomer that was surrounded by 5 copies, hence having all its contact sites occupied). Fit
1638 and geometry of the working monomer were iteratively checked and locally refined in ISOLDE.
1639 Finally, the NCS copies were replaced with the working copy monomer to obtain the final CorM-
1640 filament model.

1641 The accuracy of the model was checked using MolProbity[85]. The interface interactions within
1642 CorM filament structures were determined using PDBePISA (Proteins, Interfaces, Structure
1643 and Assemblies)[52].

1644

1645 ***Scanning electron microscopy (SEM)***

1646 For SEM analysis, cells were grown on BG11 plates, scraped off, and re-suspended in 1 ml
1647 MilliQ H_2O. Cells were pelleted by centrifugation (5000 × *g*, 4 min, RT), washed once by
1648 centrifugation with 1 ml Milli-Q H_2O, and then re-suspended in 1 ml of 0.1 M Tris base/HCl
1649 buffer containing 2.5% glutaraldehyde. Cells were fixed o/n at 4 °C. The next day, cells were
1650 washed 2x with 1 ml MilliQ H_2O by centrifugation (5000 × *g*, 4 min, RT). After washing, cells

1651 were spotted for 30 seconds onto 12 mm round glass coverslips (Electron Microscopy
1652 Sciences, USA) previously coated overnight with 0.01% poly-L-lysine (Sigma-Aldrich, USA).
1653 Subsequently, cells were subjected to an ethanol dehydration series by sequential incubation
1654 on the coverslips in 6-well plates with 40 %, 60 %, 80 %, and 100 % EtOH, each for 15 minutes.
1655 Samples were then critical point dried using EM CPD300 (Leica Microsystems) and sputter-
1656 coated with gold to a thickness of 5 nm using EM ACE600 coating device (Leica Microsystems)
1657 prior to imaging using a FE-SEM Merlin VP Compact (Zeiss, Germany) at 5 kV with a
1658 secondary electron detector.
1659
1660 ***Protein sequence analyses***
1661 We assembled a database of complete cyanobacterial genomes, aiming to represent the
1662 overall diversity of the phylum included in the NCBI Genome database[86] by including up to five
1663 species per genus when available, resulting in a final dataset of 128 species. To identify
1664 homologs of ParM, we used the *Nostoc* sp. PCC 7120 protein WP_044522477.1 as a query in
1665 a jackhmmer search (HMMER v3.3.2)[87] against our cyanobacterial database. All hits were
1666 aligned using MAFFT v7 (L-INS-i algorithm)[88], and the resulting alignment was manually
1667 curated to remove outliers. From this alignment, we generated a hidden Markov model (HMM),
1668 which we used for a second round of searches with hmmsearch[87]. The same approach was
1669 applied to identify homologs of MinC (WP_190449770.1) and ParR (WP_010999216.1), both
1670 from *Nostoc* sp. PCC 7120, but in the case of ParR, additional analyses were necessary due
1671 to its low sequence conservation and variable length across homologs. To address these
1672 limitations, ParR hits were filtered based on genomic context. In all reported cases, *parR* was
1673 located adjacent to a predicted *parM* gene, and both genes were encoded in the same
1674 orientation. Based on this observation, we only retained ParR hits found immediately next to a
1675 ParM, and all others were discarded. We also examined the distribution of ParM across
1676 Bacteria. Preliminary analyses showed that ParM is unevenly distributed and can be present
1677 in some strains but absent in others within the same species. For this reason, we used a
1678 different strategy than the one applied to Cyanobacteria. We searched all complete bacterial

1679 chromosomes and plasmids deposited in RefSeq[89], excluding cyanobacterial entries, using
1680 hmmsearch with the ParM HMM and an E-value cutoff of 1e−6. This search retrieved 3,693
1681 chromosomal and 2,298 plasmid hits, the majority of which belonged to the phyla
1682 Pseudomonadota and Bacillota, which together accounted for over 95% of all identified
1683 sequences. To reduce redundancy, we randomly selected one hit per genus, aligned all
1684 sequences using MAFFT v7 (L-INS-i algorithm)[88], and manually removed highly divergent or
1685 poorly aligned entries. The resulting curated dataset consisted of 150 chromosomal and 78
1686 plasmid sequences. Given the poor sequence conservation of ParR described above, we did
1687 not rely on direct sequence similarity to search for its homologs across Bacteria. Instead, we
1688 extracted the two neighboring genes (upstream and downstream) of each ParM hit, provided
1689 they were in the same orientation, and predicted their three-dimensional structures using
1690 AlphaFold2[54]. ParR candidates were then manually annotated based on structural similarity to
1691 the ParR reference sequence. The presence of MinC homologs in other bacterial phyla was
1692 assessed as previously described, but using a database containing taxa representative of most
1693 bacterial phyla[90]. To predict amphipathic helices in all the selected ParR sequences, we used
1694 Amphipaseek[51]. Helical wheels were generated using NetWheels[91] and amphipathicity was
1695 calculated using PMIpred[92]. All protein alignments for ParM, ParR and MinC were performed
1696 using MAFFT[88], and columns containing more than 20% gaps were removed using TrimAl[93].
1697 Alignments were visualized in JalView[94]. Sequence logos were generated using WebLogo 3[78].
1698 To analyze and display sequence conservation on protein structures, we used ChimeraX[95] in
1699 combination with the AL2CO algorithm[96].
1700
1701 ***Phylogenetic analyses***
1702 To reconstruct the phylogenies of ParM and MinC, we used all homologs identified in
1703 Cyanobacteria and in the Bacteria datasets. Phylogenetic inference was performed with IQ-
1704 TREE v2[97], using ModelFinder[98] to determine the best-fitting substitution model, and ultrafast
1705 bootstrap approximation with 10,000 replicates[99] and a minimum bootstrap correlation
1706 coefficient of 0.9999 to assess branch support. To improve resolution within the cyanobacterial

1707 clade, we reconstructed a second phylogeny based on concatenated alignments of ParM and
1708 ParR sequences, processed using the same strategy as described above. We also built a
1709 species tree for Cyanobacteria using two conserved, assumed to be vertically inherited
1710 markers: the DNA-directed RNA polymerase subunits β (BAB77960.1) and β′ (BAB77961.1).
1711 Each sequence was aligned and trimmed separately using the same method explained above,
1712 and the two alignments were concatenated for phylogenetic analysis. The resulting tree was
1713 rooted using four species from *Candidatus* Melainabacteria, the sister clade of Cyanobacteria.
1714 All phylogenetic trees were visualized and annotated using the iTOL web server v6[100].
1715

1716 ***In vivo CorM filament tracking***

1717 mNG-CorM or mNG-$^{\Delta 1\text{-}40}$CorM filaments were tracked from time lapse movies with images
1718 recorded usually every 5 or 10 seconds. Using Fiji[101], we used the line tool (width 3) and
1719 followed the track of individual filaments of which we generated kymographs using the Reslice
1720 plugin. Growth or shrinkage velocities were then calculated by distance traveled over time
1721 (nm/s).
1722

1723 ***In vitro CorM filament tracking***

1724 Filament ends were manually tracked using the Tracking plugin in Fiji[101]. Distance between
1725 positions were then calculated using a custom Python script.
1726

1727 ***Intrinsically disordered region (IDR) prediction***

1728 Unstructured domains of cyanobacterial CorM or ParM homologs was performed using
1729 ALBATROSS[102] on a Google Colab notebook (IDRome constructor v. 3.0).
1730

1731 ***AlphaFold-Multimer predictions***

1732 For prediction of protein-protein interactions, we tested CorM against the whole *Anabaena*
1733 proteome (RefSeq ID: GCF_000009705.1) as extracted from NCBI. This 'candidates' list was
1734 tested to predict interactions against the 'bait' CorM using AlphaFold-Multimer (v.2.3)[53,75]. This

1735 pipeline produced five protein complexes per protein pair. Postprocessing of the results
1736 includes a filtering step, which removes protein complexes with an ipTM standard deviation
1737 larger than the 1.5xIQR outlier threshold, i.e. 0.095, indicate highly diverse structure
1738 predictions. Unless stated otherwise, all depicted complex predictions and their corresponding
1739 PAE plots are the top-scoring relaxed model generated by Alphafold-Multimer (v3) 64 and
1740 visualized in ChimeraX.
1741
1742 ***Prediction of protein 3D structures***
1743 All shown Protein 3D structures were predicted using AF3[75] and further analyzed using UCSF
1744 ChimeraX (v. 1.9)[76]. For AF3 predictions, the respective top ranked model is shown in cartoon
1745 form and colored by pLDDT score confidence together with the corresponding Predicted
1746 Aligned Error (PAE) plot and the ipTM/pTM scores.
1747
1748 ***Image and data analysis***
1749 Microscopy data analysis was performed using FIJI software (ImageJ2 for Mac; v.
1750 2.14.0/1.54f)[101]. Time series micrographs were routinely processed using the ImageJ gaussian
1751 blur (0.5) and walking average plugins, averaging four consecutive frames. Contrast was
1752 optimized using the Enhance Contrast command (0.05-0.35% saturated pixels; normalize,
1753 process all slices) and, where appropriate, background was subtracted using the Subtract
1754 Background command (50 pixels Rolling ball radius) from ImageJ.
1755 Quantification of protein signals from SDS gels was done using Fiji or Image Lab (BioRad,
1756 USA) software. Protein signal intensities of the loaded pellet and supernatant samples were
1757 recorded and extrapolated to the overall sample volume. Values are given as percentage of
1758 proteins in the pellet or supernatant in respect to the whole protein amount of each reaction.
1759
1760 ***In vivo timelapse cell division tracking***
1761 To analyze the temporal localization of mNG-CorM, time-lapse movies of individual cells were
1762 manually stabilized using a custom Fiji macro to compensate for cell growth, division, rotation,

1763 and lateral drift. Frame intensities were normalized to ensure accurate assessment of signal
1764 localization, and each cell was cropped into a 100×100 pixel region. Initial stabilization was
1765 performed by aligning movie frames to a line region of interest (ROI) positioned along the cell's
1766 lateral axis, guided by mNG-CorM and thylakoid membrane fluorescence signals, to correct
1767 for rotation. After stabilization, a kymograph was generated for each cell by drawing a line
1768 along the longitudinal axis, spanning from pole to pole, with a line width of 1.25 μm to average
1769 the mNG-CorM signal and compensate for gaps in fluorescence. These kymographs were
1770 temporarily aligned based on the onset of cell division, defined by the sudden separation of
1771 the mNG-CorM signal into two diverging trajectories. The aligned kymographs were then
1772 stacked and averaged to produce the composite final image.
1773
1774 ***Statistical analysis***
1775 For all plots throughout this work, error bars indicate the standard deviation (SD).
1776 For TIRF microscopy of *in vitro* experiments, we define a biological replicate as a reaction
1777 performed in a separate reaction chamber. In some cases, replicates were performed on the
1778 same cover glasses, which can hold up to three reaction chambers. A normal distribution was
1779 assumed for all replicates.
1780
1781 **References:**
1782 1. Wagstaff, J., and Löwe, J. (2018). Prokaryotic cytoskeletons: protein filaments
1783 organizing small cells. Nat. Rev. Microbiol. *16*, 187–201.
1784 https://doi.org/10.1038/nrmicro.2017.153.
1785 2. Møller-Jensen, J., Borch, J., Dam, M., Jensen, R.B., Roepstorff, P., and Gerdes, K.
1786 (2003). Bacterial Mitosis: ParM of Plasmid R1 Moves Plasmid DNA by an Actin-like
1787 Insertional Polymerization Mechanism. Mol. Cell *12*, 1477–1487.
1788 https://doi.org/10.1016/S1097-2765(03)00451-9.
1789 3. Bi, E., and Lutkenhaus, J. (1991). FtsZ ring structure associated with division in
1790 Escherichia coli. Nature *354*, 161–164. https://doi.org/10.1038/354161a0.

1791 4. Loose, M., and Mitchison, T.J. (2014). The bacterial cell division proteins ftsA and ftsZ
1792 self-organize into dynamic cytoskeletal patterns. Nat. Cell Biol. *16*, 38–46.
1793 https://doi.org/10.1038/ncb2885.
1794 5. Shiomi, D., and Margolin, W. (2007). Dimerization or oligomerization of the actin-like
1795 FtsA protein enhances the integrity of the cytokinetic Z ring. Mol. Microbiol. *66*, 1396–
1796 1415. https://doi.org/https://doi.org/10.1111/j.1365-2958.2007.05998.x.
1797 6. Garner, E.C., Bernard, R., Wang, W., Zhuang, X., Rudner, D.Z., and Mitchison, T.
1798 (2011). Coupled, circumferential motions of the cell wall synthesis machinery and
1799 MreB filaments in B. subtilis. Science (80-.). *333*, 222–225.
1800 https://doi.org/10.1126/science.1203285.
1801 7. Ramm, B., Heermann, T., and Schwille, P. (2019). The E. coli MinCDE system in the
1802 regulation of protein patterns and gradients. Cell. Mol. Life Sci. *76*, 4245–4273.
1803 https://doi.org/10.1007/s00018-019-03218-x.
1804 8. Flores, E., and Herrero, A. (2014). The cyanobacteria: morphological diversity in a
1805 photoautotrophic lifestyle.
1806 9. Rippka, R., Stanier, R.Y., Deruelles, J., Herdman, M., and Waterbury, J.B. (1979).
1807 Generic Assignments, Strain Histories and Properties of Pure Cultures of
1808 Cyanobacteria. Microbiology *111*, 1–61. https://doi.org/10.1099/00221287-111-1-1.
1809 10. Herrero, A., Stavans, J., and Flores, E. (2016). The multicellular nature of filamentous
1810 heterocyst-forming cyanobacteria. FEMS Microbiol. Rev. *40*, 831–854.
1811 https://doi.org/10.1093/femsre/fuw029.
1812 11. Hoiczyk, E., and Baumeister, W. (1995). Envelope structure of four gliding filamentous
1813 cyanobacteria. J. Bacteriol. *177*, 2387–2395. https://doi.org/10.1128/jb.177.9.2387-
1814 2395.1995.
1815 12. Kieninger, A.K., and Maldener, I. (2021). Cell–cell communication through septal
1816 junctions in filamentous cyanobacteria. Curr. Opin. Microbiol. *61*, 35–41.
1817 https://doi.org/10.1016/j.mib.2021.02.002.
1818 13. Weiss, G.L., Kieninger, A.-K., Maldener, I., Forchhammer, K., and Pilhofer, M. (2019).

1819 Structure and Function of a Bacterial Gap Junction Analog. Cell *178*, 374-384.e15.
1820 https://doi.org/10.1016/J.CELL.2019.05.055.
1821 14. Miyagishima, S.Y., Wolk, P.P., and Osteryoung, K.W. (2005). Identification of
1822 cyanobacterial cell division genes by comparative and mutational analyses. Mol.
1823 Microbiol. *56*, 126–143. https://doi.org/10.1111/j.1365-2958.2005.04548.x.
1824 15. Springstein, B.L., Weissenbach, J., Koch, R., Stücker, F., and Stucken, K. (2020). The
1825 role of the cytoskeletal proteins MreB and FtsZ in multicellular cyanobacteria. FEBS
1826 Open Bio *10*, 2510–2531. https://doi.org/https://doi.org/10.1002/2211-5463.13016.
1827 16. Naha, A., Haeusser, D.P., and Margolin, W. (2023). Anchors: A way for FtsZ filaments
1828 to stay membrane bound. Mol. Microbiol. *120*, 525–538.
1829 https://doi.org/10.1111/mmi.15067.
1830 17. Camargo, S., Picossi, S., Corrales-Guerrero, L., Valladares, A., Arévalo, S., and
1831 Herrero, A. (2019). ZipN is an essential FtsZ membrane tether and contributes to the
1832 septal localization of SepJ in the filamentous cyanobacterium Anabaena. Sci. Rep. *9*,
1833 1–15. https://doi.org/10.1038/s41598-019-39336-6.
1834 18. MacCready, J.S., Schossau, J., Osteryoung, K.W., and Ducat, D.C. (2017). Robust
1835 Min-system oscillation in the presence of internal photosynthetic membranes in
1836 cyanobacteria. Mol. Microbiol. *103*, 483–503. https://doi.org/10.1111/mmi.13571.
1837 19. Springstein, B.L., Nürnberg, D.J., Weiss, G.L., Pilhofer, M., and Stucken, K. (2020).
1838 Structural determinants and their role in cyanobacterial morphogenesis. Life *10*, 355.
1839 https://doi.org/https://doi.org/10.3390/life10120355.
1840 20. Velázquez-Suárez, C., Valladares, A., Luque, I., and Herrero, A. (2022). The Role of
1841 Mre Factors and Cell Division in Peptidoglycan Growth in the Multicellular
1842 Cyanobacterium Anabaena. MBio *13*. https://doi.org/10.1128/mbio.01165-22.
1843 21. Hu, B., Yang, G., Zhao, W., Zhang, Y., and Zhao, J. (2007). MreB is important for cell
1844 shape but not for chromosome segregation of the filamentous cyanobacterium
1845 Anabaena sp. PCC 7120. Mol. Microbiol. *63*, 1640–1652.
1846 https://doi.org/10.1111/j.1365-2958.2007.05618.x.

1847 22. Velázquez-Suárez, C., Luque, I., and Herrero, A. (2020). The Inorganic Nutrient
1848 Regime and the mre Genes Regulate Cell and Filament Size and Morphology in the
1849 Phototrophic Multicellular Bacterium Anabaena. mSphere *5*, e00747-20.
1850 https://doi.org/10.1128/mSphere.00747-20.
1851 23. Griese, M., Lange, C., and Soppa, J. (2011). Ploidy in cyanobacteria. FEMS Microbiol.
1852 Lett. *323*, 124–131. https://doi.org/10.1111/j.1574-6968.2011.02368.x.
1853 24. Schneider, D., Fuhrmann, E., Scholz, I., Hess, W.R., and Graumann, P.L. (2007).
1854 Fluorescence staining of live cyanobacterial cells suggest non-stringent chromosome
1855 segregation and absence of a connection between cytoplasmic and thylakoid
1856 membranes. BMC Cell Biol. *8*, 39. https://doi.org/10.1186/1471-2121-8-39.
1857 25. Sengupta, M., and Austin, S. (2011). Prevalence and significance of plasmid
1858 maintenance functions in the virulence plasmids of pathogenic bacteria. Infect. Immun.
1859 *79*, 2502–2509. https://doi.org/10.1128/IAI.00127-11.
1860 26. Jain, I.H., Vijayan, V., and O'Shea, E.K. (2012). Spatial ordering of chromosomes
1861 enhances the fidelity of chromosome partitioning in cyanobacteria. Proc. Natl. Acad.
1862 Sci. U. S. A. *109*, 13638–13643. https://doi.org/10.1073/pnas.1211144109.
1863 27. Ohbayashi, R., Nakamachi, A., Hatakeyama, T.S., Watanabe, S., Kanesaki, Y.,
1864 Chibazakura, T., Yoshikawa, H., and Miyagishima, S.Y. (2019). Coordination of
1865 polyploid chromosome replication with cell size and growth in a cyanobacterium. MBio
1866 *10*, 1–15. https://doi.org/10.1128/MBIO.00510-19.
1867 28. Watanabe, S., Noda, A., Ohbayashi, R., Uchioke, K., Kurihara, A., Nakatake, S.,
1868 Morioka, S., Kanesaki, Y., Chibazakura, T., and Yoshikawa, H. (2018). ParA-like
1869 protein influences the distribution of multi-copy chromosomes in cyanobacterium
1870 Synechococcus elongatus PCC 7942. Microbiology *164*, 45–56.
1871 https://doi.org/10.1099/mic.0.000577.
1872 29. Salje, J., Gayathri, P., and Löwe, J. (2010). The ParMRC system: Molecular
1873 mechanisms of plasmid segregation by actin-like filaments. Nat. Rev. Microbiol. *8*,
1874 683–692. https://doi.org/10.1038/nrmicro2425.

30. Gayathri, P., Fujii, T., Møller-Jensen, J., Van Den Ent, F., Namba, K., and Löwe, J. (2012). A bipolar spindle of antiparallel ParM filaments drives bacterial plasmid segregation. Science (80-.). *338*, 1334–1337. https://doi.org/10.1126/science.1229091.

31. Van den Ent, F., Møller-Jensen, J., Amos, L.A., Gerdes, K., and Löwe, J. (2002). F-actin-like filaments formed by plasmid segregation protein ParM. EMBO J. *21*, 6935–6943. https://doi.org/10.1093/emboj/cdf672.

32. Bharat, T.A.M., Murshudov, G.N., Sachse, C., and Löwe, J. (2015). Structures of actin-like ParM filaments show architecture of plasmid-segregating spindles. Nature *523*, 106–110. https://doi.org/10.1038/nature14356.

33. Møller-Jensen, J., Jensen, R.B., Löwe, J., and Gerdes, K. (2002). Prokaryotic DNA segregation by an actin-like filament. EMBO J. *21*, 3119–3127. https://doi.org/10.1093/emboj/cdf320.

34. Ali, S., Koh, A., Popp, D., Tanaka, K., Kitaoku, Y., Miyazaki, N., Iwasaki, K., Mitsuoka, K., Robinson, R.C., and Narita, A. (2025). Bacterial genome encoded ParMs. J. Biol. Chem., 110351.

35. Gerdes, K., Moller-Jensen, J., and Jensen, R.B. (2002). Plasmid and chromosome partitioning: Surprises from phylogeny. Mol. Microbiol. *37*, 455–466. https://doi.org/10.1046/j.1365-2958.2000.01975.x.

36. Møller-Jensen, J., Ringgaard, S., Mercogliano, C.P., Gerdes, K., and Löwe, J. (2007). Structural analysis of the ParR/parC plasmid partition complex. EMBO J. *26*, 4413–4422. https://doi.org/10.1038/sj.emboj.7601864.

37. Breüner, A., Jensen, R.B., Dam, M., Pedersen, S., and Gerdes, K. (1996). The centromere-like parC locus of plasmid R1. Mol. Microbiol. *20*, 581–592. https://doi.org/10.1046/j.1365-2958.1996.5351063.x.

38. Dam, M., and Gerdes, K. (1994). Partitioning of plasmid R1 Ten direct repeats flanking the parA promoter constitute a centromere-like partition site parC, that expresses incompatibility. J. Mol. Biol. *236*, 1289–1298. https://doi.org/10.1016/0022-

1903 2836(94)90058-2.
1904 39. Jiang, S., Narita, A., Popp, D., Ghoshdastider, U., Lee, L.J., Srinivasan, R.,
1905 Balasubramanian, M.K., Oda, T., Koh, F., Larsson, M., et al. (2016). Novel actin
1906 filaments from Bacillus thuringiensis form nanotubules for plasmid DNA segregation.
1907 Proc. Natl. Acad. Sci. U. S. A. *113*, E1200–E1205.
1908 https://doi.org/10.1073/pnas.1600129113.
1909 40. Brzoska, A.J., Jensen, S.O., Barton, D.A., Davies, D.S., Overall, R.L., Skurray, R.A.,
1910 and Firth, N. (2016). Dynamic filament formation by a divergent bacterial actin-like
1911 ParM protein. PLoS One *11*, 1–14. https://doi.org/10.1371/journal.pone.0156944.
1912 41. Schreiter, E.R., and Drennan, C.L. (2007). Ribbon-helix-helix transcription factors:
1913 Variations on a theme. Nat. Rev. Microbiol. *5*, 710–720.
1914 https://doi.org/10.1038/nrmicro1717.
1915 42. Salje, J., and Löwe, J. (2008). Bacterial actin: Architecture of the ParMRC plasmid
1916 DNA partitioning complex. EMBO J. *27*, 2230–2238.
1917 https://doi.org/10.1038/emboj.2008.152.
1918 43. Orlova, A., Garner, E.C., Galkin, V.E., Heuser, J., Mullins, R.D., and Egelman, E.H.
1919 (2007). The structure of bacterial ParM filaments. Nat. Struct. Mol. Biol. *14*, 921–926.
1920 https://doi.org/10.1038/nsmb1300.
1921 44. Lee, P.S., and Grossman, A.D. (2006). The chromosome partitioning proteins Soj
1922 (ParA) and Spo0J (ParB) contribute to accurate chromosome partitioning, separation
1923 of replicated sister origins, and regulation of replication initiation in Bacillus subtilis.
1924 Mol. Microbiol. *60*, 853–869. https://doi.org/10.1111/j.1365-2958.2006.05140.x.
1925 45. Mohl, D.A., and Gober, J.W. (1997). Cell Cycle–Dependent Polar Localization of
1926 Chromosome Partitioning Proteins in Caulobacter crescentus. Cell *88*, 675–684.
1927 https://doi.org/10.1016/s0092-8674(00)81910-8.
1928 46. Niki, H., Ogura, T., Ichinose, C., Mori, H., Ezaki, B., and Jaffe, A. (1989). Chromosome
1929 partitioning in Escherichia coli: novel mutants producing anucleate cells. J. Bacteriol.
1930 *171*, 1496–1505.

1931 47. Ungerer, J., and Pakrasi, H.B. (2016). Cpf1 Is A Versatile Tool for CRISPR Genome
1932 Editing Across Diverse Species of Cyanobacteria. Sci. Rep. *6*, 1–9.
1933 https://doi.org/10.1038/srep39681.
1934 48. Campbell, C.S., and Mullins, R.D. (2007). In vivo visualization of type II plasmid
1935 segregation: Bacterial actin filaments pushing plasmids. J. Cell Biol. *179*, 1059–1066.
1936 https://doi.org/10.1083/jcb.200708206.
1937 49. Garner, E.C., Campbell, C.S., and Dyce Mullins, R. (2004). Dynamic Instability in a
1938 DNA-Segregating Prokaryotic Actin Homolog. Science (80-.). *306*, 1021–1025.
1939 50. Garner, E.C., Campbell, C.S., Weibel, D.B., and Mullins, R.D. (2007). Reconstitution
1940 of DNA Segregation Driven by Assembly of a Prokaryotic Actin Homolog. Science (80-
1941 .). *315*, 1270–1274.
1942 51. Sapay, N., Guermeur, Y., and Deléage, G. (2006). Prediction of amphipathic in-plane
1943 membrane anchors in monotopic proteins using a SVM classifier. BMC Bioinformatics
1944 *7*, 1–11. https://doi.org/10.1186/1471-2105-7-255.
1945 52. Krissinel, E., and Henrick, K. (2007). Inference of Macromolecular Assemblies from
1946 Crystalline State. J. Mol. Biol. *372*, 774–797.
1947 https://doi.org/https://doi.org/10.1016/j.jmb.2007.05.022.
1948 53. Evans, R., O'Neill, M., Pritzel, A., Antropova, N., Senior, A., Green, T., Žídek, A.,
1949 Bates, R., Blackwell, S., Yim, J., et al. (2022). Protein complex prediction with
1950 AlphaFold-Multimer. bioRxiv, 2021.10.04.463034.
1951 https://doi.org/10.1101/2021.10.04.463034.
1952 54. Jumper, J., Evans, R., Pritzel, A., Green, T., Figurnov, M., Ronneberger, O.,
1953 Tunyasuvunakool, K., Bates, R., Žídek, A., Potapenko, A., et al. (2021). Highly
1954 accurate protein structure prediction with AlphaFold. Nature *596*, 583–589.
1955 https://doi.org/10.1038/s41586-021-03819-2.
1956 55. de Boer, P.A.J., Crossley, R.E., and Rothfield, L.I. (1989). A division inhibitor and a
1957 topological specificity factor coded for by the minicell locus determine proper
1958 placement of the division septum in E. coli. Cell *56*, 641–649.

https://doi.org/10.1016/0092-8674(89)90586-2.

56. Hu, Z., and Lutkenhaus, J. (1999). Topological regulation of cell division in Escherichia coli involves rapid pole to pole oscillation of the division inhibitor MinC under the control of MinD and MinE. Mol. Microbiol. *34*, 82–90. https://doi.org/https://doi.org/10.1046/j.1365-2958.1999.01575.x.

57. Raskin, D.M., and De Boer, P.A.J. (1999). Rapid pole-to-pole oscillation of a protein required for directing division to the middle of Escherichia coli. Proc. Natl. Acad. Sci. *96*, 4971–4976.

58. Pollard, T.D. (2016). Actin and actin-binding proteins. Cold Spring Harb. Perspect. Biol. *8*, 1–17. https://doi.org/10.1101/cshperspect.a018226.

59. Xue, B., Leyrat, C., Grimes, J.M., and Robinson, R.C. (2014). Structural basis of thymosin-β4/profilin exchange leading to actin filament polymerization. Proc. Natl. Acad. Sci. U. S. A. *111*, E4596–E4605. https://doi.org/10.1073/pnas.1412271111.

60. Palmgren, S., Vartiainen, M., and Lappalainen, P. (2002). Twinfilin, a molecular mailman for actin monomers. J. Cell Sci. *115*, 881–886. https://doi.org/10.1242/jcs.115.5.881.

61. Curmi, P.A., Andersen, S.S.L., Lachkar, S., Gavet, O., Karsenti, E., Knossow, M., and Sobel, A. (1997). The stathmin/tubulin interaction in vitro. J. Biol. Chem. *272*, 25029–25036. https://doi.org/10.1074/jbc.272.40.25029.

62. Hu, Z., Mukherjee, A., Pichoff, S., and Lutkenhaus, J. (1999). The MinC component of the division site selection system in Escherichia coli interacts with FtsZ to prevent polymerization. Proc. Natl. Acad. Sci. U. S. A. *96*, 14819–14824. https://doi.org/10.1073/pnas.96.26.14819.

63. Paredez, A.R., Somerville, C.R., and Ehrhardt, D.W. (2006). Visualization of Cellulose Synthase Demonstrates Functional Association with Microtubules. Science (80-.). *312*, 1491–1495. https://doi.org/10.1126/science.1126551.

64. Sugimoto, K., Williamson, R.E., and Wasteneys, G.O. (2000). New techniques enable comparative analysis of microtubule orientation, wall texture, and growth rate in intact

1987 roots of Arabidopsis. Plant Physiol. *124*, 1493–1506.
1988 https://doi.org/10.1104/pp.124.4.1493.
1989 65. Paredez, A.R., Persson, S., Ehrhardt, D.W., and Somerville, C.R. (2008). Genetic
1990 evidence that cellulose synthase activity influences microtubule cortical array
1991 organization. Plant Physiol. *147*, 1723–1734. https://doi.org/10.1104/pp.108.120196.
1992 66. Savage, D.F., Afonso, B., Chen, A.H., and Silver, P.A. (2010). Spatially Ordered
1993 Dynamics of the Bacterial Carbon Fixation Machinery. Science (80-.). *327*, 1258–
1994 1261. https://doi.org/10.1126/science.1186090.
1995 67. Wachi, M., Doi, M., Tamaki, S., Park, W., Nakajima-Iijima, S., and Matsuhashi, M.
1996 (1987). Mutant isolation and molecular cloning of mre genes, which determine cell
1997 shape, sensitivity to mecillinam, and amount of penicillin-binding proteins in
1998 Escherichia coli. J. Bacteriol. *169*, 4935–4940.
1999 68. Shi, H., Bratton, B.P., Gitai, Z., and Huang, K.C. (2018). How to Build a Bacterial Cell:
2000 MreB as the Foreman of E. coli Construction. Cell *172*, 1294–1305.
2001 https://doi.org/10.1016/j.cell.2018.02.050.
2002 69. van den Ent, F., Izoré, T., Bharat, T.A.M., Johnson, C.M., and Löwe, J. (2014).
2003 Bacterial actin MreB forms antiparallel double filaments. Elife *2014*, 1–22.
2004 https://doi.org/10.7554/eLife.02634.
2005 70. van Teeffelen, S., Wang, S., Furchtgott, L., Huang, K.C., Wingreen, N.S., Shaevitz,
2006 J.W., and Gitai, Z. (2011). The bacterial actin MreB rotates, and rotation depends on
2007 cell-wall assembly. Proc. Natl. Acad. Sci. *108*, 15822 LP – 15827.
2008 https://doi.org/10.1073/pnas.1108999108.
2009 71. Mukherjee, A., and Lutkenhaus, J. (1998). Dynamic assembly of FtsZ regulated by
2010 GTP hydrolysis. EMBO J. *17*, 462–469. https://doi.org/10.1093/emboj/17.2.462.
2011 72. Carlier, M.F., Pantaloni, D., and Korn, E.D. (1984). Evidence for an ATP cap at the
2012 ends of actin filaments and its regulation of the F-actin steady state. J. Biol. Chem.
2013 *259*, 9983–9986. https://doi.org/10.1016/s0021-9258(18)90914-2.
2014 73. Mitchison, T., and Kirschner, M. (1984). Dynamic instability of microtubule growth.

Nature *312*, 237–242.

74. Rubio, M.Á., Napolitano, M., Ochoa De Alda, J.A.G., Santamaría-Gómez, J., Patterson, C.J., Foster, A.W., Bru-Martínez, R., Robinson, N.J., and Luque, I. (2015). Trans-oligomerization of duplicated aminoacyl-tRNA synthetases maintains genetic code fidelity under stress. Nucleic Acids Res. *43*, 9905–9917. https://doi.org/10.1093/nar/gkv1020.

75. Abramson, J., Adler, J., Dunger, J., Evans, R., Green, T., Pritzel, A., Ronneberger, O., Willmore, L., Ballard, A.J., Bambrick, J., et al. (2024). Accurate structure prediction of biomolecular interactions with AlphaFold 3. Nature *630*, 493–500. https://doi.org/10.1038/s41586-024-07487-w.

76. Meng, E.C., Goddard, T.D., Pettersen, E.F., Couch, G.S., Pearson, Z.J., Morris, J.H., and Ferrin, T.E. (2023). UCSF ChimeraX: Tools for structure building and analysis. Protein Sci. *32*, e4792. https://doi.org/https://doi.org/10.1002/pro.4792.

77. Vega-Palas, M.A., Flores, E., and Herrero, A. (1992). NtcA, a global nitrogen regulator from the cyanobacterium Synechococcus that belongs to the Crp family of bacterial regulators. Mol. Microbiol. *6*, 1853–1859. https://doi.org/https://doi.org/10.1111/j.1365-2958.1992.tb01357.x.

78. Crooks, G.E., Hon, G., Chandonia, J.-M., and Brenner, S.E. (2004). WebLogo: a sequence logo generator. Genome Res. *14*, 1188–1190.

79. Sun, C., Gonzalez, B., and Jiang, W. (2022). Helical indexing in real space. Sci. Rep. *12*, 8162.

80. Corrales-Guerrero, L., Camargo, S., Valladares, A., Picossi, S., Luque, I., Ochoa De Alda, J.A.G., and Herrero, A. (2018). FtsZ of filamentous, heterocyst-forming cyanobacteria has a conserved N-terminal peptide required for normal FtsZ polymerization and cell division. Front. Microbiol. *9*, 1–20. https://doi.org/10.3389/fmicb.2018.02260.

81. Valladares, A., Picossi, S., Corrales-Guerrero, L., and Herrero, A. (2023). The role of SepF in cell division and diazotrophic growth in the multicellular cyanobacterium

Anabaena sp. strain PCC 7120. Microbiol. Res. *277*, 127489. https://doi.org/10.1016/j.micres.2023.127489.

82. Karimova, G., Davi, M., and Ladant, D. (2012). The β-lactam resistance protein Blr, a small membrane polypeptide, is a component of the Escherichia coli cell division machinery. J. Bacteriol. *194*, 5576–5588. https://doi.org/10.1128/JB.00774-12.

83. Kartasalo, K., Pölönen, R.P., Ojala, M., Rasku, J., Lekkala, J., Aalto-Setälä, K., and Kallio, P. (2015). CytoSpectre: A tool for spectral analysis of oriented structures on cellular and subcellular levels. BMC Bioinformatics *16*, 1–23. https://doi.org/10.1186/s12859-015-0782-y.

84. Croll, T.I. (2018). ISOLDE: a physically realistic environment for model building into low-resolution electron-density maps. Biol. Crystallogr. *74*, 519–530.

85. Williams, C.J., Headd, J.J., Moriarty, N.W., Prisant, M.G., Videau, L.L., Deis, L.N., Verma, V., Keedy, D.A., Hintze, B.J., and Chen, V.B. (2018). MolProbity: more and better reference data for improved all-atom structure validation. Protein Sci. *27*, 293–315.

86. Sayers, E.W., Bolton, E.E., Brister, J.R., Canese, K., Chan, J., Comeau, D.C., Farrell, C.M., Feldgarden, M., Fine, A.M., Funk, K., et al. (2023). Database resources of the National Center for Biotechnology Information in 2023. Nucleic Acids Res. *51*, D29–D38. https://doi.org/10.1093/nar/gkac1032.

87. Eddy, S.R. (2011). Accelerated Profile HMM Searches. PLOS Comput. Biol. *7*, e1002195.

88. Katoh, K., and Standley, D.M. (2013). MAFFT multiple sequence alignment software version 7: Improvements in performance and usability. Mol. Biol. Evol. *30*, 772–780. https://doi.org/10.1093/molbev/mst010.

89. Goldfarb, T., Kodali, V.K., Pujar, S., Brover, V., Robbertse, B., Farrell, C.M., Oh, D.-H., Astashyn, A., Ermolaeva, O., Haddad, D., et al. (2025). NCBI RefSeq: reference sequence standards through 25 years of curation and annotation. Nucleic Acids Res. *53*, D243–D257. https://doi.org/10.1093/nar/gkae1038.

90. Megrian, D., Taib, N., Jaffe, A.L., Banfield, J.F., and Gribaldo, S. (2022). Ancient origin and constrained evolution of the division and cell wall gene cluster in Bacteria. Nat. Microbiol. *7*, 2114–2127. https://doi.org/10.1038/s41564-022-01257-y.

91. AR, M., MS, C., and W, F. (2024). NetWheels: A Web Application to Create High Quality Peptide Helical Wheel and Net Projections. J. Bioinforma. Syst. Biol. *7*, 98–100. https://doi.org/10.26502/jbsb.5107082.

92. Van Hilten, N., Verwei, N., Methorst, J., Nase, C., Bernatavicius, A., and Risselada, H.J. (2024). PMIpred: a physics-informed web server for quantitative protein-membrane interaction prediction. Bioinformatics *40*, 1–10. https://doi.org/10.1093/bioinformatics/btae069.

93. Capella-Gutiérrez, S., Silla-Martínez, J.M., and Gabaldón, T. (2009). trimAl: a tool for automated alignment trimming in large-scale phylogenetic analyses. Bioinformatics *25*, 1972–1973. https://doi.org/10.1093/bioinformatics/btp348.

94. Waterhouse, A.M., Procter, J.B., Martin, D.M.A., Clamp, M., and Barton, G.J. (2009). Jalview Version 2—a multiple sequence alignment editor and analysis workbench. Bioinformatics *25*, 1189–1191. https://doi.org/10.1093/bioinformatics/btp033.

95. Pettersen, E.F., Goddard, T.D., Huang, C.C., Meng, E.C., Couch, G.S., Croll, T.I., Morris, J.H., and Ferrin, T.E. (2021). UCSF ChimeraX: Structure visualization for researchers, educators, and developers. Protein Sci. *30*, 70–82. https://doi.org/https://doi.org/10.1002/pro.3943.

96. Pei, J., and Grishin, N. V (2001). AL2CO: calculation of positional conservation in a protein sequence alignment. Bioinformatics *17*, 700–712. https://doi.org/10.1093/bioinformatics/17.8.700.

97. Minh, B.Q., Schmidt, H.A., Chernomor, O., Schrempf, D., Woodhams, M.D., von Haeseler, A., and Lanfear, R. (2020). IQ-TREE 2: New Models and Efficient Methods for Phylogenetic Inference in the Genomic Era. Mol. Biol. Evol. *37*, 1530–1534. https://doi.org/10.1093/molbev/msaa015.

98. Kalyaanamoorthy, S., Minh, B.Q., Wong, T.K.F., von Haeseler, A., and Jermiin, L.S.

(2017). ModelFinder: fast model selection for accurate phylogenetic estimates. Nat. Methods *14*, 587–589. https://doi.org/10.1038/nmeth.4285.

99. Hoang, D.T., Chernomor, O., von Haeseler, A., Minh, B.Q., and Vinh, L.S. (2018). UFBoot2: Improving the Ultrafast Bootstrap Approximation. Mol. Biol. Evol. *35*, 518–522. https://doi.org/10.1093/molbev/msx281.

100. Letunic, I., and Bork, P. (2021). Interactive Tree Of Life (iTOL) v5: an online tool for phylogenetic tree display and annotation. Nucleic Acids Res. *49*, W293–W296. https://doi.org/10.1093/nar/gkab301.

101. Schindelin, J., Arganda-Carreras, I., Frise, E., Kaynig, V., Longair, M., Pietzsch, T., Preibisch, S., Rueden, C., Saalfeld, S., Schmid, B., et al. (2012). Fiji: An open-source platform for biological-image analysis, https://doi.org/10.1038/nmeth.2019 https://doi.org/10.1038/nmeth.2019.

102. Lotthammer, J.M., Ginell, G.M., Griffith, D., Emenecker, R.J., and Holehouse, A.S. (2024). Direct prediction of intrinsically disordered protein conformational properties from sequence. Nat. Methods *21*, 465–476. https://doi.org/10.1038/s41592-023-02159-5.

Figure 1

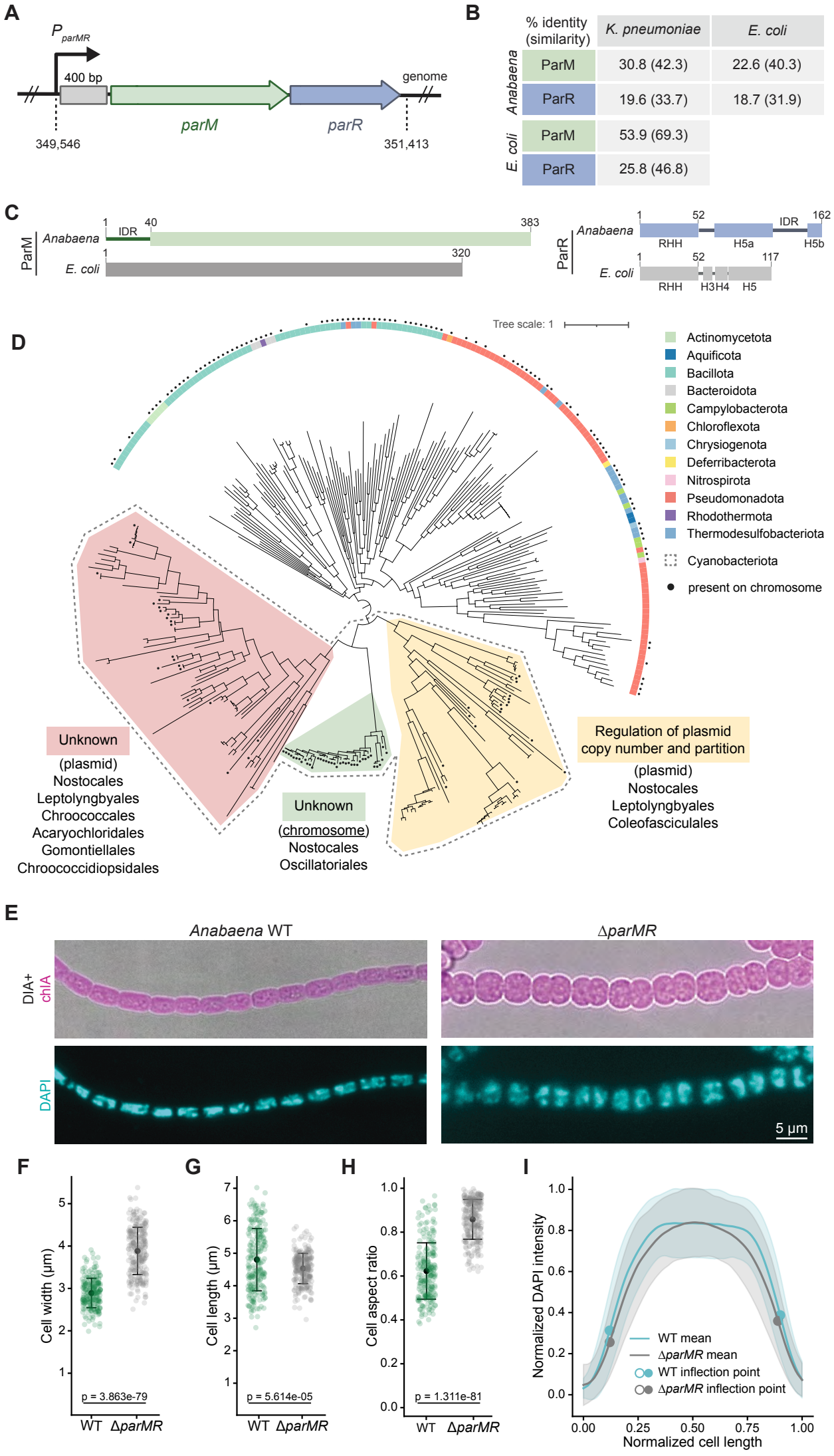
A
P_{parMR}
400 bp
genome
parM
parR
349,546
351,413
B
% identity (similarity)
K. pneumoniae
E. coli
Anabaena
ParM 30.8 (42.3) 22.6 (40.3)
ParR 19.6 (33.7) 18.7 (31.9)
E. coli
ParM 53.9 (69.3)
ParR 25.8 (46.8)
C
ParM
Anabaena
IDR
1
40
383
E. coli
1
320
ParR
Anabaena
1
52
IDR
162
RHH
H5a
H5b
E. coli
1
52
117
RHH
H3H4
H5
D
Tree scale: 1
Actinomycetota
Aquificota
Bacillota
Bacteroidota
Campylobacterota
Chloroflexota
Chrysiogenota
Deferribacterota
Nitrospirota
Pseudomonadota
Rhodothermota
Thermodesulfobacteriota
Cyanobacteriota
present on chromosome
Unknown
(plasmid)
Nostocales
Leptolyngbyales
Chroococcales
Acaryochloridales
Gomontiellales
Chroococcidiopsidales
Unknown
(chromosome)
Nostocales
Oscillatoriales
Regulation of plasmid copy number and partition
(plasmid)
Nostocales
Leptolyngbyales
Coleofasciculales
E
Anabaena WT
ΔparMR
DIA+ chlA
DAPI
5 µm
F
Cell width (µm)
p = 3.863e-79
WT
ΔparMR
G
Cell length (µm)
p = 5.614e-05
WT
ΔparMR
H
Cell aspect ratio
p = 1.311e-81
WT
ΔparMR
I
Normalized DAPI intensity
WT mean
ΔparMR mean
WT inflection point
ΔparMR inflection point
Normalized cell length

Figure 2

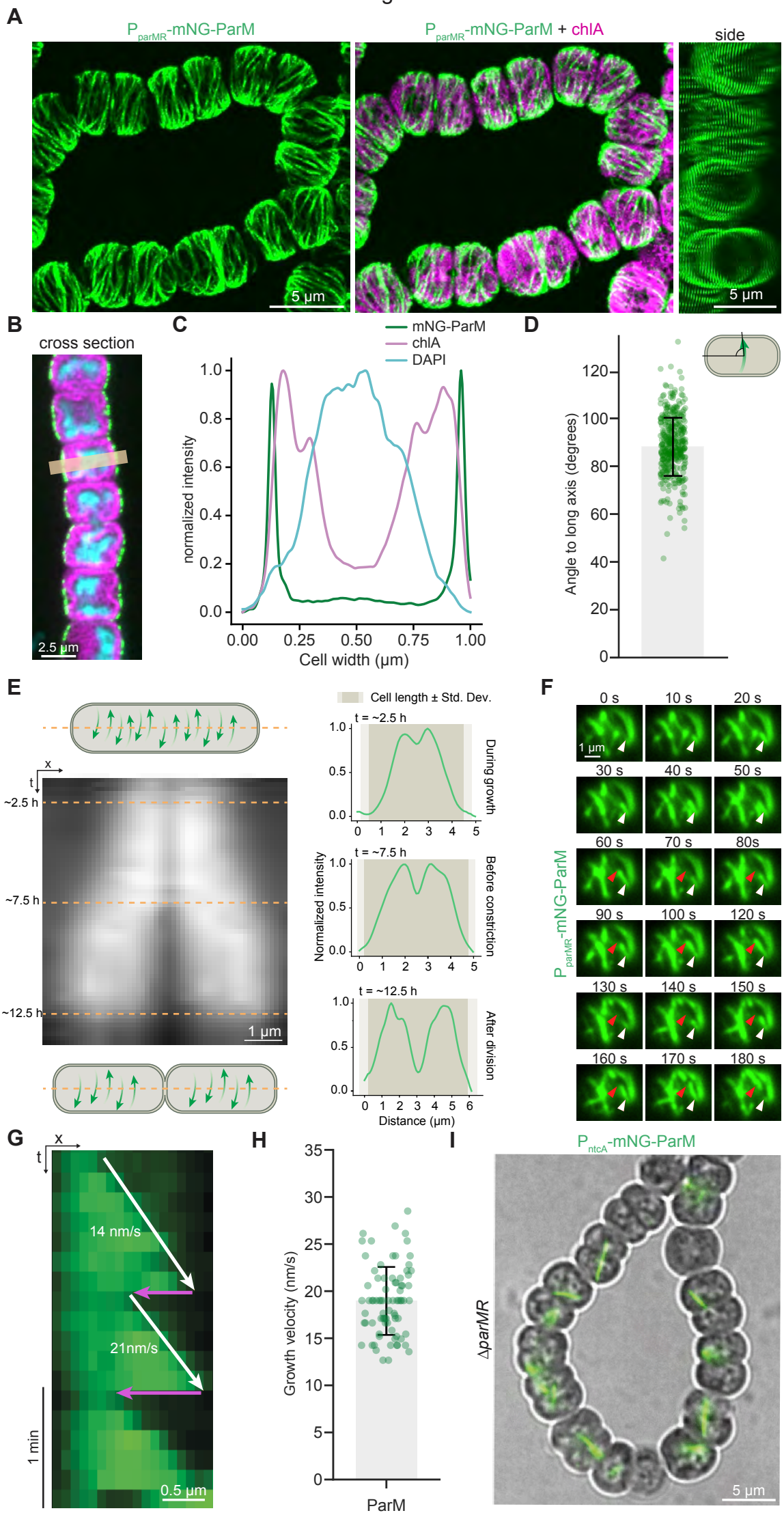
A
P parMR -mNG-ParM
P parMR -mNG-ParM + chlA
side
5 µm
5 µm
B
cross section
2.5 µm
C
mNG-ParM
chlA
DAPI
normalized intensity
Cell width (µm)
D
Angle to long axis (degrees)
E
Cell length ± Std. Dev.
t = ~2.5 h
During growth
t = ~7.5 h
Before constriction
t = ~12.5 h
After division
Normalized intensity
Distance (µm)
~2.5 h
~7.5 h
~12.5 h
1 µm
F
0 s
10 s
20 s
30 s
40 s
50 s
60 s
70 s
80s
90 s
100 s
120 s
130 s
140 s
150 s
160 s
170 s
180 s
1 µm
P parMR -mNG-ParM
G
14 nm/s
21nm/s
1 min
0.5 µm
H
Growth velocity (nm/s)
ParM
I
P ntcA -mNG-ParM
ΔparMR
5 µm

Figure 3

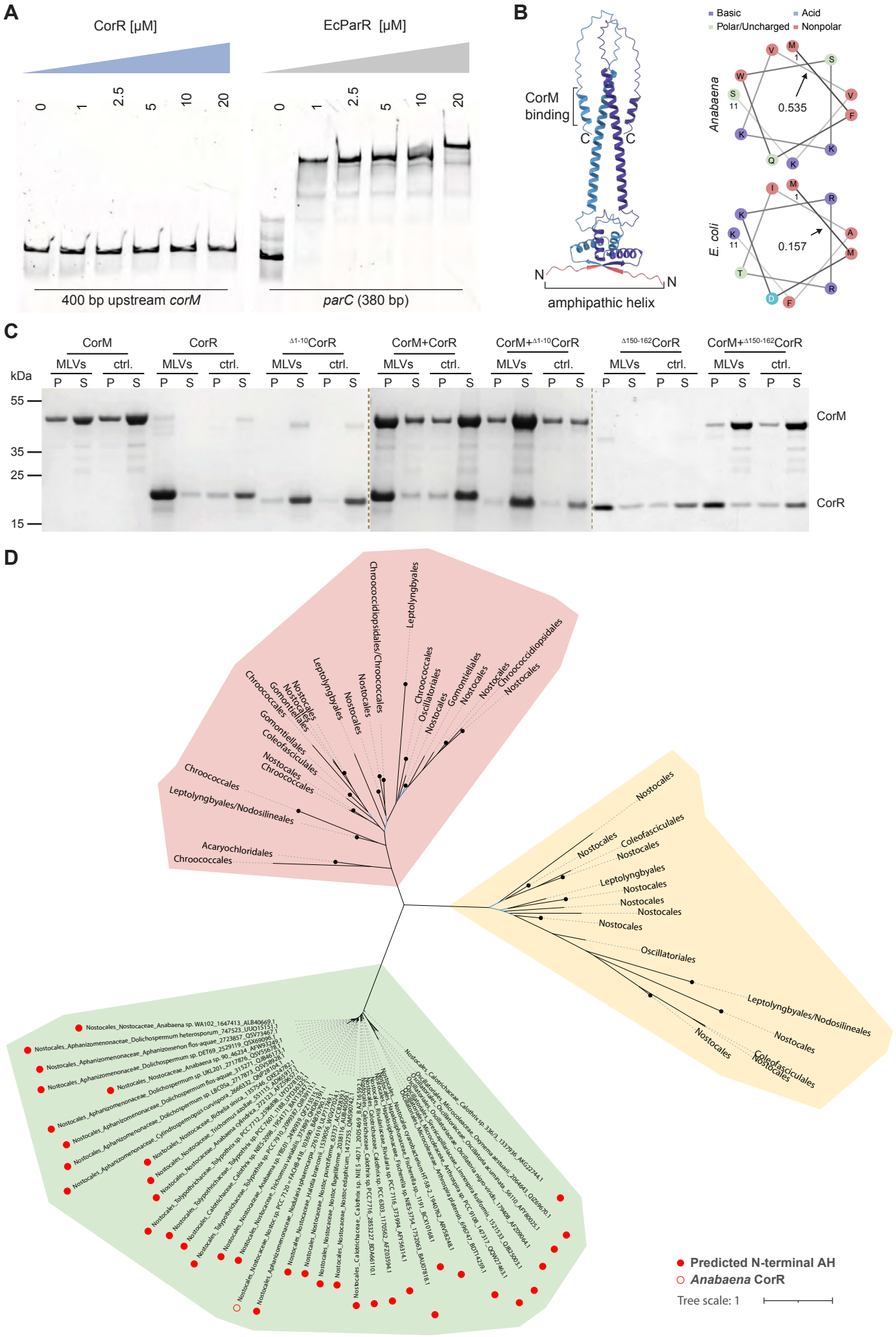
A
CorR [μM]
EcParR [μM]
0
1
2.5
5
10
20
400 bp upstream corM
parC (380 bp)
B
CorM binding
C
C
N
N
amphipathic helix
Basic
Acid
Polar/Uncharged
Nonpolar
Anabaena
0.535
E. coli
0.157
C
CorM
CorR
Δ1-10CorR
CorM+CorR
CorM+Δ1-10CorR
Δ150-162CorR
CorM+Δ150-162CorR
MLVs
ctrl.
P
S
kDa
55
35
25
15
CorM
CorR
D
Chroococcidiopsidales/Chroococcales
Leptolyngbyales
Chroococcales
Oscillatoriales
Nostocales
Gomontiellales
Chroococcidiopsidales
Coleofasciculales
Leptolyngbyales/Nodosilineales
Acaryochloridales
Predicted N-terminal AH
Anabaena CorR
Tree scale: 1

Figure 4

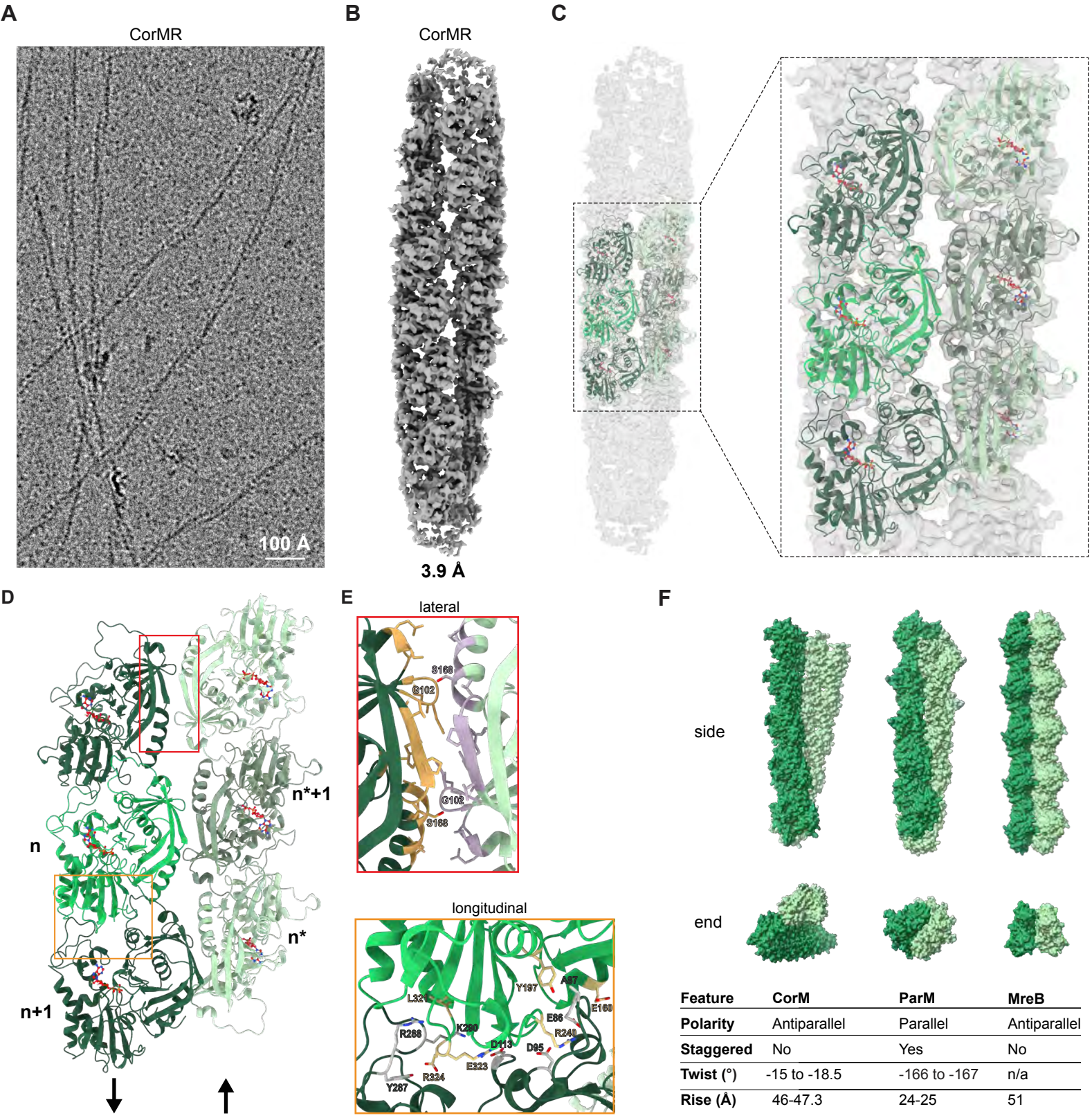

Feature	CorM	ParM	MreB
Polarity	Antiparallel	Parallel	Antiparallel
Staggered	No	Yes	No
Twist (°)	-15 to -18.5	-166 to -167	n/a
Rise (Å)	46-47.3	24-25	51

Figure 5

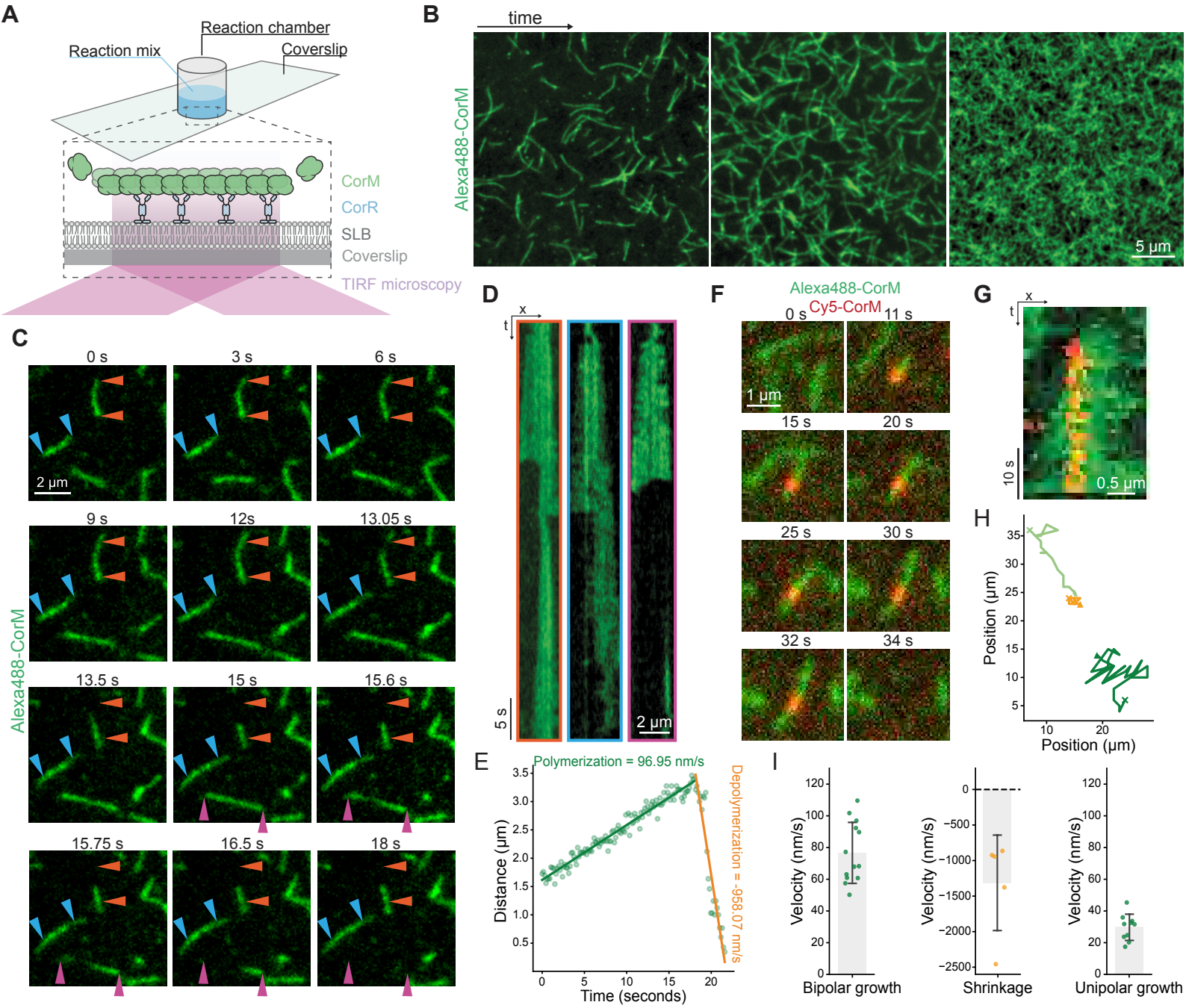
A
Reaction chamber
Reaction mix
Coverslip
CorM
CorR
SLB
Coverslip
TIRF microscopy
B
time
Alexa488-CorM
5 µm
C
0 s
3 s
6 s
2 µm
9 s
12s
13.05 s
13.5 s
15 s
15.6 s
15.75 s
16.5 s
18 s
Alexa488-CorM
D
x
t
5 s
2 µm
E
Polymerization = 96.95 nm/s
Depolymerization = -958.07 nm/s
Distance (µm)
Time (seconds)
F
Alexa488-CorM
Cy5-CorM
0 s
11 s
1 µm
15 s
20 s
25 s
30 s
32 s
34 s
G
x
t
10 s
0.5 µm
H
Position (µm)
Position (µm)
I
Velocity (nm/s)
Bipolar growth
Velocity (nm/s)
Shrinkage
Velocity (nm/s)
Unipolar growth

Figure 6

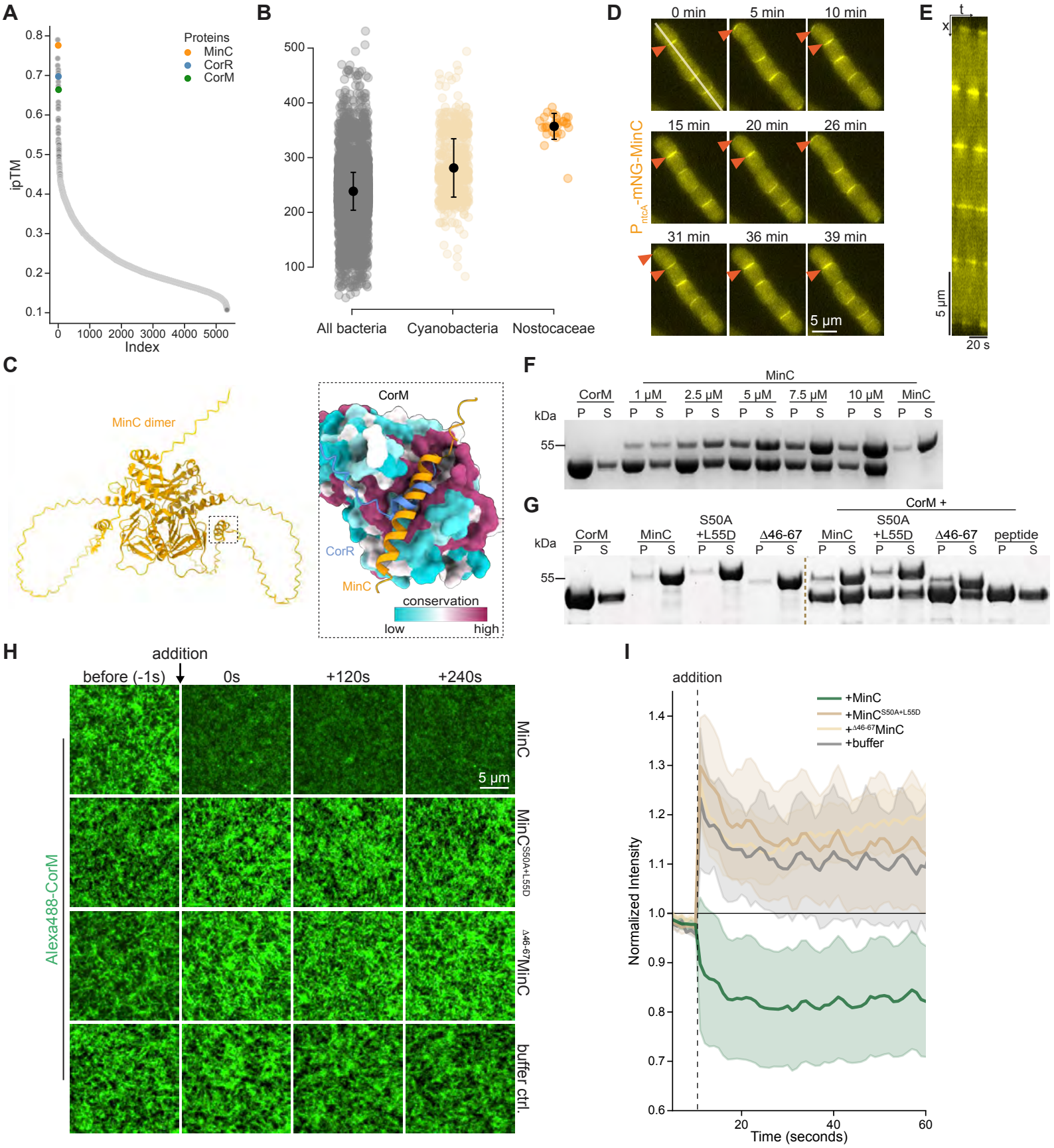
A
Proteins
MinC
CorR
CorM
ipTM
Index
B
All bacteria
Cyanobacteria
Nostocaceae
C
MinC dimer
CorM
CorR
MinC
conservation
low
high
D
0 min
5 min
10 min
15 min
20 min
26 min
31 min
36 min
39 min
5 µm
P ntcA-mNG-MinC
E
t
x
5 µm
20 s
F
MinC
CorM
1 µM
2.5 µM
5 µM
7.5 µM
10 µM
MinC
kDa
55
P S
G
CorM
MinC
S50A +L55D
Δ46-67
CorM +
MinC
S50A +L55D
Δ46-67
peptide
kDa
55
H
addition
before (-1s)
0s
+120s
+240s
Alexa488-CorM
MinC
MinC S50A+L55D
Δ46-67 MinC
buffer ctrl.
5 µm
I
addition
+MinC
+MinC S50A+L55D
+Δ46-67 MinC
+buffer
Normalized Intensity
Time (seconds)

Figure 7

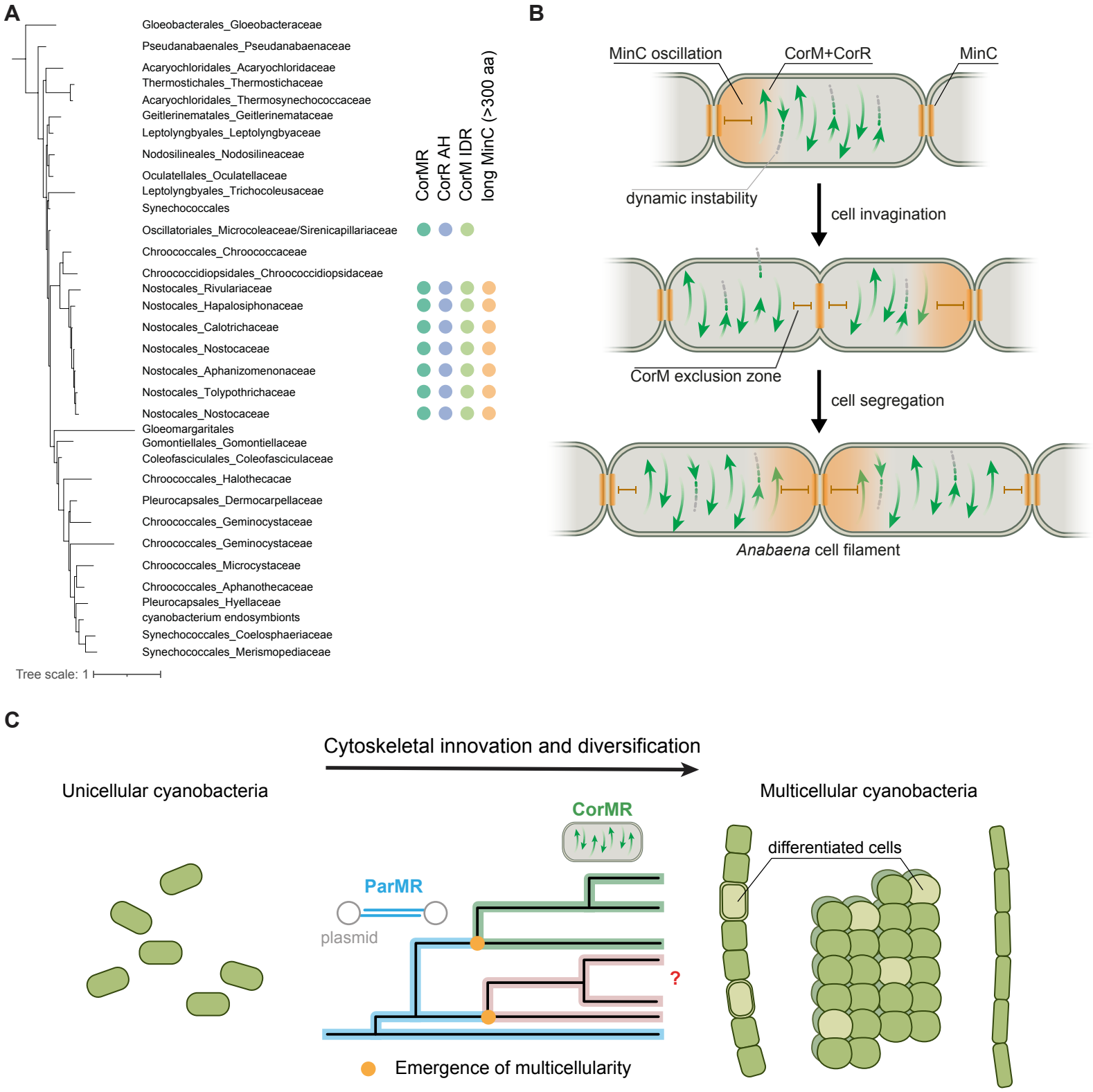
A
Gloeobacterales_Gloeobacteraceae
Pseudanabaenales_Pseudanabaenaceae
Acaryochloridales_Acaryochloridaceae
Thermostichales_Thermostichaceae
Acaryochloridales_Thermosynechococcaceae
Geitlerinematales_Geitlerinemataceae
Leptolyngbyales_Leptolyngbyaceae
Nodosilineales_Nodosilineaceae
Oculatellales_Oculatellaceae
Leptolyngbyales_Trichocoleusaceae
Synechococcales
Oscillatoriales_Microcoleaceae/Sirenicapillariaceae
Chroococcales_Chroococcaceae
Chroococcidiopsidales_Chroococcidiopsidaceae
Nostocales_Rivulariaceae
Nostocales_Hapalosiphonaceae
Nostocales_Calotrichaceae
Nostocales_Nostocaceae
Nostocales_Aphanizomenonaceae
Nostocales_Tolypothrichaceae
Nostocales_Nostocaceae
Gloeomargaritales
Gomontiellales_Gomontiellaceae
Coleofasciculales_Coleofasciculaceae
Chroococcales_Halothecacae
Pleurocapsales_Dermocarpellaceae
Chroococcales_Geminocystaceae
Chroococcales_Geminocystaceae
Chroococcales_Microcystaceae
Chroococcales_Aphanothecaceae
Pleurocapsales_Hyellaceae
cyanobacterium endosymbionts
Synechococcales_Coelosphaeriaceae
Synechococcales_Merismopediaceae
Tree scale: 1
CorMR
CorR AH
CorM IDR
long MinC (>300 aa)
B
MinC oscillation
CorM+CorR
MinC
dynamic instability
cell invagination
CorM exclusion zone
cell segregation
Anabaena cell filament
C
Cytoskeletal innovation and diversification
Unicellular cyanobacteria
Multicellular cyanobacteria
CorMR
ParMR
plasmid
?
differentiated cells
Emergence of multicellularity

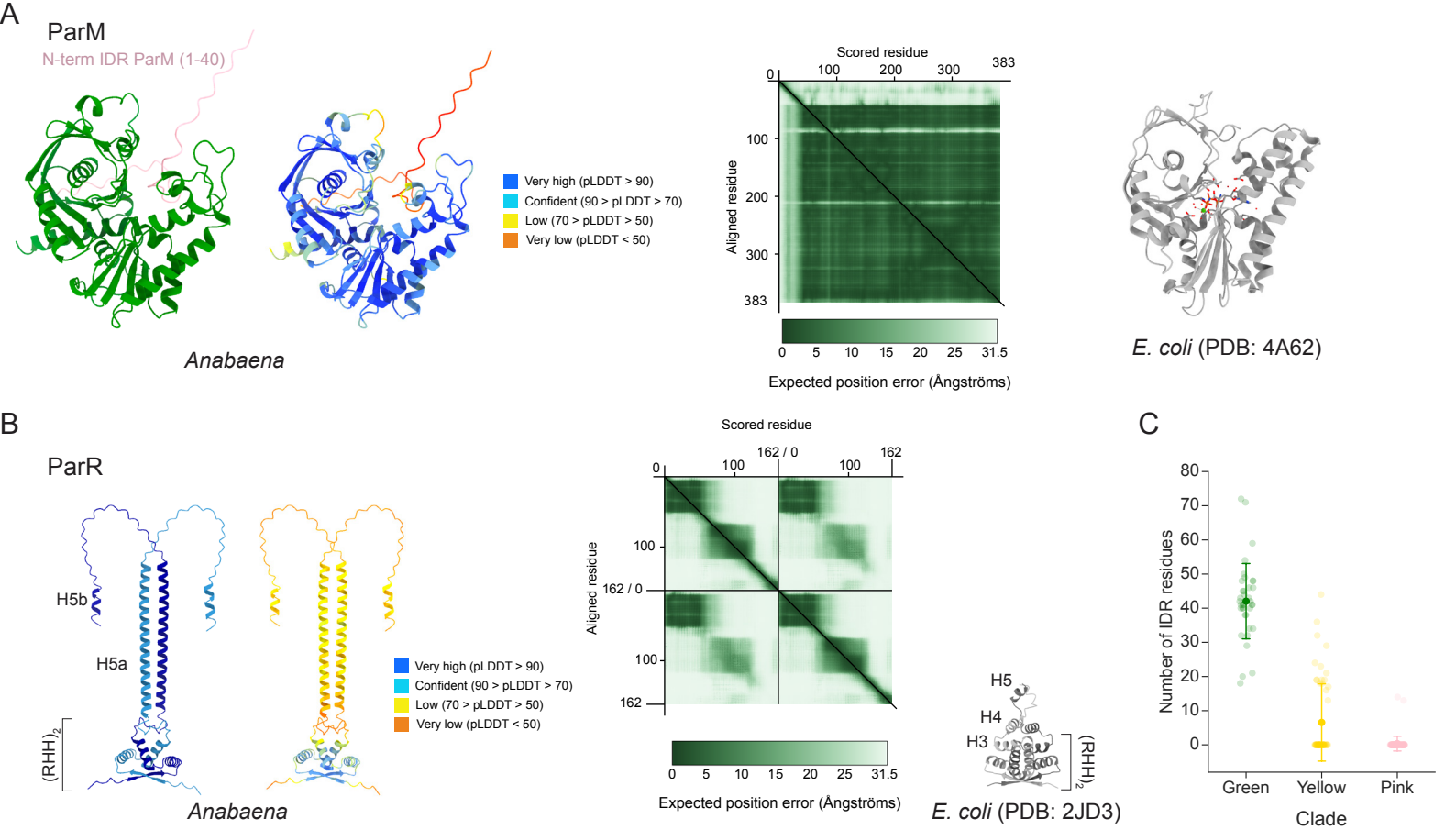
A
ParM
N-term IDR ParM (1-40)
Very high (pLDDT > 90)
Confident (90 > pLDDT > 70)
Low (70 > pLDDT > 50)
Very low (pLDDT < 50)
Anabaena
Scored residue
Aligned residue
Expected position error (Ångströms)
E. coli (PDB: 4A62)
B
ParR
H5b
H5a
(RHH)2
Anabaena
H5
H4
H3
E. coli (PDB: 2JD3)
C
Number of IDR residues
Green
Yellow
Pink
Clade

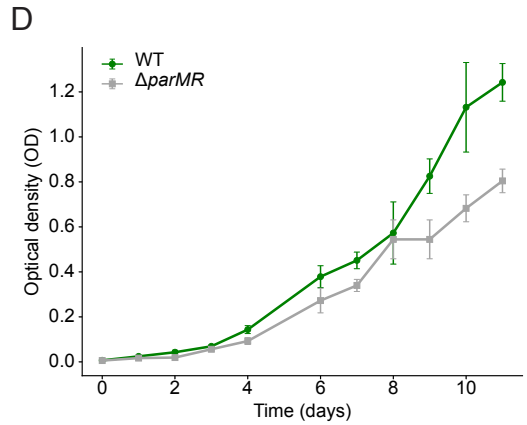
D
WT
ΔparMR
Optical density (OD)
Time (days)

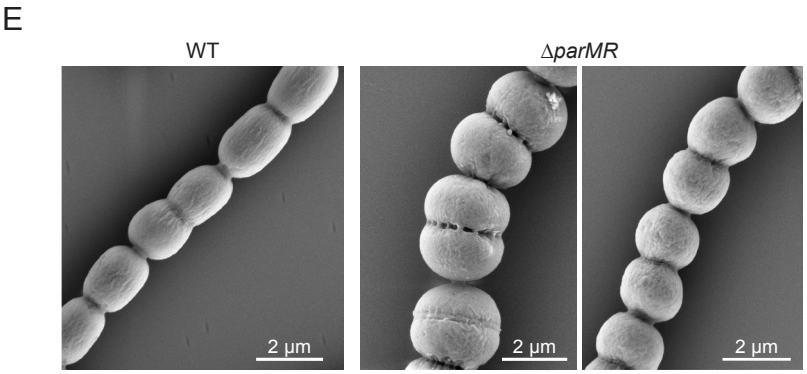
E
WT
ΔparMR
2 µm
2 µm
2 µm

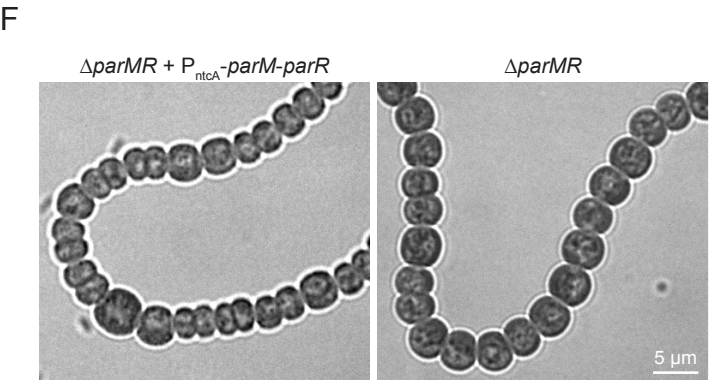
F
ΔparMR + PntcA-parM-parR
ΔparMR
5 µm

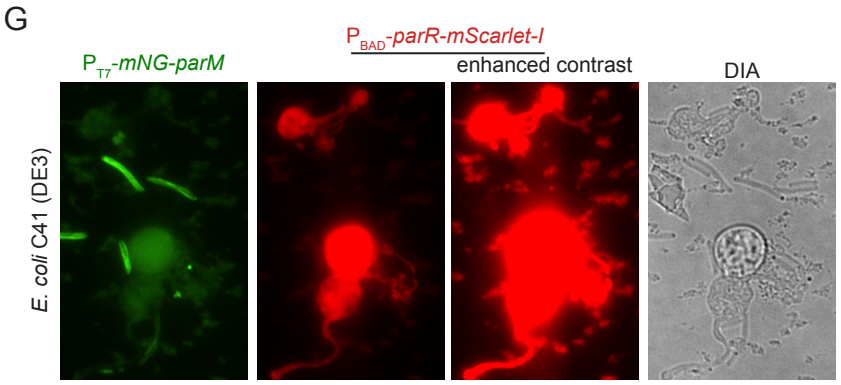
G
PT7-mNG-parM
PBAD-parR-mScarlet-I
enhanced contrast
DIA
E. coli C41 (DE3)

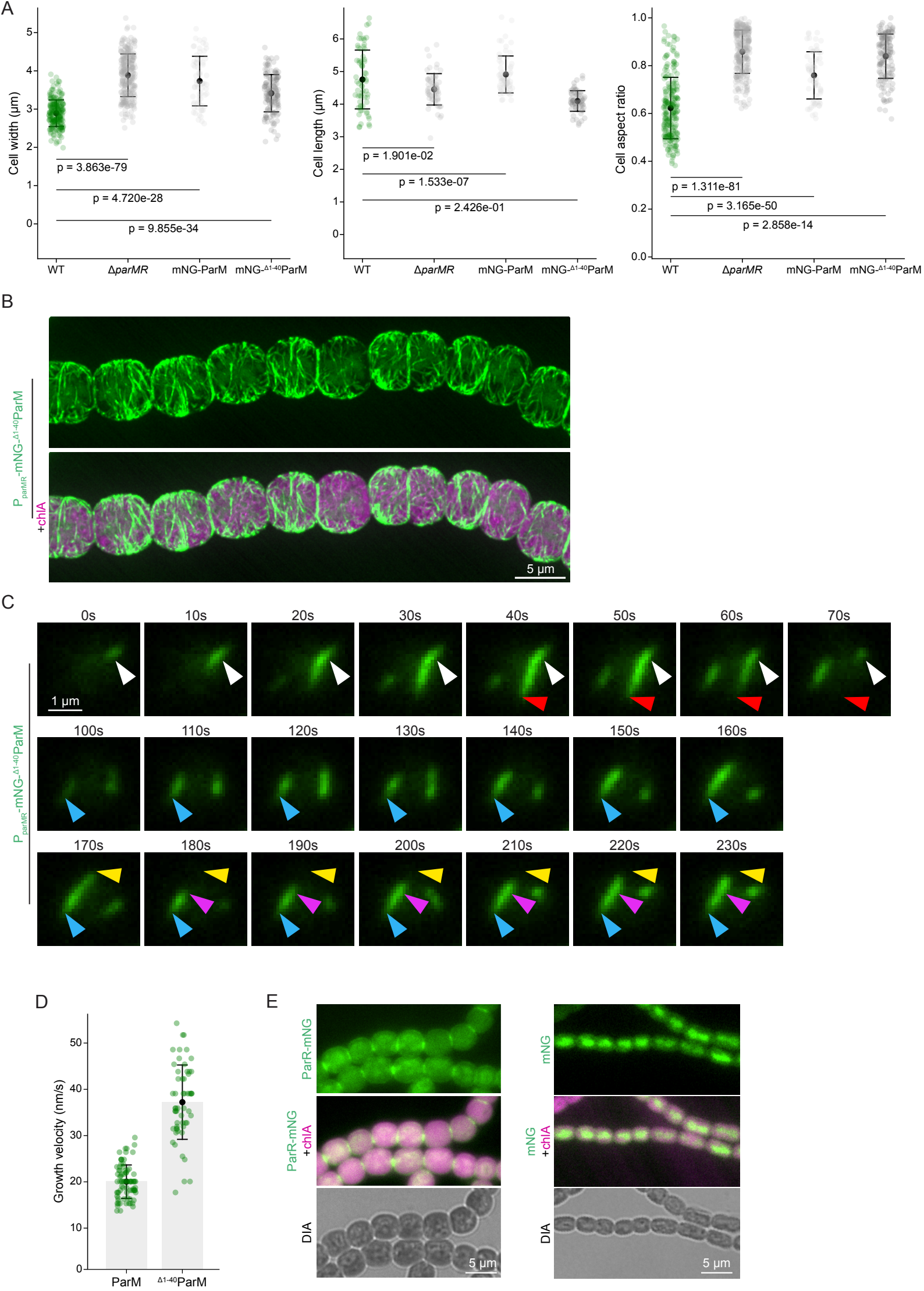
A
Cell width (µm)
p = 3.863e-79
p = 4.720e-28
p = 9.855e-34
Cell length (µm)
p = 1.901e-02
p = 1.533e-07
p = 2.426e-01
Cell aspect ratio
p = 1.311e-81
p = 3.165e-50
p = 2.858e-14
WT
ΔparMR
mNG-ParM
mNG-Δ1-40ParM
B
P parMR-mNG-Δ1-40ParM
+chlA
5 µm
C
0s
10s
20s
30s
40s
50s
60s
70s
1 µm
100s
110s
120s
130s
140s
150s
160s
170s
180s
190s
200s
210s
220s
230s
D
Growth velocity (nm/s)
ParM
Δ1-40ParM
E
ParR-mNG
ParR-mNG +chlA
DIA
5 µm
mNG
mNG +chlA
DIA
5 µm

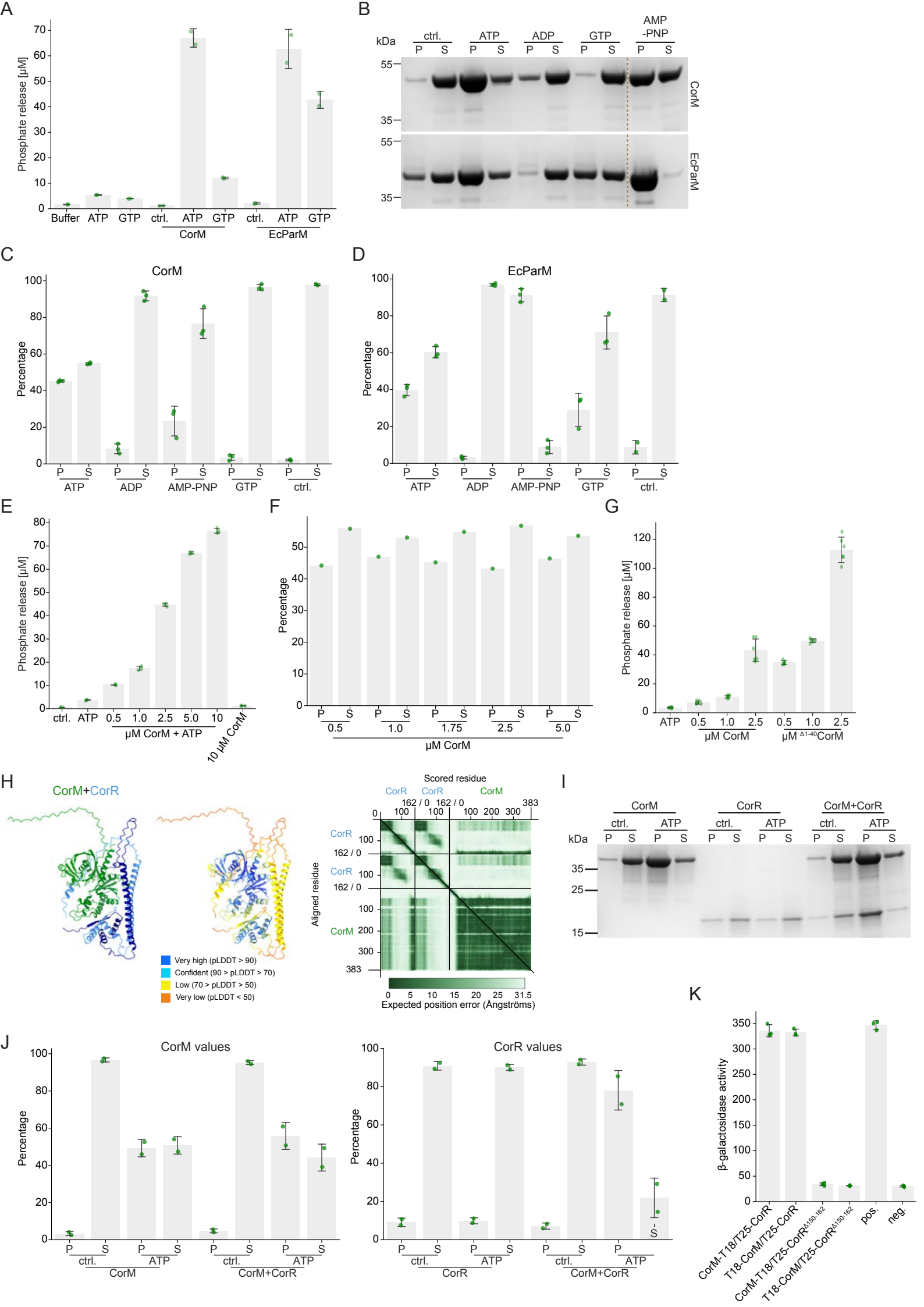
A
Phosphate release [µM]
Buffer
ATP
GTP
ctrl.
ATP
GTP
ctrl.
ATP
GTP
CorM
EcParM
B
kDa
ctrl.
ATP
ADP
GTP
AMP -PNP
P
S
55
35
CorM
EcParM
C
CorM
Percentage
ATP
ADP
AMP-PNP
GTP
ctrl.
D
EcParM
Percentage
ATP
ADP
AMP-PNP
GTP
ctrl.
E
Phosphate release [µM]
ctrl.
ATP
0.5
1.0
2.5
5.0
10
µM CorM + ATP
10 µM CorM
F
Percentage
0.5
1.0
1.75
2.5
5.0
µM CorM
G
Phosphate release [µM]
ATP
0.5
1.0
2.5
µM CorM
µM Δ1-40CorM
H
CorM+CorR
Very high (pLDDT > 90)
Confident (90 > pLDDT > 70)
Low (70 > pLDDT > 50)
Very low (pLDDT < 50)
Scored residue
CorR
CorR
CorM
162 / 0
383
Aligned residue
Expected position error (Ångströms)
I
CorM
CorR
CorM+CorR
ctrl.
ATP
kDa
35
25
15
J
CorM values
Percentage
ctrl.
ATP
CorM
CorM+CorR
CorR values
Percentage
CorR
CorM+CorR
K
β-galactosidase activity
CorM-T18/T25-CorR
T18-CorM/T25-CorR
CorM-T18/T25-CorRΔ150-162
T18-CorM/T25-CorRΔ150-162
pos.
neg.

A

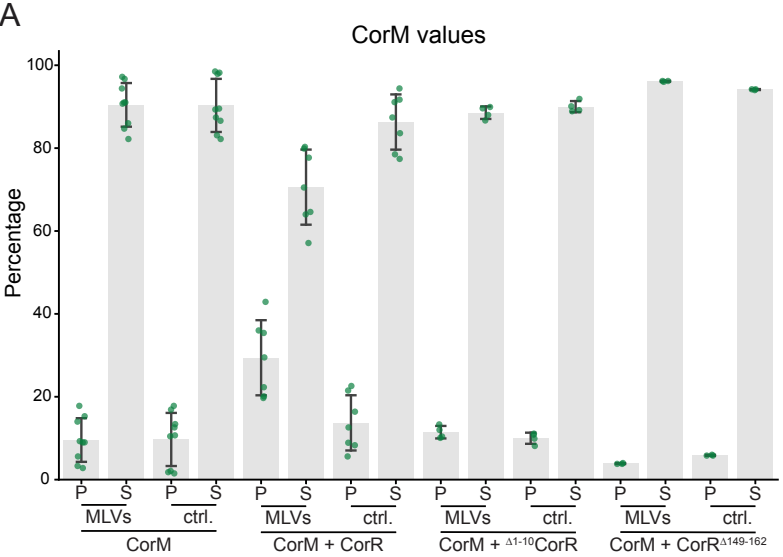
CorM values
Percentage
100
80
60
40
20
0
P S P S P S P S P S P S P S P S
MLVs ctrl. MLVs ctrl. MLVs ctrl. MLVs ctrl.
CorM
CorM + CorR
CorM + Δ1-10CorR
CorM + CorRΔ149-162

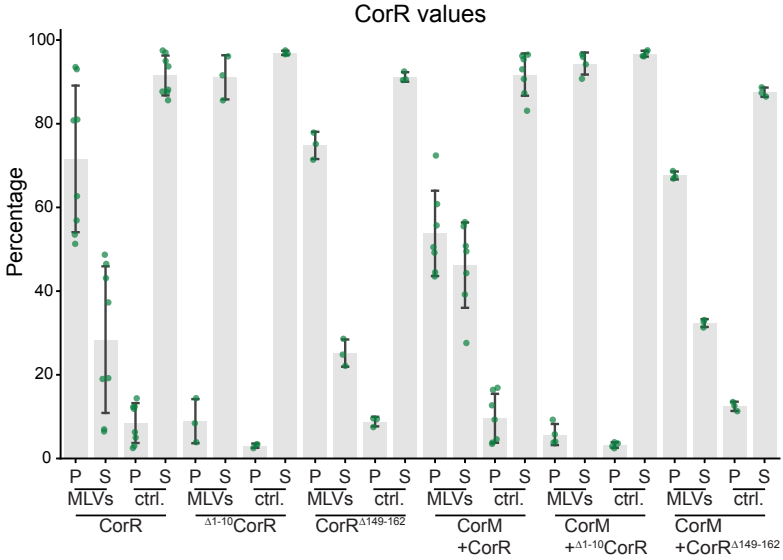
CorR values
Percentage
100
80
60
40
20
0
P S P S P S P S P S P S P S P S P S P S P S P S P S P S P S
MLVs ctrl. MLVs ctrl. MLVs ctrl. MLVs ctrl. MLVs ctrl. MLVs ctrl.
CorR
Δ1-10CorR
CorRΔ149-162
CorM +CorR
CorM +Δ1-10CorR
CorM +CorRΔ149-162

B

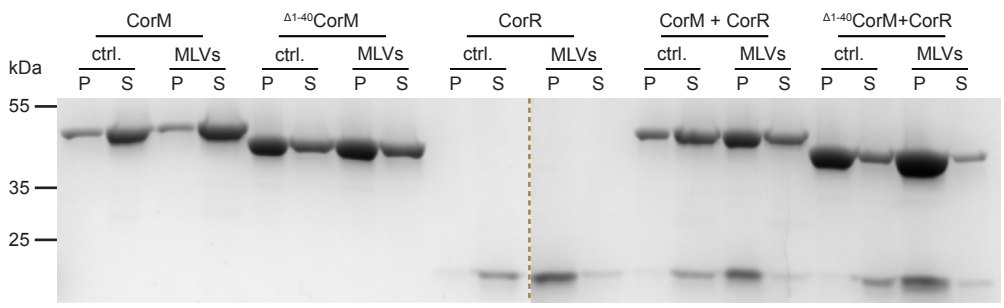
CorM
Δ1-40CorM
CorR
CorM + CorR
Δ1-40CorM+CorR
ctrl. MLVs ctrl. MLVs ctrl. MLVs ctrl. MLVs ctrl. MLVs
P S P S P S P S P S P S P S P S P S P S
kDa
55
35
25

C

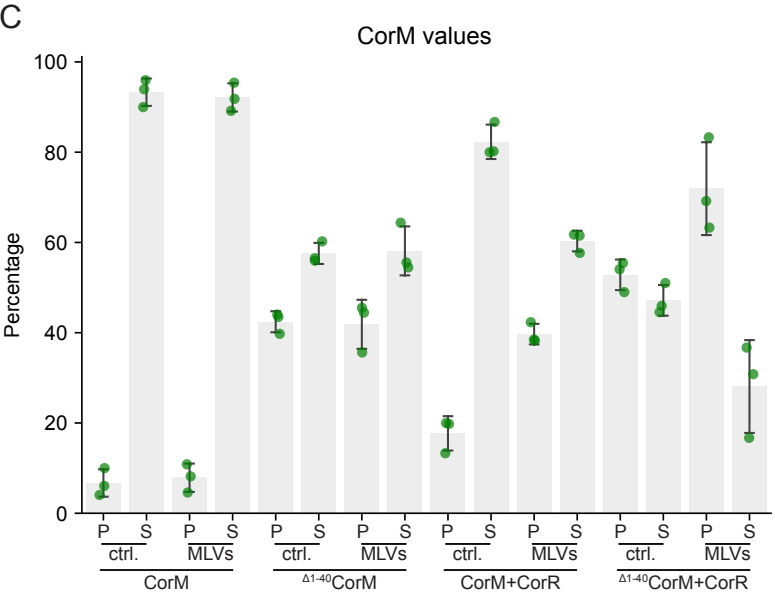
CorM values
Percentage
100
80
60
40
20
0
P S P S P S P S P S P S P S P S
ctrl. MLVs ctrl. MLVs ctrl. MLVs ctrl. MLVs
CorM
Δ1-40CorM
CorM+CorR
Δ1-40CorM+CorR

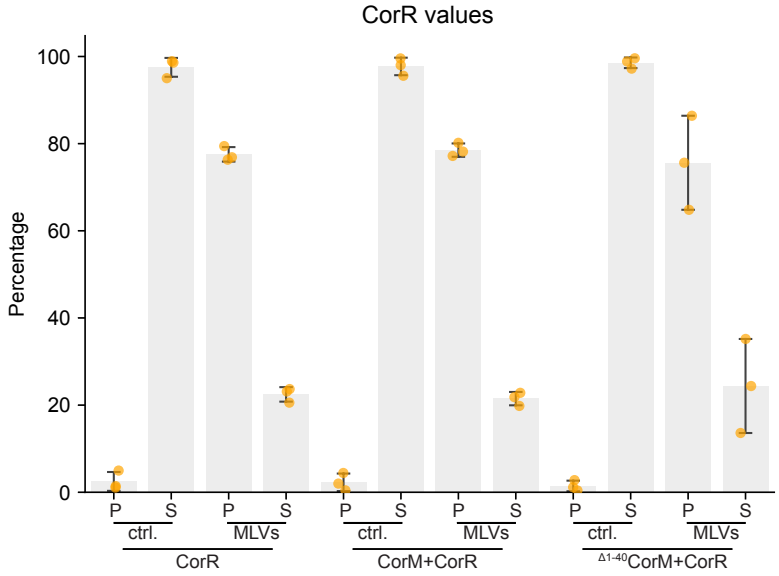
CorR values
Percentage
100
80
60
40
20
0
P S P S P S P S P S P S
ctrl. MLVs ctrl. MLVs ctrl. MLVs
CorR
CorM+CorR
Δ1-40CorM+CorR

D

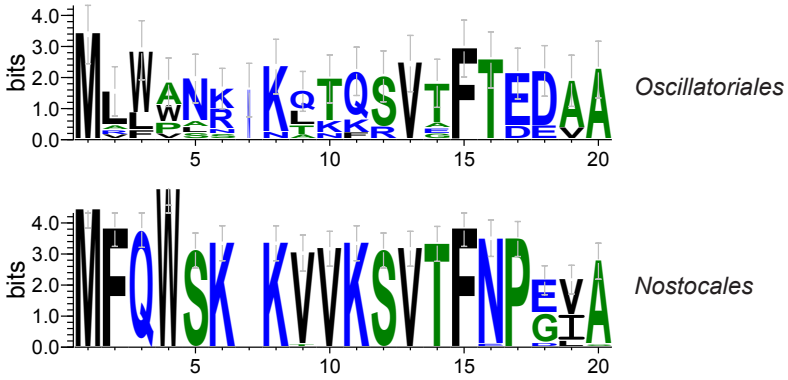
bits
4.0
3.0
2.0
1.0
0.0
5
10
15
20
Oscillatoriales
Nostocales

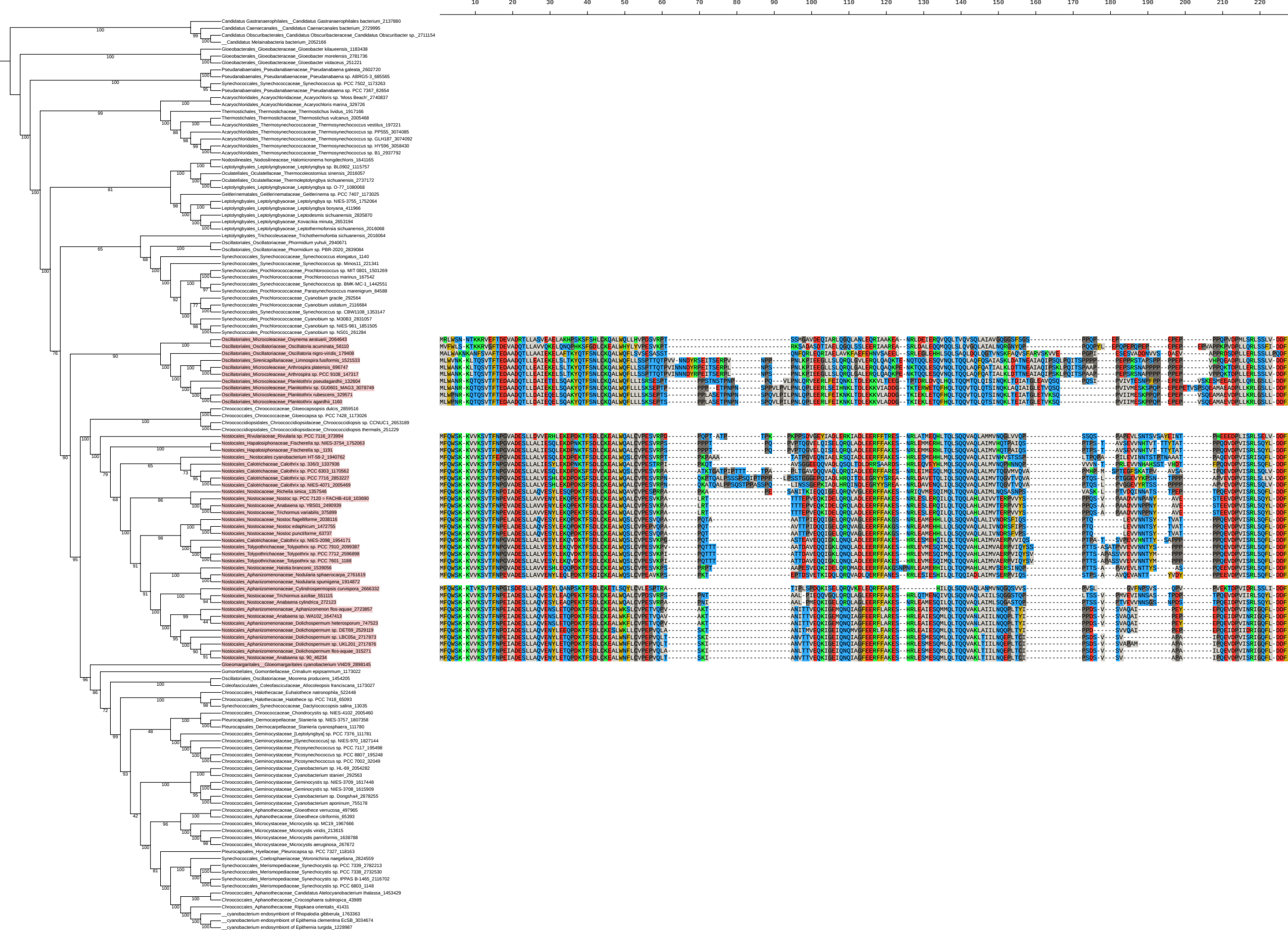
Candidatus Gastranaerophilales__Candidatus Gastranaerophilales bacterium_2137880
Candidatus Caenarcanales__Candidatus Caenarcanales bacterium_2729995
Candidatus Obscuribacterales_Candidatus Obscuribacteraceae_Candidatus Obscuribacter sp._2711154
__Candidatus Melainabacteria bacterium_2052166
Gloeobacterales_Gloeobacteraceae_Gloeobacter kilaueensis_1183438
Gloeobacterales_Gloeobacteraceae_Gloeobacter morelensis_2781736
Gloeobacterales_Gloeobacteraceae_Gloeobacter violaceus_251221
Pseudanabaenales_Pseudanabaenaceae_Pseudanabaena galeata_2602720
Pseudanabaenales_Pseudanabaenaceae_Pseudanabaena sp. ABRG5-3_685565
Synechococcales_Synechococcaceae_Synechococcus sp. PCC 7502_1173263
Pseudanabaenales_Pseudanabaenaceae_Pseudanabaena sp. PCC 7367_82654
Acaryochloridales_Acaryochloridaceae_Acaryochloris sp. 'Moss Beach'_2740837
Acaryochloridales_Acaryochloridaceae_Acaryochloris marina_329726
Thermostichales_Thermostichaceae_Thermostichus lividus_1917166
Thermostichales_Thermostichaceae_Thermostichus vulcanus_2005468
Acaryochloridales_Thermosynechococcaceae_Thermosynechococcus vestitus_197221
Acaryochloridales_Thermosynechococcaceae_Thermosynechococcus sp. PP555_3074085
Acaryochloridales_Thermosynechococcaceae_Thermosynechococcus sp. GLH187_3074092
Acaryochloridales_Thermosynechococcaceae_Thermosynechococcus sp. HY596_3058430
Acaryochloridales_Thermosynechococcaceae_Thermosynechococcus sp. B1_2937792
Nodosilineales_Nodosilineaceae_Halomicronema hongdechloris_1641165
Leptolyngbyales_Leptolyngbyaceae_Leptolyngbya sp. BL0902_1115757
Oculatellales_Oculatellaceae_Thermocoleostomius sinensis_2016057
Oculatellales_Oculatellaceae_Thermoleptolyngbya sichuanensis_2737172
Leptolyngbyales_Leptolyngbyaceae_Leptolyngbya sp. O-77_1080068
Geitlerinematales_Geitlerinemataceae_Geitlerinema sp. PCC 7407_1173025
Leptolyngbyales_Leptolyngbyaceae_Leptolyngbya sp. NIES-3755_1752064
Leptolyngbyales_Leptolyngbyaceae_Leptolyngbya boryana_411966
Leptolyngbyales_Leptolyngbyaceae_Leptodesmis sichuanensis_2835870
Leptolyngbyales_Leptolyngbyaceae_Kovacikia minuta_2653194
Leptolyngbyales_Leptolyngbyaceae_Leptothermofonsia sichuanensis_2016068
Leptolyngbyales_Trichocoleusaceae_Trichothermofontia sichuanensis_2016064
Oscillatoriales_Oscillatoriaceae_Phormidium yuhuli_2940671
Oscillatoriales_Oscillatoriaceae_Phormidium sp. PBR-2020_2839084
Synechococcales_Synechococcaceae_Synechococcus elongatus_1140
Synechococcales_Synechococcaceae_Synechococcus sp. Minos11_221341
Synechococcales_Prochlorococcaceae_Prochlorococcus sp. MIT 0801_1501269
Synechococcales_Prochlorococcaceae_Prochlorococcus marinus_167542
Synechococcales_Synechococcaceae_Synechococcus sp. BMK-MC-1_1442551
Synechococcales_Prochlorococcaceae_Parasynechococcus marenigrum_84588
Synechococcales_Prochlorococcaceae_Cyanobium gracile_292564
Synechococcales_Prochlorococcaceae_Cyanobium usitatum_2116684
Synechococcales_Synechococcaceae_Synechococcus sp. CBW1108_1353147
Synechococcales_Prochlorococcaceae_Cyanobium sp. M3083_2831057
Synechococcales_Prochlorococcaceae_Cyanobium sp. NIES-981_1851505
Synechococcales_Prochlorococcaceae_Cyanobium sp. NSC1_261284
Oscillatoriales_Microcoleaceae_Oxynema aestuarii_2064643
Oscillatoriales_Oscillatoriaceae_Oscillatoria acuminata_56110
Oscillatoriales_Oscillatoriaceae_Oscillatoria nigro-viridis_179408
Oscillatoriales_Sirenicapillariaceae_Limnospira fusiformis_1521533
Oscillatoriales_Microcoleaceae_Arthrospira platensis_696747
Oscillatoriales_Microcoleaceae_Arthrospira sp. PCC 9108_147317
Oscillatoriales_Microcoleaceae_Planktothrix pseudagardhii_132604
Oscillatoriales_Microcoleaceae_Planktothrix sp. GU0601_MAG3_3078749
Oscillatoriales_Microcoleaceae_Planktothrix rubescens_329571
Oscillatoriales_Microcoleaceae_Planktothrix agardhii_1160
Chroococcales_Chroococcaceae_Gloeocapsopsis dulcis_2859516
Chroococcales_Chroococcaceae_Gloeocapsa sp. PCC 7428_1173026
Chroococcidiopsidales_Chroococcidiopsidaceae_Chroococcidiopsis sp. CCNUC1_2653189
Chroococcidiopsidales_Chroococcidiopsidaceae_Chroococcidiopsis thermalis_251229
Nostocales_Rivulariaceae_Rivularia sp. PCC 7116_373994
Nostocales_Hapalosiphonaceae_Fischerella sp. NIES-3754_1752063
Nostocales_Hapalosiphonaceae_Fischerella sp._1191
Nostocales__Nostocales cyanobacterium HT-58-2_1940762
Nostocales_Calothrichaceae_Calothrix sp. 336/3_1337936
Nostocales_Calothrichaceae_Calothrix sp. PCC 6303_1170562
Nostocales_Calothrichaceae_Calothrix sp. PCC 7716_2853227
Nostocales_Calothrichaceae_Calothrix sp. NIES-4071_2005469
Nostocales_Nostocaceae_Richelia sinica_1357546
Nostocales_Nostocaceae_Nostoc sp. PCC 7120 = FACHB-418_103690
Nostocales_Nostocaceae_Anabaena sp. YBS01_2490939
Nostocales_Nostocaceae_Trichormus_375899
Nostocales_Nostocaceae_Nostoc flagelliformе_2038116
Nostocales_Nostocaceae_Nostoc edaphicum_1472755
Nostocales_Nostocaceae_Nostoc punctiforme_63737
Nostocales_Calothrichaceae_Calothrix sp. NIES-2098_1954171
Nostocales_Tolypothrichaceae_Tolypothrix sp. PCC 7910_2099387
Nostocales_Tolypothrichaceae_Tolypothrix sp. PCC 7712_2596898
Nostocales_Tolypothrichaceae_Tolypothrix sp. PCC 7601_1188
Nostocales_Nostocaceae_Halotia branconii_1539056
Nostocales_Aphanizomenonaceae_Nodularia sphaerocarpa_2761619
Nostocales_Aphanizomenonaceae_Nodularia spumigena_1914872
Nostocales_Aphanizomenonaceae_Cylindrospermopsis curvispora_2666332
Nostocales_Nostocaceae_Trichormus azollae_551115
Nostocales_Nostocaceae_Anabaena cylindrica_272123
Nostocales_Aphanizomenonaceae_Aphanizomenon flos-aquae_2723857
Nostocales_Nostocaceae_Anabaena sp. WA102_1647413
Nostocales_Aphanizomenonaceae_Dolichospermum heterosporum_747523
Nostocales_Aphanizomenonaceae_Dolichospermum sp. DET69_2529119
Nostocales_Aphanizomenonaceae_Dolichospermum sp. LBC05a_2717873
Nostocales_Aphanizomenonaceae_Dolichospermum sp. UKL201_2717876
Nostocales_Aphanizomenonaceae_Dolichospermum flos-aquae_315271
Nostocales_Nostocaceae_Anabaena sp. 90_46234
Gloeomargaritales__Gloeomargaritales cyanobacterium VIdD9_2898145
Gomontiellales_Gomontiellaceae_Crinalium epipsammum_1173022
Oscillatoriales_Oscillatoriaceae_Moorena producens_1454205
Coleofasciculales_Coleofasciculaceae_Allocoleopsis franciscana_1173027
Chroococcales_Halothecacae_Euhalothece natronophila_522448
Chroococcales_Halothecacae_Halothece sp. PCC 7418_65093
Synechococcales_Synechococcaceae_Dactylococcopsis salina_13035
Chroococcales_Chroococcaceae_Chondrocystis sp. NIES-4102_2005460
Pleurocapsales_Dermocarpellaceae_Stanieria sp. NIES-3757_1807358
Pleurocapsales_Dermocarpellaceae_Stanieria cyanosphaera_111780
Chroococcales_Geminocystaceae_[Leptolyngbya] sp. PCC 7376_111781
Chroococcales_Geminocystaceae_[Synechococcus] sp. NIES-970_1827144
Chroococcales_Geminocystaceae_Picosynechococcus sp. PCC 7117_195498
Chroococcales_Geminocystaceae_Picosynechococcus sp. PCC 8807_195248
Chroococcales_Geminocystaceae_Picosynechococcus sp. PCC 7002_32049
Chroococcales_Geminocystaceae_Cyanobacterium sp. HL-69_2054282
Chroococcales_Geminocystaceae_Cyanobacterium stanieri_292563
Chroococcales_Geminocystaceae_Geminocystis sp. NIES-3709_1617448
Chroococcales_Geminocystaceae_Geminocystis sp. NIES-3708_1615909
Chroococcales_Geminocystaceae_Cyanobacterium sp. Dongsha4_2878255
Chroococcales_Geminocystaceae_Cyanobacterium aponinum_755178
Chroococcales_Aphanothecaceae_Gloeothece verrucosa_497965
Chroococcales_Aphanothecaceae_Gloeothece citriformis_65393
Chroococcales_Microcystaceae_Microcystis sp. MC19_1967666
Chroococcales_Microcystaceae_Microcystis viridis_213615
Chroococcales_Microcystaceae_Microcystis panniformis_1638788
Chroococcales_Microcystaceae_Microcystis aeruginosa_267872
Pleurocapsales_Hyellaceae_Pleurocapsa sp. PCC 7327_118163
Synechococcales_Coelosphaeriaceae_Woronichinia naegeliana_2824559
Synechococcales_Merismopediaceae_Synechocystis sp. PCC 7339_2782213
Synechococcales_Merismopediaceae_Synechocystis sp. PCC 7338_2732530
Synechococcales_Merismopediaceae_Synechocystis sp. IPPAS B-1465_2116702
Synechococcales_Merismopediaceae_Synechocystis sp. PCC 6803_1148
Chroococcales_Aphanothecaceae_Candidatus Atelocyanobacterium thalassa_1453429
Chroococcales_Aphanothecaceae_Crocosphaera subtropica_43989
Chroococcales_Aphanothecaceae_Rippkaea orientalis_41431
__cyanobacterium endosymbiont of Rhopalodia gibberula_1763363
__cyanobacterium endosymbiont of Epithemia clementina EcSB_3034674
__cyanobacterium endosymbiont of Epithemia turgida_1228987

SUPPLEMENTARY 6.1

CorMR
Example micrograph

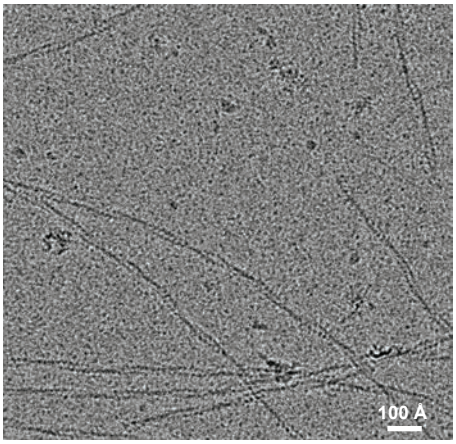

Glacios 200kV Falcon4i
(2,236 movies, 4,096x4,096 px)

cryoSPARC v4.4

Patch motion correction
Patch CTF estimation
Curate exposure

2,205 micrographs

Filament tracer
(Filament diameter 90 Å)
Particle extraction
256x256 px
(~705k particles)

2D Classification
(50 classes)
Select 2D classes
(3 classes with ~307k particles)

Filament tracer
(Filament diameter 100 Å,
25 Å separation distance)

Particle extraction
512x512 px
(~424k particles)

2D Classification
(100 classes)
Select 2D classes
(22 classes with ~311k particles)

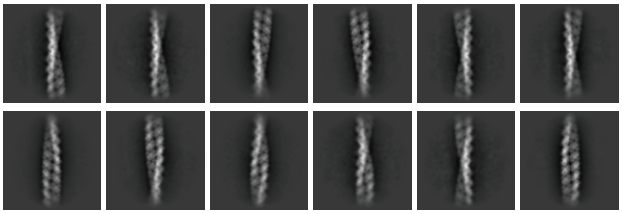

Representative 2D classes

Ab-initio reconstruction
(C1 symmetry, ~282k particles)

Homogeneous refinement
(C1 symmetry, ~282k particles)

Helical refinement
(*Helical twist -18° , rise 46.5 Å
~282k particles)

Local refinement
Local CTF refinement
Local refinement
(~282k particles)

Remove duplicate particles
(~109k particles discarded)
Homogeneous refinement
(C2 symmetry, ~173k particles)

Remove duplicate particles
(~49k particles discarded)
Homogeneous refinement
(C2 symmetry, ~124k particles)

Final map: 3.92 Å
(124,109 particles)
Helical twist: -15.75°
Helical rise: 46.427 Å
Bfactor: 111.2 Å^{-2}

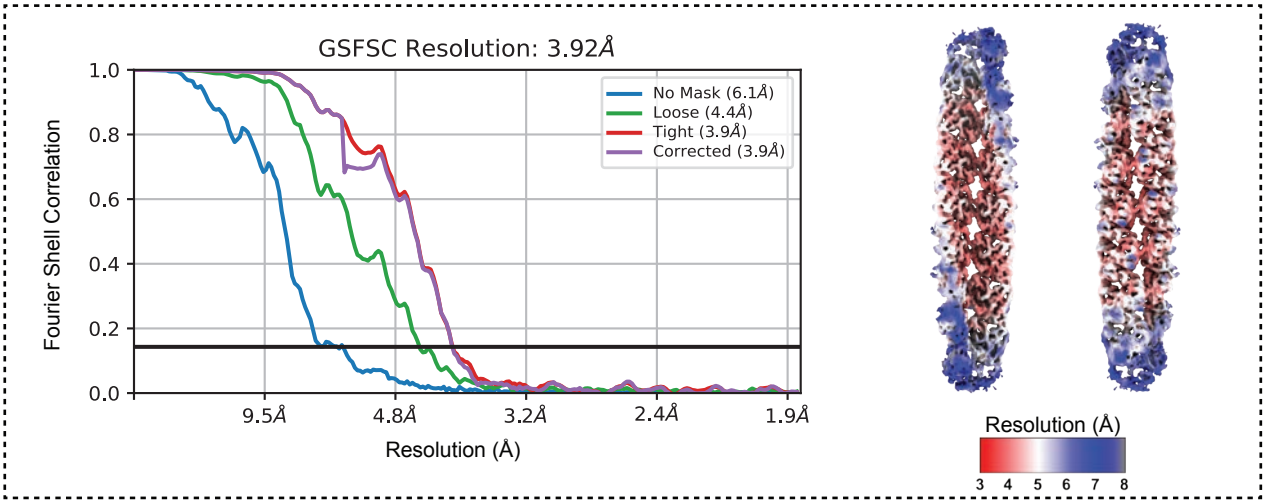

Cryo-EM image processing strategy applied to obtain CorM filament structure in the presence of CorR.

SUPPLEMENTARY 6.2

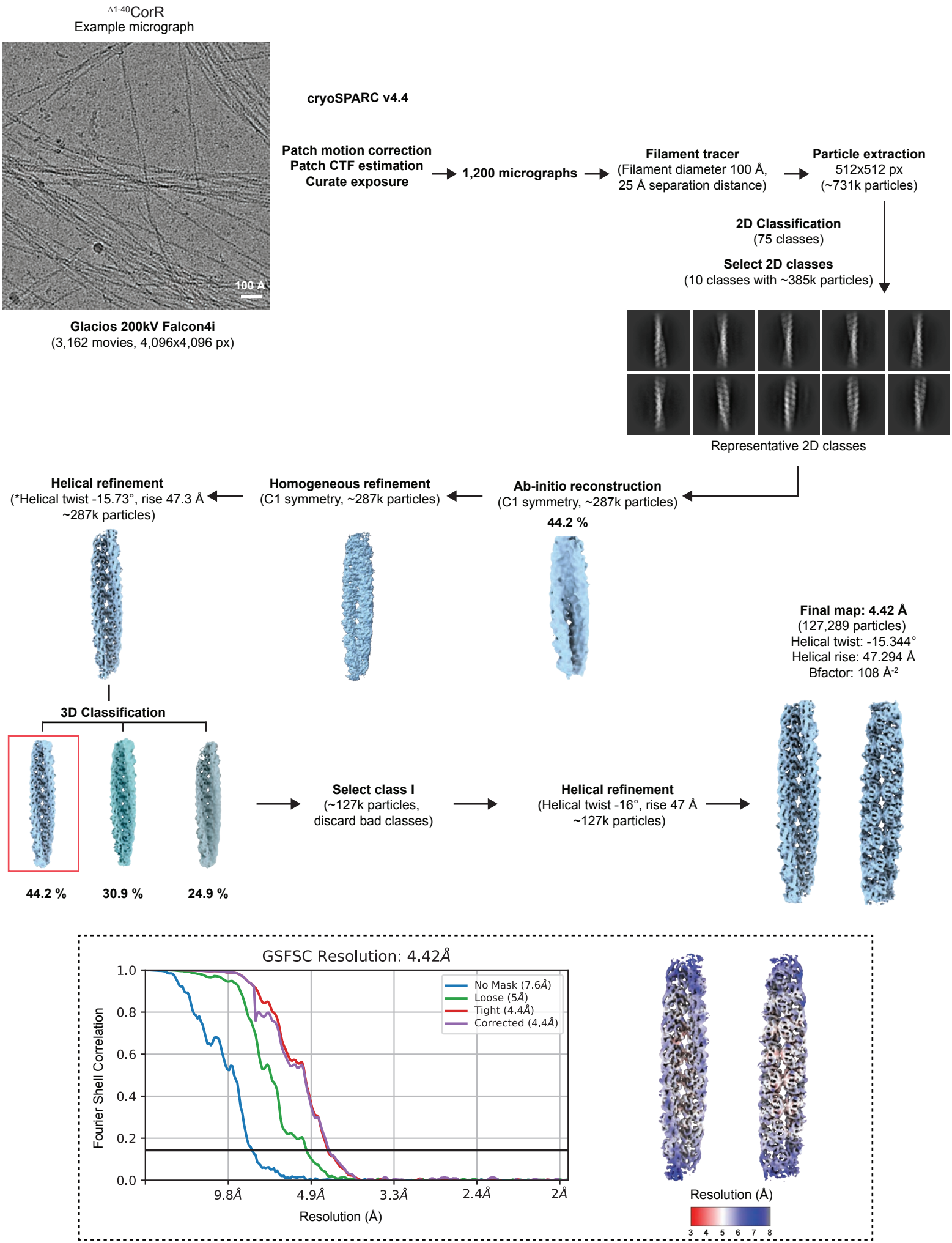

Cryo-EM image processing strategy applied to obtain N40_CorM filament structure.

SUPPLEMENTARY 6.3

CorM
Example micrograph

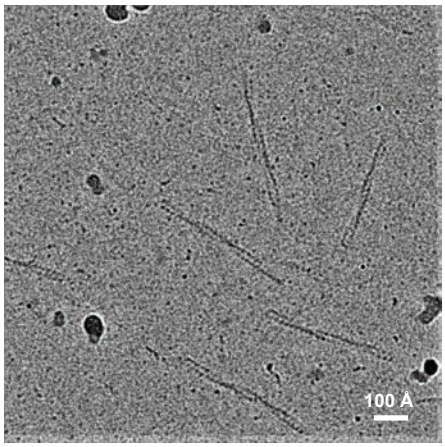

Glacios 200kV Falcon4i
(2,206 movies, 4,096x4,096 px)

cryoSPARC v4.4

Patch motion correction
Patch CTF estimation
Curate exposure

→ **2,147 micrographs**

Filament tracer
(Filament diameter 100 Å,
5 Å separation distance)
Particle extraction
512x512 px
(~2M particles)

→ **2D Classification**
(100 classes)
Select 2D classes
(22 classes with ~333k particles)

↓

Filament tracer
(Filament diameter 100 Å,
1 Å separation distance)

→ **Particle extraction**
360x360 px
(~6M particles)

↓

2D Classification (4X)

↓

Ab-initio reconstruction
Homogeneous refinement
(C1 symmetry, ~227k particles)

↓

Re-extract particles
512x512 px
(~211k particles)

↓

2D Classification
Select 2D classes
(7 classes with ~197k particles)

← **Ab-initio reconstruction**
(C1 symmetry, ~197k particles)

← **Homogeneous refinement**
(C1 symmetry, ~197k particles)

← **Helical refinement**
(*Helical twist -18.5°, rise 46.5 Å
~197k particles)

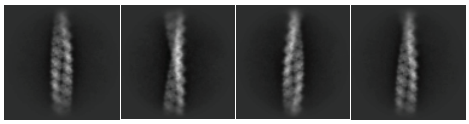

Representative 2D classes

3D Classification

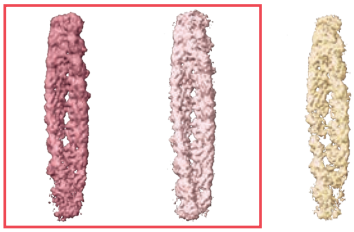

41.6 % **36.7 %** **21.7 %**

→ **Select class I & II**
(~154k particles,
discard bad class)

→ **Helical refinement**
(Helical twist -18.5°, rise 46.5 Å
~154k particles)

→ **Final map: 7.14 Å**
(154,726 particles)
Helical twist: -18.5°
Helical rise: 46.5 Å
Bfactor: 420.3 Å^{-2}

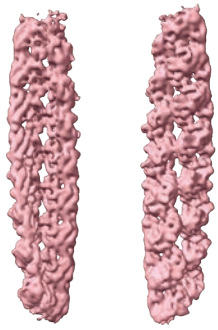

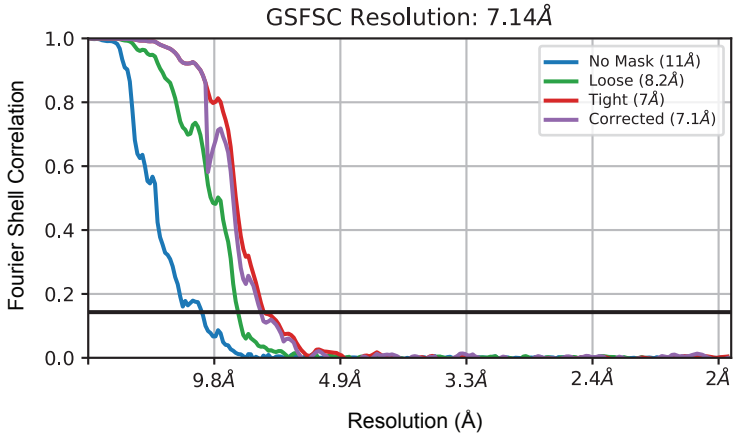

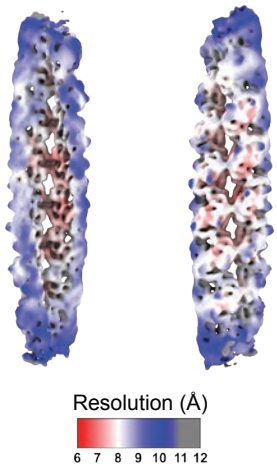

Cryo-EM image processing strategy applied to obtain CorM filament structure.

SUPPLEMENTARY 6.4

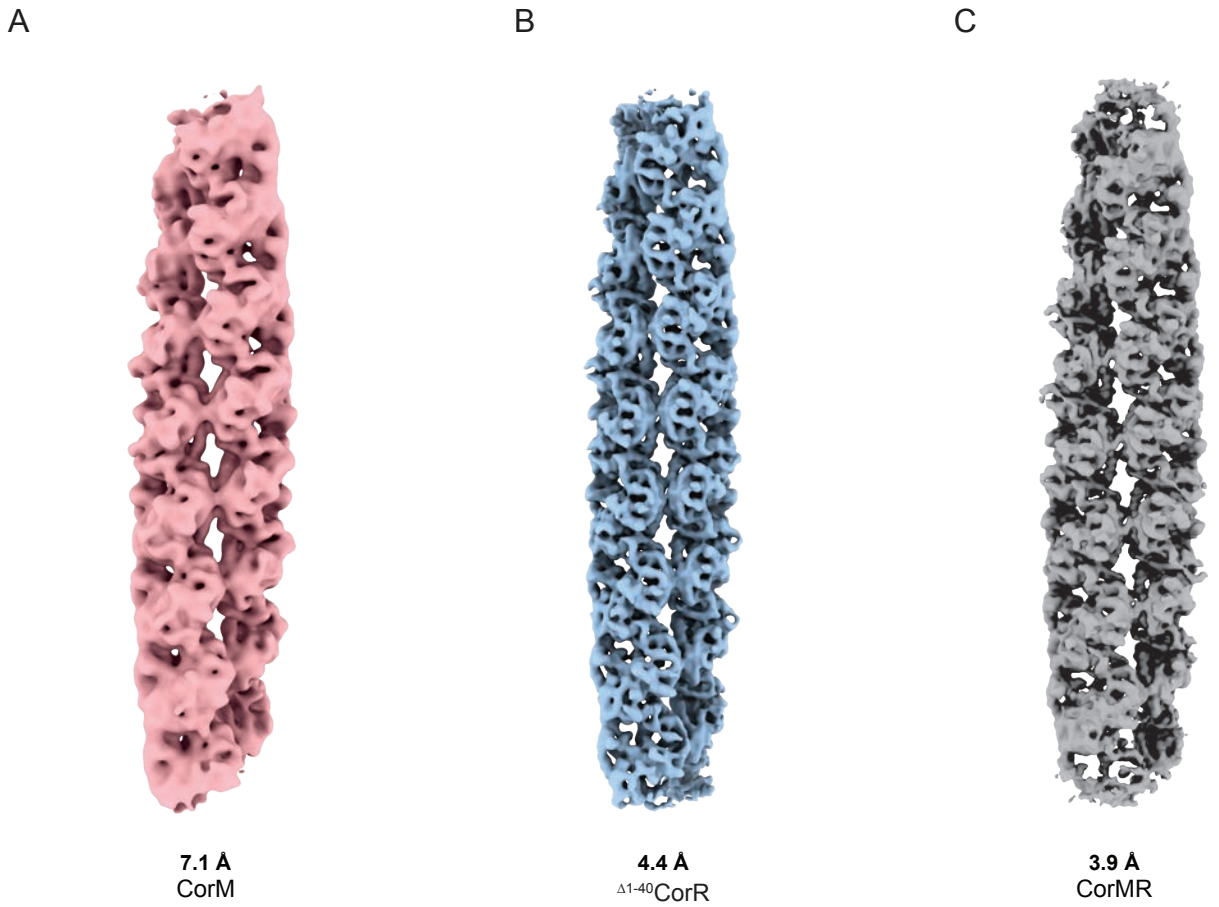

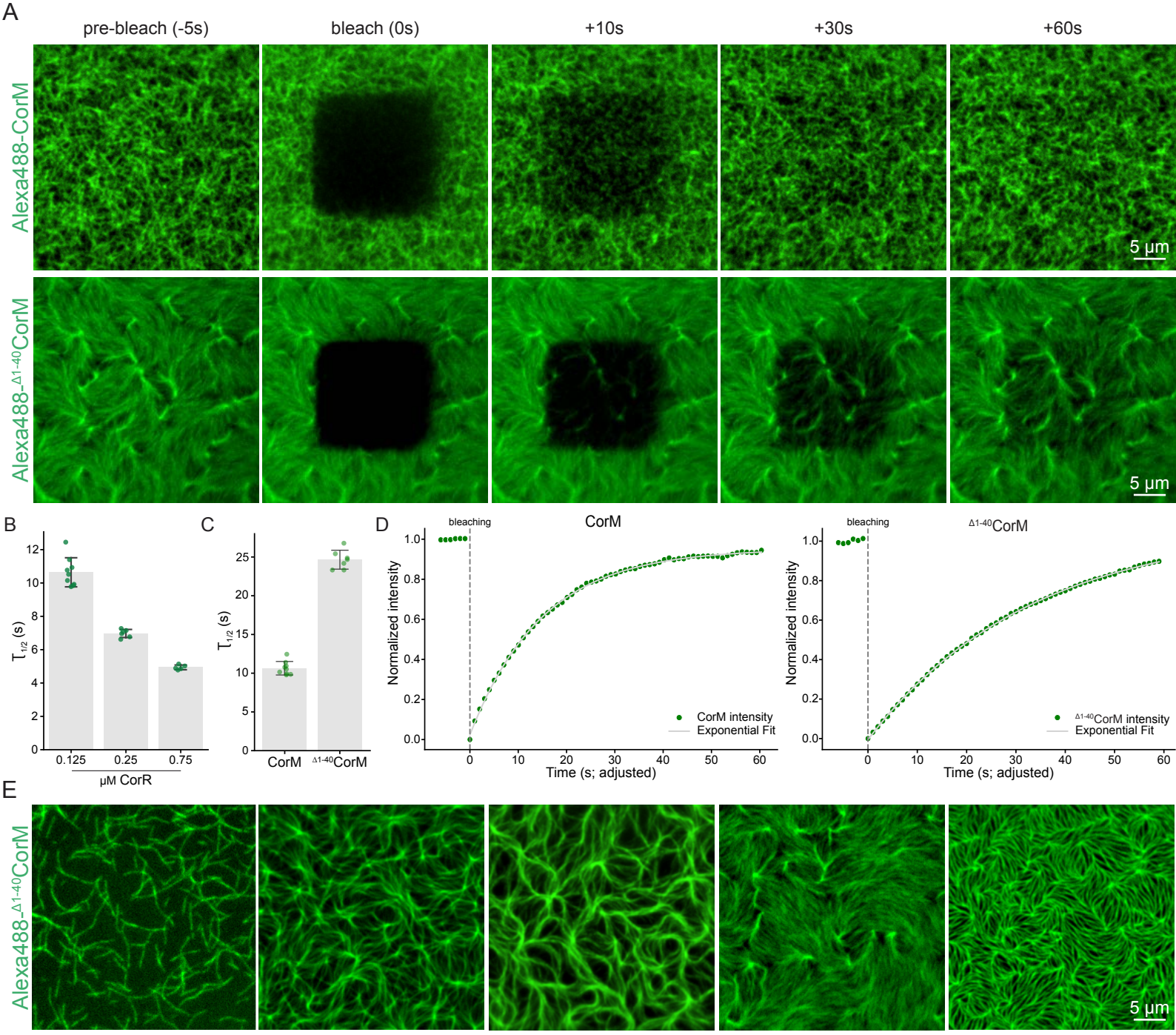
A
pre-bleach (-5s)
bleach (0s)
+10s
+30s
+60s
Alexa488-CorM
Alexa488-Δ1-40CorM
5 µm
B
$T_{1/2}$ (s)
0.125
0.25
0.75
µM CorR
C
CorM
Δ1-40CorM
D
bleaching
CorM
Normalized intensity
Time (s; adjusted)
CorM intensity
Exponential Fit
Δ1-40CorM intensity
E

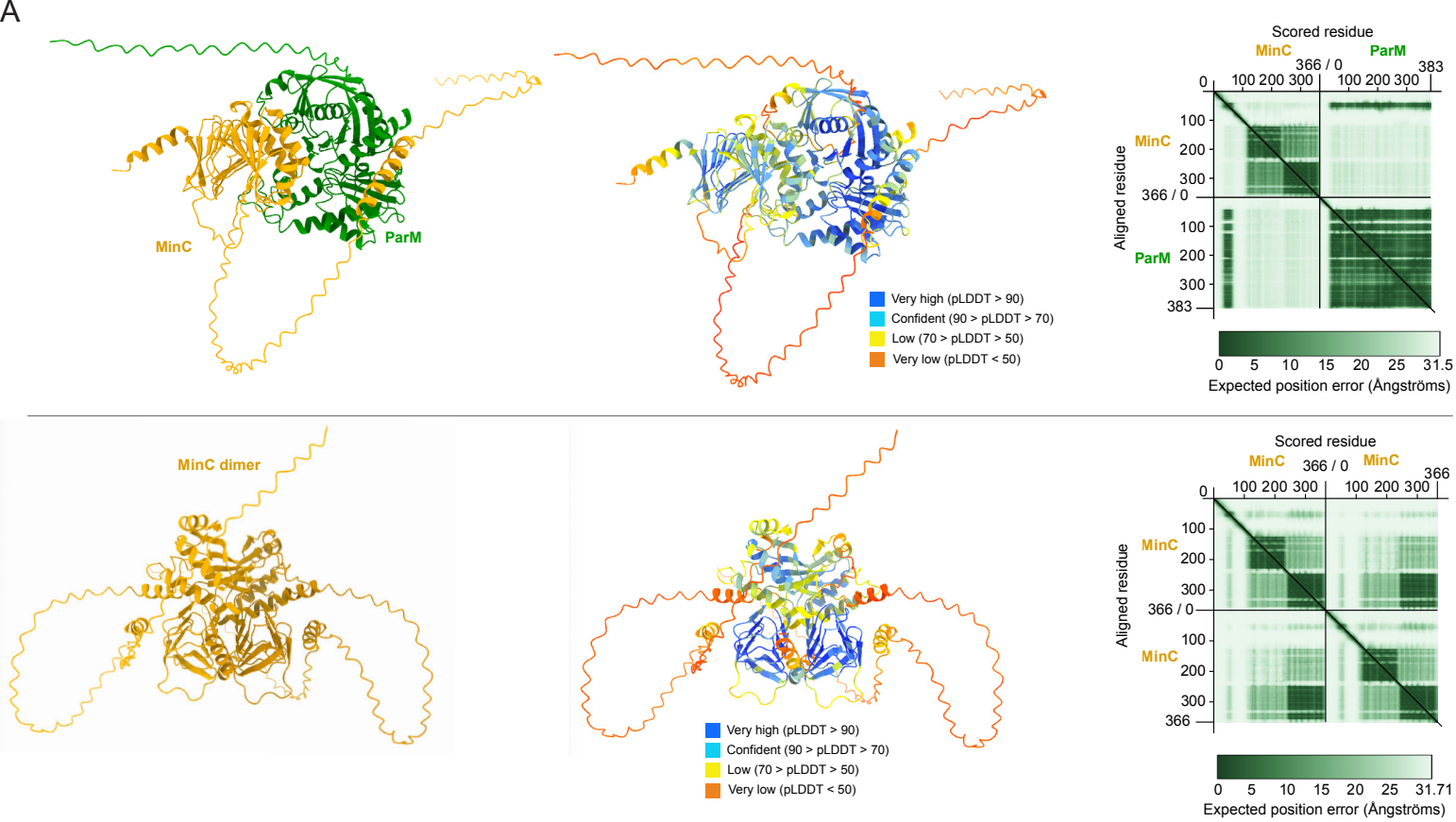
A
MinC
ParM
Very high (pLDDT > 90)
Confident (90 > pLDDT > 70)
Low (70 > pLDDT > 50)
Very low (pLDDT < 50)
Scored residue
Aligned residue
366 / 0
383
Expected position error (Ångströms)
MinC dimer
366

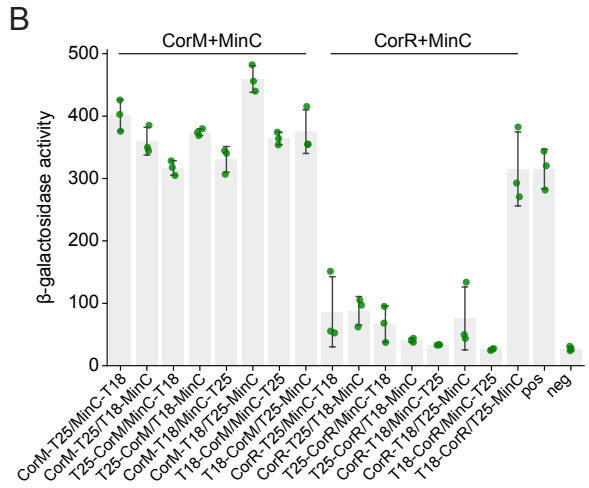
B
CorM+MinC
CorR+MinC
β-galactosidase activity
CorM-T25/MinC-T18
CorM-T25/T18-MinC
T25-CorM/MinC-T18
T25-CorM/T18-MinC
CorM-T18/MinC-T25
T18-CorM/T25-MinC
CorR-T25/MinC-T18
CorR-T25/T18-MinC
T25-CorR/MinC-T18
T25-CorR/T18-MinC
CorR-T18/MinC-T25
T18-CorR/T25-MinC
pos
neg

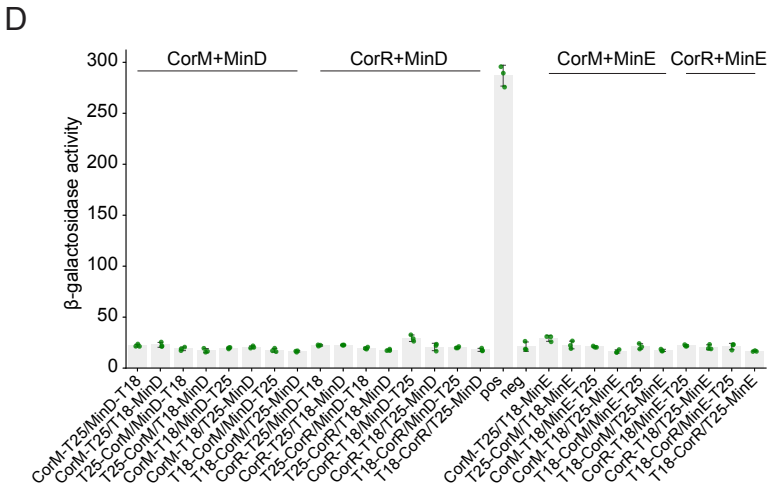
D
CorM+MinD
CorR+MinD
CorM+MinE
CorR+MinE
β-galactosidase activity
CorM-T25/MinD-T18
CorM-T25/T18-MinD
T25-CorM/MinD-T18
T25-CorM/T18-MinD
CorM-T18/MinD-T25
T18-CorM/T25-MinD
CorR-T25/MinD-T18
CorR-T25/T18-MinD
T25-CorR/MinD-T18
T25-CorR/T18-MinD
CorR-T18/MinD-T25
T18-CorR/T25-MinD
pos
neg
CorM-T25/T18-MinE
T25-CorM/T18-MinE
CorM-T18/MinE-T25
T18-CorM/T25-MinE
CorR-T25/T18-MinE
T25-CorR/T18-MinE
CorR-T18/T25-MinE
T18-CorR/T25-MinE

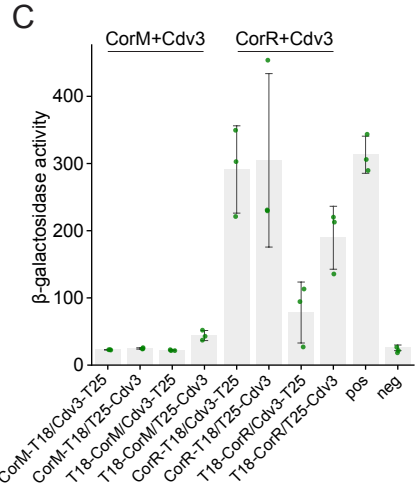
C
CorM+Cdv3
CorR+Cdv3
β-galactosidase activity
CorM-T18/Cdv3-T25
CorM-T18/T25-Cdv3
T18-CorM/Cdv3-T25
T18-CorM/T25-Cdv3
CorR-T18/Cdv3-T25
CorR-T18/T25-Cdv3
T18-CorR/Cdv3-T25
T18-CorR/T25-Cdv3
pos
neg

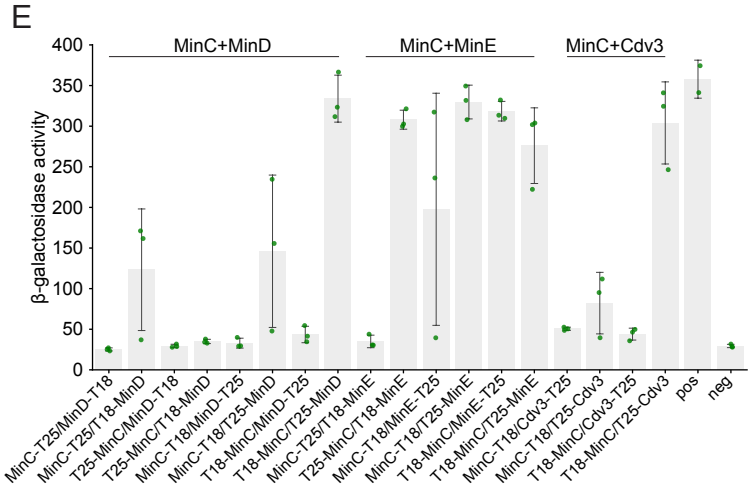
E
MinC+MinD
MinC+MinE
MinC+Cdv3
β-galactosidase activity
MinC-T25/MinD-T18
MinC-T25/T18-MinD
T25-MinC/MinD-T18
T25-MinC/T18-MinD
MinC-T18/MinD-T25
MinC-T18/T25-MinD
T18-MinC/MinD-T25
T18-MinC/T25-MinD
MinC-T25/T18-MinE
T25-MinC/T18-MinE
MinC-T18/MinE-T25
MinC-T18/T25-MinE
T18-MinC/MinE-T25
T18-MinC/T25-MinE
MinC-T18/Cdv3-T25
MinC-T18/T25-Cdv3
T18-MinC/Cdv3-T25
T18-MinC/T25-Cdv3
pos
neg

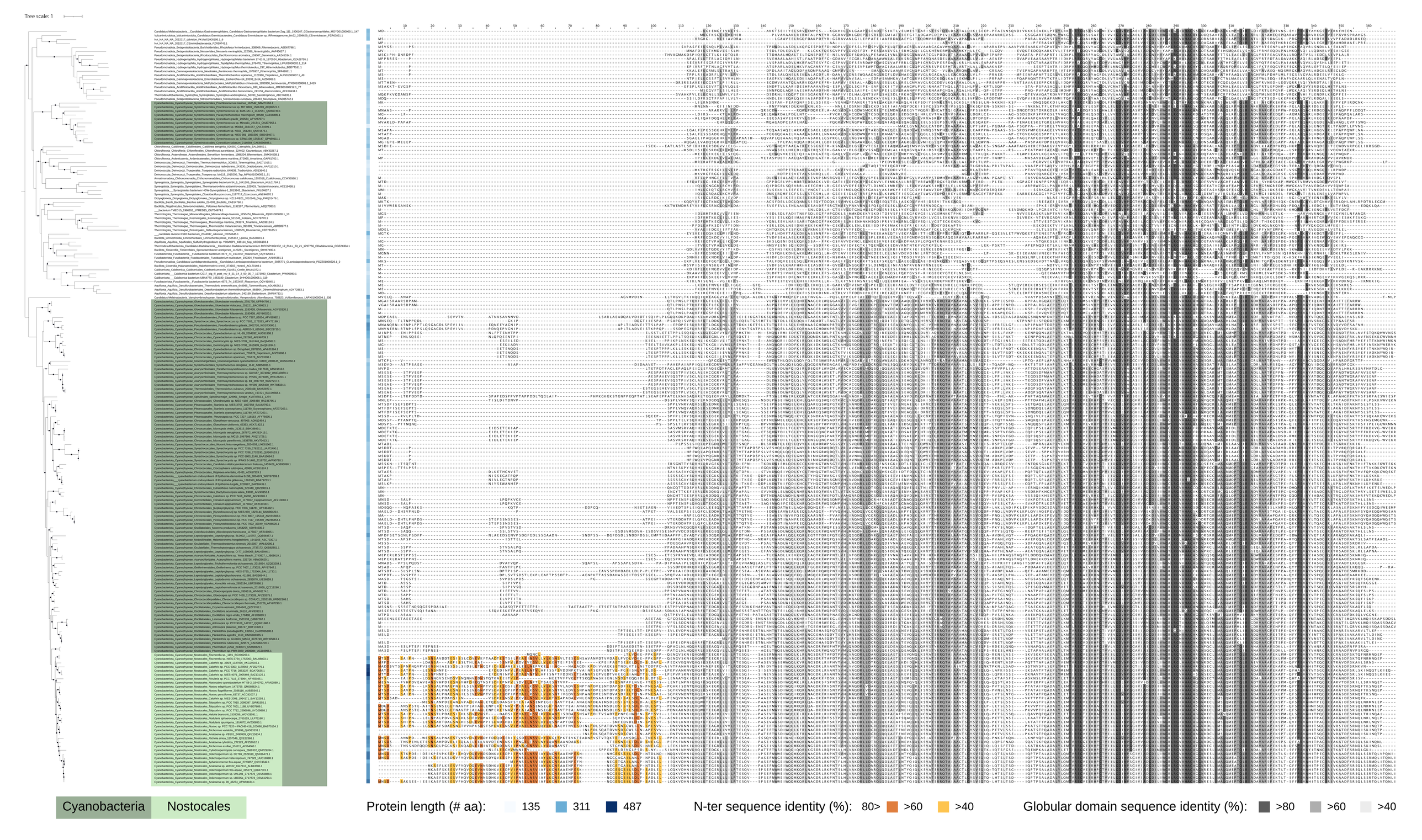
Tree scale: 1
Cyanobacteria
Nostocales
Protein length (# aa):
135
311
487
N-ter sequence identity (%):
80>
>60
>40
Globular domain sequence identity (%):
>80
>60
>40

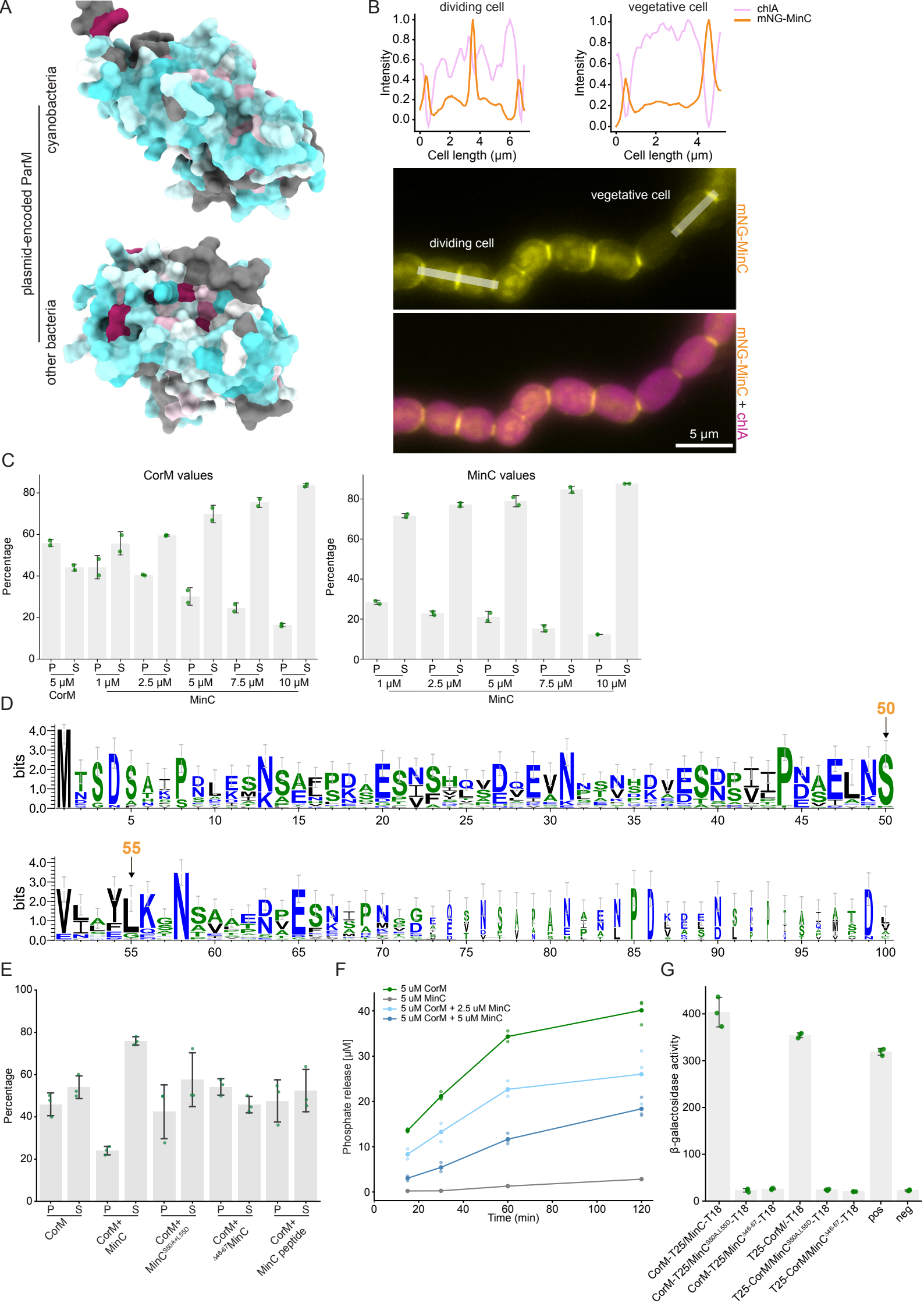
A
plasmid-encoded ParM
cyanobacteria
other bacteria
B
dividing cell
vegetative cell
chlA
mNG-MinC
Intensity
Cell length (μm)
mNG-MinC
mNG-MinC + chlA
5 μm
C
CorM values
MinC values
Percentage
5 μM CorM
1 μM
2.5 μM
5 μM
7.5 μM
10 μM
MinC
D
bits
50
55
E
Percentage
CorM
CorM+ MinC
CorM+ MinC^S50A,L55D
CorM+ Δ46-67MinC
CorM+ MinC peptide
F
5 uM CorM
5 uM MinC
5 uM CorM + 2.5 uM MinC
5 uM CorM + 5 uM MinC
Phosphate release [μM]
Time (min)
G
β-galactosidase activity
CorM-T25/MinC-T18
CorM-T25/MinC^S50A,L55D-T18
CorM-T25/MinC^Δ46-67-T18
T25-CorM/-T18
T25-CorM/MinC^S50A,L55D-T18
T25-CorM/MinC^Δ46-67-T18
pos
neg